Ph.D. Dissertation

Ka-band Tunable Metamaterial Absorber with a Stress-induced MEMS Cantilever Using Oxygen Plasma Ashing

산소 플라즈마 애싱 공정을 이용한 응력 구배 MEMS 외팔보가 있는 Ka밴드 대역 가변형 메타물질 흡수체

August 2022

Seoul National University

Department of Electrical and Computer Engineering

Myungjin Chung

Ka-band Tunable Metamaterial Absorber with a Stress-induced MEMS Cantilever Using Oxygen Plasma Ashing

지도 교수 김 용 권

이 논문을 공학박사 학위논문으로 제출함
2022 년 8 월

서울대학교 대학원
전기·정보공학부
정 명 진

정명진의 공학박사 학위논문을 인준함
2022 년 8 월

위 원 장 <u>　　　남 상 욱　　</u> (인)

부위원장 <u>　　　김 용 권　　</u> (인)

위　　원 <u>　　　백 창 욱　　</u> (인)

위　　원 <u>　　　김 정 무　　</u> (인)

위　　원 <u>　　　오 정 석　　</u> (인)

Abstract

This dissertation proposes and realizes the first Ka-band frequency tunable metamaterial absorber with stress-induced MEMS cantilever with oxygen plasma ashing process. To employ a MEMS-driven actuator for LC resonance frequency tuning method in the GHz regime, the split-ring resonator (SRR) structure of the metamaterial unit cell is designed to have a sub-mm scale cantilever as a capacitor element of the unit cell. To enlarge capacitance change, the MEMS cantilever is released with a large out-of-plane deflection by the plasma ashing process. This MEMS cantilever with stress gradient is arranged at four parts of a symmetrical SRR unit cell, and the two cells compose the absorber sample as an array structure. The overall cantilevers of the absorber actuate from the initial bent upward state to pulled down state when the electrostatic voltage is applied. The decrease of deflection reduces the gap between cantilevers and bottom electrodes to increase capacitance for frequency tuning to lower frequency.

To verify and improve the uniformity of the mechanical behavior of the absorber, this research proposes and demonstrates 3 different design types of releasing on stress-induced cantilevers. First, the array design of 12 cantilevers with 400 µm in length and 50 µm widths is modified from a cantilever with 400 µm in length and 800 µm widths. To overcome the limitation on the mechanical behavior of cantilever arrays due to their nonuniformity, further modification on

etching hole rearrangement is reflected in the 2nd type of rectangular cantilever. The space length of etch hole varies depending on the position from the open end of cantilevers. This incremental space length between 8 μm etch holes from the open end enables sequential releasing of cantilevers during photoresist oxygen plasma ashing. The cyclic process was performed in the ashing process to lower the distribution of fabrication results. Finally, the last design to have a semicircle shape with incremental space length between etching holes to improve the uniformity of the cantilever to prevent such drawbacks of a wrinkled profile which the previous design shows. Also, our last design is driven by a digital drive creating 5 different reconfiguration states.

With full-wave simulations, the performance of the proposed absorber demonstrates experimentally in each of 5 different reconfiguration states. The initially measured deflection of the cantilever beam is 51.8 μm on average. At the initial state, the resonant frequency and the absorptivity are 32.95 GHz and 80.95%. When all the cantilevers are pulled down, the frequency shifts a total of 4.08 GHz from the initial state showing a tuning ratio of 12.29 %. The error between the measured value and the simulation value came within 0.39 GHz in all five states. This dissertation demonstrated the potential of MEMS as a tuning method for Ka-band absorbers.

Keyword : Ka-band, Metamaterial absorber, Frequency tunable, MEMS, Stress-induced cantilever, oxygen plasma ashing

Student Number : 2017-32662

List of contents

List of tables

List of figures

CHAPTER 1. Introduction

1.1 Background

1.1.1 Advent of metamaterial

A metamaterial is an artificially tailored composite of periodic or non-periodic structure as a creation for engineering purposes, whose function shows a peculiar and exotic electromagnetic behavior unlike materials found in nature [1, 2]. This metamaterial function is due to both the chemical composition and the cellular architecture structuralized on a size scale smaller than the wavelength of external stimuli. Figure 1.1 is a brief view archetypal of the periodic structure of metamaterials studied recently [3-9].
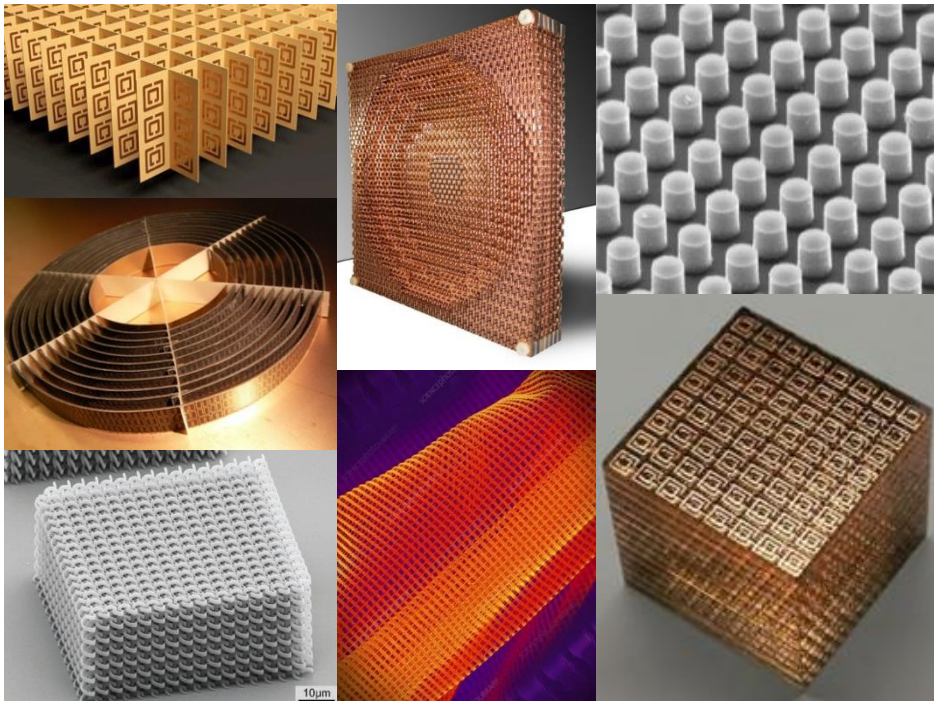
Figure 1.1. The periodic structure of metamaterials [3-9]

Currently, metamaterials are called by various names, such as frequency selective surface (FSS), high-impedance surface (HIS), left-handed material (LHM), negative index material, and meta-device, depending on the scope and the conceptual ambiguity of the research object or the continuous development of research in each field. Notably, before the nomenclature of metamaterial was suggested by Roger M. Walser in 1999, the metamaterial was first called the left-handed material in 1968, the time when Vaselago proposed its concept. Indeed, one of the early discoveries of the theoretical phenomena of negative refraction and backward-wave propagation dates back to 1944, the year when the research by L.I. Mandelshtam is published [1]. Afterward, the advent of negative index materials spawned extensive research into metamaterials.

1.1.2 Application of metamaterial

The vast amount of studies related to compelling phenomena on metamaterials such as metalens [10-13], slow light [14-17], device with chirality [18-22], negative refractive index[23, 24], ultrafast device [25, 26], antenna elements[27, 28], perfect absorption [29, 30], etc. have being vigorously announced. Metamaterials are attractive not only for their exotic electromagnetic properties but also for their promise for applications. Figure 1.2 shows a glance at the application of the metamaterial phenomena.

N. I. Landy *et al.*, 2008 [29] N. Wiu *et al.*, 2010 [30] W. Panpradit *et al.*, 2012 [21] B. Wang *et al.*, 2009 [22]

<Perfect absorption> <Chiral device>

X. Chen *et al.*, 2012 [13] K. Chen *et al.*, 2017 [12] M. Choi *et al.*, 2011 [14] S.-Y. Chiam *et al.*, 2009 [16]

<Metalens> <Slow light>

M. Ren *et al.*, 2011 [25] K. M. Dani *et al.*, 2009 [26]

<Ultrafast device>

D. R. Smith *et al.*, 2000 [23] S. Xiao *et al.*, 2010 [24]

<Negative refractive index>

S. Zhu *et al.*, 2013 [27] N. Vasilantonakis *et al.*, 2015 [28]

<Antenna/waveguide>
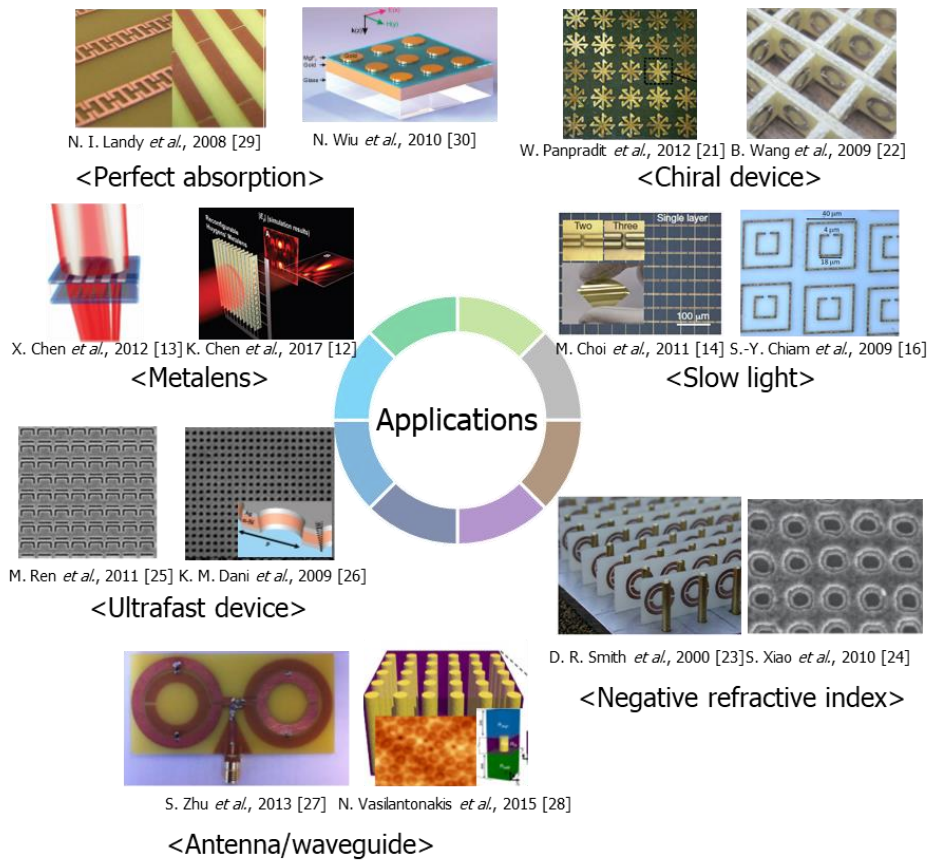
Figure 1.2. Metamaterial and its application

1.1.3   Physics of metamaterial

▪ Electromagnetic behavior of metamaterial

Previously mentioned outcomes are based on the fact that the electromagnetic properties of the material are mostly defined by a function of its permittivity (ε) and permeability (μ).

As a matter of fact, the permittivity and the permeability of almost all isotropic materials found in nature such as dielectrics have a positive value. That is,

3

these natural materials are usually called double-positive (DPS) materials or right-handed medium (RHM) since the wave vector $\vec{K}$ forms a right-handed system with the electric and magnetic field $\vec{E}$ and $\vec{H}$. Additionally, there are some materials with negative permittivity and positive permeability values typically such as noble metals. The dielectric constant of such metals has frequency dependency in the Drude-Lorentz model, and the permittivity is negative below the plasma frequency. This region is to be denoted as an epsilon negative (ENG) material or electric plasma in an evanescent wave-propagation perspective. Moreover, certain materials such as gyrotropic magnetic materials show the permittivity of positive values and the permeability of negative values. Such a realm is called mu-negative (MNG) or magnetic plasma in an evanescent wave-propagation perspective. However, there is no such thing found in nature with both negative values of permittivity and permeability. The only way to achieve the corresponding specifications is to artificially design composite structures. These synthetically fabricated materials are labeled as double-negative (DNG) materials or left-handed medium due to the left-handed form relations of the wave vector and the electric/magnetic fields. Figure 1.3 represents the first to the fourth quadrant of the $\varepsilon - \mu$ domain.
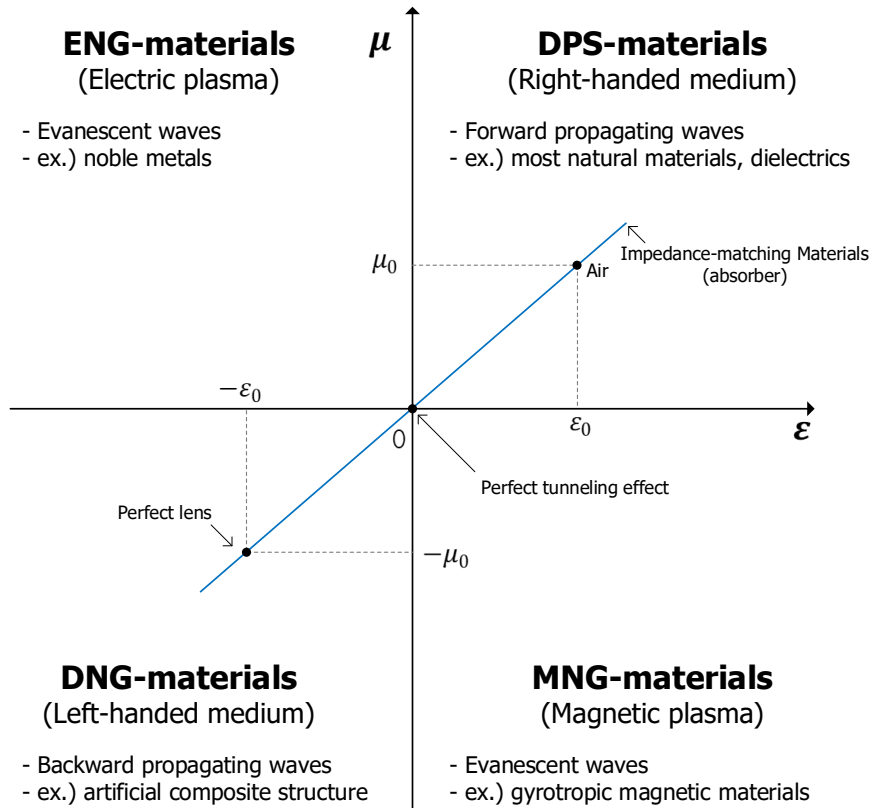
Figure 1.3. The quadrant of the material classification according to wave propagation characteristics

Materials can be categorized in a quadrant. In $\varepsilon - \mu$ domain, a point $(0,0)$ denotes the perfect tunneling effect and the point (ε_0, μ_0) indicates the air. Furthermore, the point $(-\varepsilon_0, -\mu_0)$ is where the perfect lens is applied and the linear graph crossing the air elucidates the materials with impedance matching or somehow called absorber. The wave vector and the pointing vector are in the same direction on DPS media. However, the pointing vector of the light in DNG media has a reverse direction from the wave vector. Figures 1.4 (a) and (b) explain the comparison of the incident wave path between the DPS-DPS boundary and the DPS
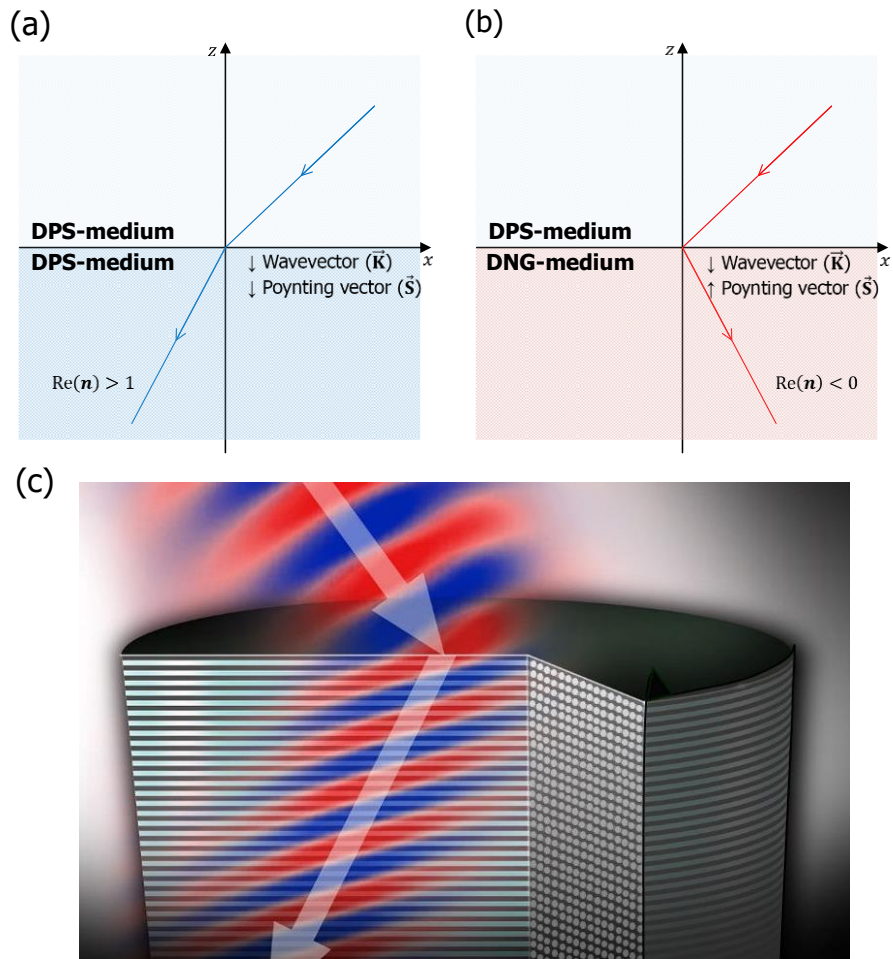
Figure 1.4. (a) The wave path between DPS-DPS boundary (b) The wave path with negative refractive index (c) The schematic of the wave path in metamaterial

▪ Mathematical compendium on the foundation of metamaterial physics

The previous explanation of categorizing material properties by the sign of permittivity and permeability is based on the following foundation of physics. Below glance at the explanation of material nature is a microscopic view. That is, a simple approximation or maybe the most favorable approximation on motion of the bounded electron in a dielectric atom can be modelized by the second harmonic Lorentz oscillation. Therefore, the complex permittivity with the single resonance could be expressed as

$$\widetilde{\varepsilon_r}(\omega) = 1 + \frac{\omega_{pe}^2}{\omega_{0_e}^2 - \omega^2 - j\omega\Gamma_e} \qquad \text{Eqn. 1.1}$$

where ω_{0_e} is the electric resonance frequency, Γ_e is electric damping coefficient and ω_{pe} is electric plasma frequency [31]. In here,

$$\omega_{pe} \overset{\text{def}}{=} \sqrt{\frac{N_e q_e^2}{m_e \varepsilon_0}} \qquad \text{Eqn. 1.2}$$

N_e is the number density of electrons, q_e is an electron charge, and m_e is an effective mass of electrons. Also, due to the duality of electromagnetics, the complex permeability of the Lorentz model on dielectric materials having the magnetic dipole of electron spinning nucleus can be expressed as the following equation.

$$\widetilde{\mu_r}(\omega) = 1 + \frac{\omega_{pm}^2}{\omega_{0_m}^2 - \omega^2 - j\omega\Gamma_m} \qquad \text{Eqn. 1.3}$$

ω_{0_m} is the magnetic resonance frequency, Γ_m is the magnetic damping coefficient and ω_{pm} is a magnetic plasma frequency. The magnetic plasma

frequency is

$$\omega_{pm} \stackrel{\text{def}}{=} \sqrt{\frac{N_m q_e^2}{m_e \varepsilon_0}} \qquad \text{Eqn. 1.4}$$

N_m is the number density of magnetic charges, q_m is a magnetic charge, and m_e is an effective magnetic mass.

If it is certain that the complex permittivity and the complex permeability are known, the macroscopic views on the physics of wave propagation are achieved by some of the well-defined parameters. First of all, the complex refractive index is in the following relationship.

$$\tilde{n} = \sqrt{\widetilde{\mu_r}\widetilde{\varepsilon_r}} \qquad \text{Eqn. 1.5}$$

In the other hand, in the frequency domain, the complex refractive index $\tilde{n}$ has the real part (n) for wave propagation and the imaginary part (κ) called attenuation coefficient for wave decay. This refractive index is also related to the propagation constant (γ).

$$\tilde{\gamma} = \gamma_0 \tilde{n} = \gamma_0 \sqrt{\widetilde{\mu_r}\widetilde{\varepsilon_r}} \qquad \text{Eqn. 1.6}$$

The $\gamma_0 = \frac{2\pi}{\lambda_0}$ is the propagation constant for free space, and the λ_0 is the free-space wavelength. Also, the impedance of a certain medium could be calculated by the following terms.

$$\tilde{\eta} = \frac{|\vec{E}|}{|\vec{H}|} \qquad \text{Eqn. 1.7}$$

The complex impedance $\tilde{\eta}$ has the real part η' which has the amplitude relations and the imaginary part η'' that is related to phase. Also, the complex impedance can be rewritten relative to the free space impedance.

$$\tilde{\eta} = \eta_0 \sqrt{\frac{\widetilde{\mu_r}}{\widetilde{\varepsilon_r}}} = \sqrt{\frac{\mu_0 \widetilde{\mu_r}}{\varepsilon_0 \widetilde{\varepsilon_r}}} \qquad \text{Eqn. 1.8}$$

Thus, the key approach for designing a metamaterial absorber is acquired by impedance matching with the air impedance $\eta_0 = 376.730\ \Omega$. With the above parameters, the reflection coefficient ($\Gamma(\omega)$), the transmission coefficient ($T(\omega)$) of the air-medium with a thickness (d), and the absorptivity ($A(\omega)$) have the following relations [60].

$$\Gamma(\omega) = \frac{\eta_0 - \tilde{\eta}}{\eta_0 + \tilde{\eta}} \qquad \text{Eqn. 1.9}$$

$$T(\omega) = e^{-\gamma d} \qquad \text{Eqn. 1.10}$$

$$A(\omega) = 1 - \Gamma(\omega) - T(\omega) \qquad \text{Eqn. 1.11}$$

Therefore, the complex permittivity and the complex permeability can be rewritten with the propagation coefficient and the reflection coefficient.

$$\widetilde{\varepsilon_r} = \frac{\tilde{\gamma}}{\gamma_0} \left(\frac{1 - \Gamma}{1 + \Gamma} \right) \qquad \text{Eqn. 1.12}$$

$$\widetilde{\mu_r} = \frac{\tilde{\gamma}}{\gamma_0} \left(\frac{1 + \Gamma}{1 - \Gamma} \right) \qquad \text{Eqn. 1.13}$$

That is, the design parameters of the target metamaterial define the complex permittivity and the complex permeability which determines S-parameters. Ironically, the experimental measurement of return loss (S_{11}) and the insertion loss (S_{21}) infer the graphical plot on the permittivity and the permeability, and ascertain the metamaterial characteristic.

The absorptivity (A) has the following relation with the reflection coefficient (Γ), the transmission coefficient (T).

$$A = 1 - |\Gamma|^2 - |T|^2 \qquad\qquad \text{Eqn. 1.14}$$

Moreover, the S-parameters are related to the reflection coefficient Γ and the transmission coefficient T.

$$S_{11} \, [\text{dB}] = 20 \log(|\Gamma|) \qquad\qquad \text{Eqn. 1.15}$$

$$S_{21} \, [\text{dB}] = 20 \log(|T|) \qquad\qquad \text{Eqn. 1.16}$$

Strictly speaking, the reflection coefficient is a voltage ratio, and its dB conversion value is S_{11}, but S_{11} is regarded as the reflection coefficient in many literatures and references. In this thesis, the title of the graph y-axis of simulation and measurement of S_{11} value will be unified as "Reflection coefficient (dB)".

To conclude, the absorptivity can be written with the S-parameters in following equation.

$$A = \left(1 - 10^{\frac{S_{11}}{10}} - 10^{\frac{S_{21}}{10}}\right) \times 100 \, [\%] \qquad\qquad \text{Eqn. 1.17}$$

1.1.4   Meta-atom

Decisively, the quintessence of this research on artificial engineering to yield desired electromagnetic response is achieved by controlling the permittivity and permeability by specially designing the geometry of the unit cell, in charge of the subwavelength resonant structure of the metamaterial, called a meta-atom. The coupling construction is accomplished by manifold structures such as mushroom-type artificial magnetic conductor (AMC) shape [32], interconnected grid structure

[33], colloidal nanoparticle [34], optimized binary FSS patterns [35], triple wires[36], spiral resonators [37], Swiss rolls [38], meta-solenoids [39], S-shaped structures [40], chiral structures [41], and etc. Figure 1.5 expresses diverse shapes of metamaterial unit cells.

Mushroom-type AMC shape [32]	Grid structure [33]
Colloidal nanoparticle [34]	Binary FSS pattern [35]
Triple wire structure [36]	Spiral resonator shape [37]
Swiss roll shape [38]	Meta-solenoid structure [39]
S-shape [40]	Chiral structure [41]

Figure 1.5. Several types of meta-atoms in the metamaterial

▪ Split-ring resonator unit cell

Despite the multifarious shapes on the resonant structure having been demonstrated by countless papers, the split-ring resonator (hereinafter referred as SRR) is the most common and straightforward method to design subwavelength resonant structure. Metamaterial researches based on the SRR shape have been most widely and intensely reported and became mainstream [6, 42, 43].

SRR is the structure with an enclosed loop with splits at opposite ends. Most the metamaterial are a combination of the dielectric substrate and the metal SRR pattern above them. These artificial media create a strong electromagnetic coupling.

By Faraday's law, an electromagnetic field is induced when a time-varying magnetic field is applied in a split ring and again occurs a rotating current. So much that, the induced currents generate the split ring's own secondary magnetic field enhancing or diminishing the incident fields. That is, these semi-enclosed loop patterns of metal act as an equivalent LC circuit. Specifically, the capacitor stores the energy in terms of an electric field, and in fact this possesses a dielectric response showing Lorentz like behavior.

Additionally, researches on the derivative form of SRR such as the complementary split-ring resonator (CSRR) [3, 24, 44], the micro-split split-ring resonator (MSSRR) [45-47], the electric LC resonator (ELC) [30, 48, 49], Omega(Ω)-shaped structures [50-52] and etc. are also actively progressing. Figure 1.6 is the example list of the scientific works on SRR.

D. Schurig *et al.*, 2006 [6]	C. Sabah *et al.*, 2012 [42]	W. Zhang *et al.*, 2012 [43]

Split-ring resonator

R. A. Shelby *et al.*, 2000 [3]	D. R. Smith *et al.*, 2018 [24]	S. K. Patel *et al.*, 2016 [44]

Complementary split-ring resonator

E. Ekmekci *et al.*, 2009 [45]	A. X. Lalas *et al.*, 2017 [46]	X. He *et al.*, 2011 [47]

Micro-split split-ring resonator

N.-I. Landy *et al.*, 2008 [30]	Y.-S. Lin *et al.*, 2013 [48]	J. Naqui *et al.*, 2014 [49]

Electric LC resonator

R. Basiry *et al.*, 2011 [50]	F. Zhang *et al.*, 2008 [51]	F. Dincer *et al.*, 2013 [52]

Omega-shape resonator

Figure 1.6. Metamaterial unit cell based on SRR and SRR derivatives

13

1.1.5   Electromagnetic absorber to metamaterial absorber

        This thesis will focus on the metamaterial absorber among metamaterial fields. It is considerably worthy to engineer such a substance that can manipulate the electromagnetic (EM) wave. The EM absorber is central to manufacture those EM controlling products. As previously mentioned, the perfect EM absorption could be achieved by matching of free space impedance and the metamaterial impedance. This is called the impedance matching theory.

        Explaining in deductive form, the EM absorber can be generally categorized into resonant EM absorbers and broadband EM absorbers. The trace of EM absorber dates back to the early 20century. Perhaps the first absorber-related outcome is thought to be an absorber research by Naamlooze Vennootschap Machineriee in 1938 [53].

        The major type of the early stage was the form of Salisbury screen which is the stereotype of resonant EM absorber devised by W. W. Salisbury [53]. Also, similar absorbers of Salisbury such as the Jaumann absorber devised by J. Jaunann and circuit analogy absorbers were independently published [54]. Other EM absorber types are Dällenbach layer, crossed grating absorber, Geometric transition absorber (foam absorber), and etc.

        Even though the above absorbers show excellency on performance in the aspect of the absorptivity, the mandatory design constraint on the form factor of EM absorber is that the absorber device should have at least a quarter operation wavelength ($\frac{\lambda}{4}$) dimension in the direction of the traveling wave.

        By way of contrast, unlike the conventional EM absorbers mentioned above,

EM absorbers based on metamaterial structure comprise numberless engineering merits in the respect of absorptivity performance to volume ratio. Moreover, this EM absorber designing with metamaterial leads to provide a manufacturing or fabrication process advantage in terms of the level of difficulty and economic benefits. Thus, in 2006, the first type of the metamaterial-based absorber was theoretically scrutinized [55]. Unlike the other conventional EM absorbers having $\frac{\lambda}{4}$ requirement, studies on metamaterial absorbers showed from $\frac{\lambda}{35}$ to even $\frac{\lambda}{75}$ [30, 56-58].

Figure 1.7 assists on understanding the fundamental differences between the typical types of absorbers mentioned above and absorbers based on metamaterial.

Due to the advantage on volume to performance ratio and design flexibility, metamaterial absorbers, regardless of its targeting frequency from GHz even up to THz, having been widely applied to sundry fields such as detection and sensing. One of the major applications of metamaterial absorber is thermal emitters [59, 60]. Moreover, applications on microbolometers using metamaterial absorber have been reported [61, 62]. Practical application such as automotive radar, imaging, wireless network, and etc. has vigorously developing [63].
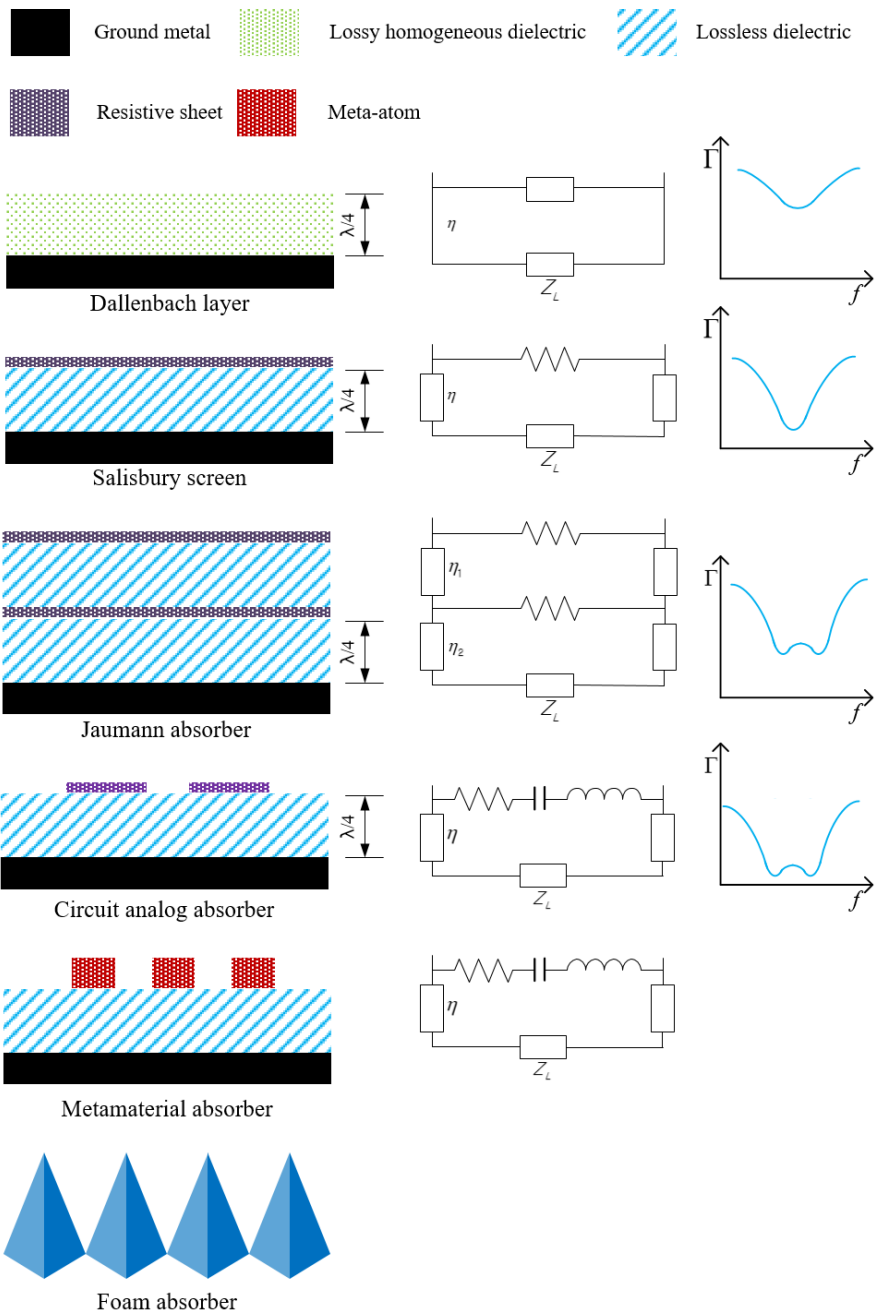
Figure 1.7. The comparison of EM absorbers types

1.1.6 Reconfigurable metamaterial

Even if the metamaterial-based device for electromagnetic wave reflection and transmission has higher degree of freedom in terms of meta-atom design flexibility and better volume-to-performance ratio, metamaterial absorbers have limitations and tolerance problems on losses and operational bandwidth resulting narrow absorption. That is, a single narrow absorption could limit the sensitivity of such sensor application device based on the metamaterial absorber.

One of the straightforward approaches to solve these drawbacks of metamaterial is to change reflectance of meta-atom in any way. As a result of this, many studies have been attempted to apply the tuning mechanism to metamaterials recently.

In modern engineering society, the active control of metamaterial has been reached by brilliant strategies. Macroscopically, frequency tuning methods of metamaterial are categorized in three typical ways. One is using a special material tuning characteristic itself, another is using electrical tuning components in metamaterial, and the other is mechanical tuning.

Such intrinsic material tuning are shown below : liquid crystal [64-66], graphene & carbon nanotube [67-69], ferroelectric/ferromagnetic material [70, 71], optically pumped photo-conductive material [72-74], phase change material [75, 76], thermally controlled materials [77-80]. In here, like the inherent ambiguity of taxonomy, the classification of phase change material and thermally controlled material would cause unsureness as the phase change material are mostly activated

by thermally controlled mechanism. However, distinguishing phase change material and thermally controlled material, in the sense of all-encompassing a wide range of ways to trigger phase change transitions in addition to thermally controlled mechanism, can help, at least, to fathom the concept of the tunable metamaterial.

Another tuning category is electrical tuning mechanism : PIN diode [81-83], varactor [84-86], non-Foster material [87, 88], semiconductors [89-93], superconductors [94-96]. As well as a particular material mentioned above, it has been proven that tuning of metamaterial be originated from materials integrated with unique geometrical shape such as nanorods [97, 98], and Origami [99, 100].

However, the most straight forward of tuning metamaterials is to modify displacement of meta-atom by mechanically tuning method [101-103].

Figure 1.8 shows the glimpse of the diversification of tuning mechanism in metamaterial research.

1. Mechanical tuning
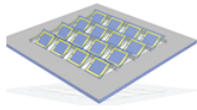
H. Tao *et al* (2009) [122]
**Displacement shift/
deformation**
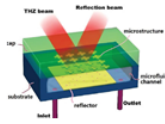
X. Hu *et al* (2016)
Microfluidic

2. Electrical tuning
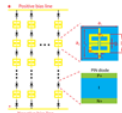
W. Xu *et al* (2013) [81]
PIN diode
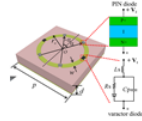
T. Wu *et al* (2021) [84]
Varactor
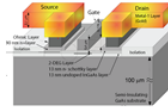
D. Shrekenhamer *et al* (2011) [89]
Semiconductor
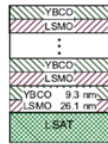
A. Pimenov *et al* (2005) [94]
Superconductor

3. Material based tuning
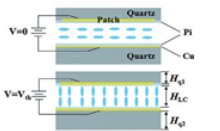
Z. Yin *et al* [64]
Liquid crystal
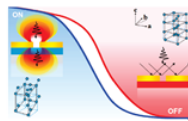
M. Seo *et al* (2010) [75]
Phase change material
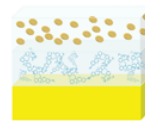
M. K. Hedayati *et al* (2014) [72]
**Optically pumped
material**

H. Yan *et al* [67]
Graphene/CNT
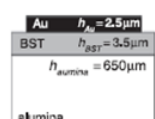
M. Gil *et al* (2009) [70]
Ferroelectric/magnetic

Figure 1.8. Tuning mechanism of metamaterials

On the subject of this tuning mechanism of metamaterial, the forte and the counter demerits of each tuning methods are briefly summarized in the below Table 1.1.

Table 1.1. Merits and demerits of the tuning mechanism

Tuning mechanism		Strength	Issues
Mechanical tuning	Microfluidic	- Drastic change - Resistant to contamination - Elimination of bias circuitry	- Low tuning speed - Precise fluidic control requirement - Miniaturization limit
	None-MEMS mechanical tuning	- High structural freedom - Applicability on multiple application	- Slow tuning - Scaling limitation
Electrical tuning	PIN diode	- High tuning ratio - Fast tuning speed - Integration simplicity - Appropriate on broadband-switch	- Parasitic impedance above 10GHz - Bias distribution - Change of impedance rather than capacitance
	Varactor	- High tuning ratio - Fast tuning speed - Simplicity of integration - Continuous tuning capability	- Parasitic impedance above 10GHz - Bias distribution - Limitation on broadband spectrum
	Semiconductor	- Integration compatibility with various substrate - Ultrafast modulation	- Passive for RF frequencies - Non-linear effects - High-carrier density requirement over THz
	Superconductor	- Sufficient dynamic behavior - Highly desirable features - Ultra low losses	- Performance dependency over Tc - Thickness scaling issues - Josephson nonlinearity
Material tuning	Liquid crystal	- Wide spectral range - Large birefringence - Agile tuning speed	- Narrow liquid crystal phase temperature - Issues on molecular anchoring (scaling difficulties)
	Phase change material	- Relatively fast switching - Considerable tuning ratio	- Temperature limitation - Requirements of specific fabrication and materials
	Optically pumped material	- Fast modulation	- Relatively low efficiency - Pumping intensity - Lifetime issues
	Graphene/ Caron nanotube	- Relatively high performance on nonlinear optical conversion - High performance in mid-infrared range	- Niche on applications - Requirement of preprocess on chemical potential - Unsuitability except for IR regime
	Ferroelectric/ magnetic	- Relatively fast switching - Considerable tuning ratio	- Temperature constraints

Furthermore, according to recent reviews on meta surface, a simple radar chart about a brief glimpse on characteristics of metasurface tuning mechanism is plotted. As shown in Figure 10, material-based tuning mechanism such as liquid crystal, PCM, and etc. has demerits relatively on tuning speed, fabrication difficulty, cost, and target frequency range. The electrical tuning mechanism secures a high tuning ratio, rapid tuning speed, relatively accessible fabrication level, and somewhat better cost-effectivity [104].

At any rate, metamaterial tuning mechanism using MEMS solution has quite strength on applying target frequency band, structural flexibility, relatively admissible tuning ratio, and relatively fair Q-factor value even though MEMS tuning

1.1.7   MEMS reconfigurable metamaterial

It is the MEMS-based tuning mechanism that fits the scale issue when considering the wavelength that performs through the metamaterial device among the mechanical tuning. The characteristic length of metal patterning, somehow called meta-atom unit cell, would mean a form factor of a piece of microdevice or the assemblage of microdevice spawned by MEMS solution which deliver impact on metamaterial performance and determines resonant frequency, and that the length maybe around 100 nm to 10 mm considering the resolution of photolithography, in which approximately converted to 10 GHz to 1,000 THz in spectral frequency.

In this article, even though it would be a desirable act to wholly scrutinize all the reference papers as much as possible, pre-study of many reference papers related to MEMS tunable metamaterial would have been omitted and not been

completed.

With deeply contemplating this in mind, research outcome of metamaterial based on MEMS tuning mechanism might be better to categorized in manner of spectral frequency and tuning ratio, tuning parameters, types of MEMS actuators and the driving energy source of the MEMS actuators. MEMS tuning technology.

In frequency perspective, majority of MEMS-driven reconfigurable metamaterial are focused in THz regime since the characteristic length of micrometer scale is converted to THz domain. Researches on GHz region seldomly published. In the second place, an electrostatic driven micro-cantilever is the most widely used MEMS actuators as a tuning mechanism [48, 105-120]. A few researchers utilized thermal energy or pneumatic driving [121-123]. Since the frequency shift inevitably requires a displacement change meaning mechanical reconfiguration, the simplest form is using cantilevers or minorly membrane as in vertical direction or is using comb-drive actuators as in lateral direction [43, 124-130]. Moreover, these micro-scale instrument inevitably involves the change of energy status and the most widely used methods are electrostatic and electrothermal driving mechanism. Thirdly, studies on a reconfigurable MEMS-driven metamaterial targets tuning of polarization, transmission, and frequency. Given these points, Table 1.2 summarizes recent studies related to keywords: MEMS, tunable, and metamaterial.

Author	[123] H Tao et al 2011 **	[124] T. Kan et al 2015	[125] Y. Fu et al 2011	[126] X. Zhao et al 2015 **	[127] W.M. Zhu et al 2012	[128] M. Zhang et al 2014	[129] W. Zhang et al 2012 **	26 [130] W. M. Zhu et al 2011
Cell size (μm)	72 × 72	170 × 170	50 × 25	40 × 10	28 × 28	80 × 50	50 × 60	19 × 19
Frequency regime	sub-THz	THz	THz	THz	THz	THz	sub-THz	THz
Tuning parameter	polarization	polarization	transmission	transmission	polarization	polarization	reflection	reflection
Resonance type								LC, dipolar
Resonance frequency f_{res}	0.5 THz	1.0 THz	TE 1.28 THz TM 1.40 THz	1.1, 1.4 THz TE coupled	3.11 THz		0.76, 1.16 THz TE	2.2 THz TE
Frequency change Δf		$\Delta\theta \sim 10°$	TE 0.3 THz TM 0.25 THz	0.05, 0.1THz	0.38 THz			0.3 THz TE
Tuning ratio $\Delta f/f_{res}$			TE 0.31 TM 0.22	0.05, 0.07	0.12			0.14
Q-factor			TE 13.8 TM 7.8					10
Meta-atom shape	DSRR array	spiral ring array	ASRR 2 layers, array	BC- SRR 2 layers, array	Cross-shape array	slab pattern	U-shape DSRR, array	U-shape DSRR, array
Material	Au, Si	Au, Si	Al, SOI	Au, Si	Al, Si	Al, SOI	Al, SOI	Al, SOI
Actuating direction	vertical bidirectional	vertical bidirectional	lateral in-plane	lateral in-plane	lateral in-plane	lateral in-plane	lateral in-plane	lateral in-plane
Actuator type	cantilever	cantilever	comb-drive	comb-drive	comb-drive	comb-drive	comb-drive	comb-drive
Max. displacement	80°	55 μm	20μm	18μm	5μm	25 μm	30μm	8 μm
Actuating energy	thermal	pneumatic	electrostatic	electrostatic	electrostatic	electrostatic	electrostatic	electrostatic
Driving V or I		±10 Pa	20 V	60 V	10 V	26V	10V	10V
Modulation time		120 kHz	1 ms					1kHz

Table 1.2. Summary of MEMS reconfigurable metamaterial [123-130]

1.1.8   Tunable metamaterial absorber

Figure 1.9 shows the summary of the tunable metamaterial absorbers in terms of tuning mechanism and applied frequency range. Metamaterial-based absorbers can accomplish both high absorptivity and a thin thickness with a simple and low-cost fabrication. However, the metamaterial-based absorber has a decisive disadvantage of narrow bandwidth caused by the resonance frequency characteristic. To overcome the drawbacks of narrow bandwidth, studies on tunable metamaterials have been actively presented.

The tuning of a metamaterial absorber can be categorized into four methods. The first method is electrical tuning. Because the electrically tuning system uses electrical active components such as a varactor or PIN diodes [84, 131, 132], a metamaterial absorber with electrical tuning has a fast tuning speed, wide tuning ratio, and high absorption range. However, these electrical components have a limitation above the 10 GHz range due to the bias distribution and parasitic impedance. Second, there is a method to realize a tunable metamaterial absorber by changing the material properties using liquid crystals [133, 134], phase change material [80, 135-137], graphene [138, 139], etc. Even though these material tuning metamaterial absorbers have a wide spectral range, a relatively fast switching speed, and a considerable tuning ratio, these materials have major disadvantages in temperature constraints and unusual fabrication difficulties. Moreover, some studies have applied a fluidic platform for tuning metamaterial absorbers [140]. The aqueous solution injected above the metamaterial unit cell can dramatically affect the refractive index. Though this fluidically tunable metamaterial has an exceptional

tuning range, the fluidic tuning has an extremely low tuning speed and difficulties with integration with other applications. The most straightforward way to achieve a tunable metamaterial absorber is to mechanically reconfigure the metamaterial unit cell. The deformation of the unit cell can simply lead to a resonance frequency change without high loss, continuous power consumption, and temperature limitations.
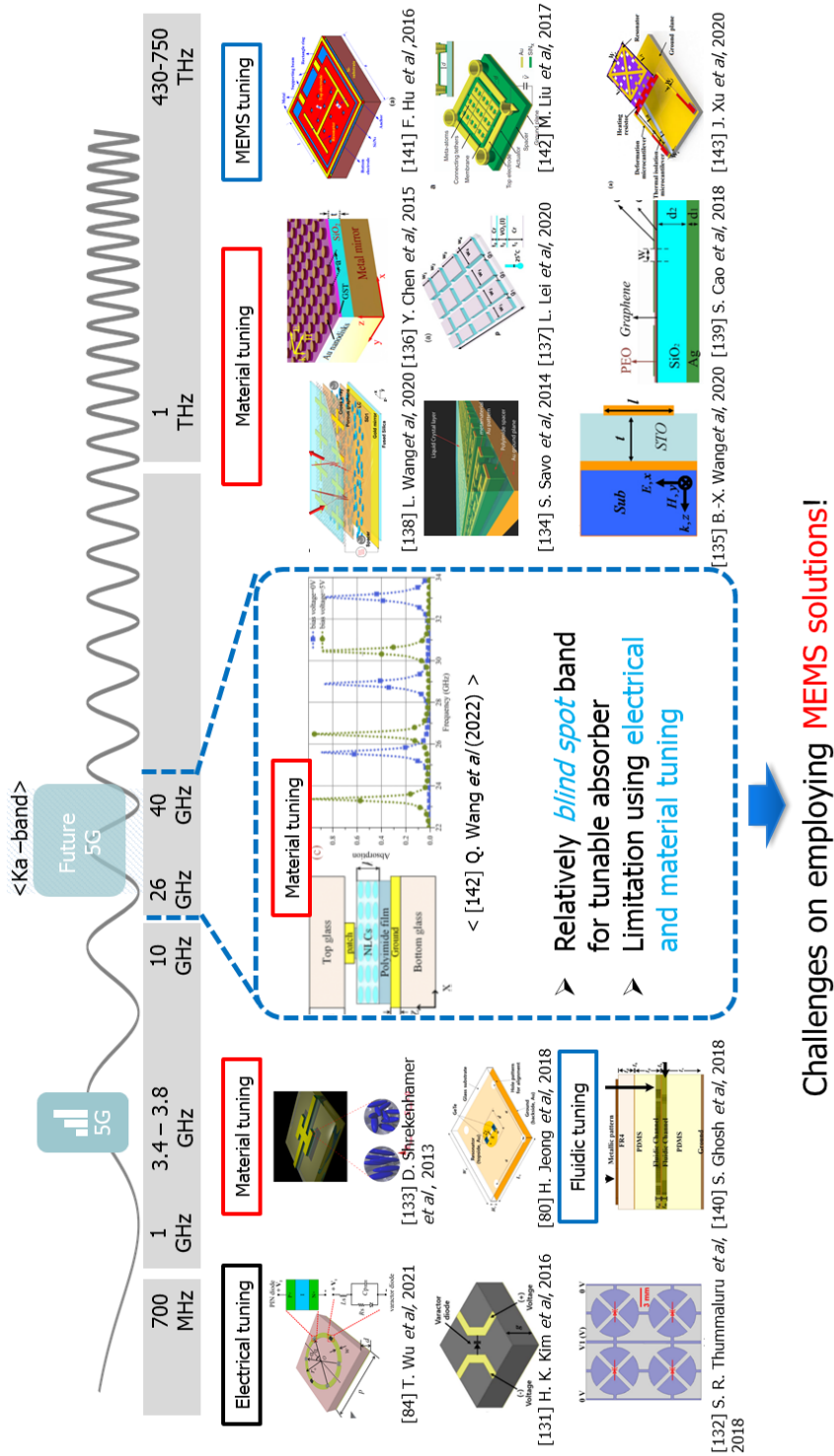
Figure 1.9. Tuning mechanism and applied frequency band of tunable metamaterial absorber

1.1.9   MEMS reconfigurable metamaterial absorber

Studies related to MEMS-driven tunable metamaterial absorbers have been published [141-143]. These studies apply cantilever beams as out-of-plane actuators for the unit cell reconfiguration. However, these MEMS-based tunable metamaterial absorbers are only found in the sub-THz and THz-regime because the MEMS fabrication solution is suitable for only a characteristic length ($\lambda/4$) of the sub-THz and THz regime. Table 1.3 summarizes each MEMS tunable metamaterial absorber.

Table 1.3. Summary of MEMS reconfigurable metamaterial absorber
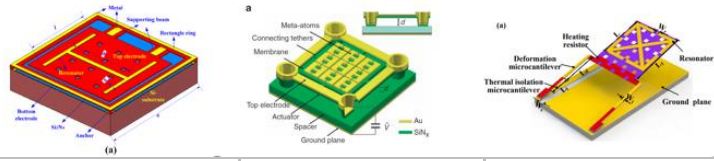
	[141] F. Hu *et al.*, 2016	[142] M. Liu *et al.*, 2017	[143] X. LXu *et al.*, 2020
	Sub THz regime	THz regime	THz regime
Resonance frequency (f)	$f = 0.61$ THz	$f = 1.168$ THz	$f = 0.68$ THz
Wave length (λ)	$\lambda = 491$ μm	$\lambda = 261$ μm	$\lambda = 441$ μm
Characteristic length ($\frac{\lambda}{4}$)	122.75 μm	65.25 μm	110.25 μm
Meta-atom unit cell	160×90 μm^2	60×60 μm^2	80×105 μm^2
Type of MEMS actuator	cantilever	Suspended membrane	cantilever
Driving of unit cell	Individual unit cell driving	9 unit cells set driving	Individual unit cell driving
Deflection direction	Vertical, out-of-plane	Vertical	Vertical, out-of-plane
Maximum deflection (δ, ϕ)	$\phi = 0.6°$	$\delta = 3$ μm	$\phi = 5.4°$
Fabrication	HF wet etching	Oxygen plasma	Oxygen plasma
Sacrificial layer	Phosphosilicate glass	Polyimide	Polyimide
Tuning range	$\Delta f = 0.06$ THz	$\Delta f = 0.188$ THz	$\Delta f = 0.01$ THZ
Tuning ratio	$\frac{\Delta f}{f} = 9$ %	$\frac{\Delta f}{f} = 16$ %	$\frac{\Delta f}{f} = 15\%$
Peak absorptivity	About 60 %	Up to 80 %	95.6%
Driving voltage / current	$V_d = 20$ V	$V_d = 250$ V	$I = 1200$ mA

1.1.10 Tunable metamaterial absorber for Ka-band

This Ka-band is a blind spot for achieving a tunable metamaterial absorber because it is not quite easy to apply the electrical, material, fluidic, and mechanical tuning methods for the millimeter-wave length. Today, a tunable metamaterial absorber for the Ka-band is only achieved by utilizing liquid crystals [144]. In this study, a Ka-band tunable metamaterial absorber is implemented by using the change in the relative permittivity of nematic liquid crystals according to the application of a bias voltage. Even though this approach has advantages of low loss, mature fabrication, and relatively large tuning range, it has a limitation on temperature sensitivity and requires continuous energy consumption for frequency tuning, Summary of this Ka-band tunable metamaterial absorber using liquid crystal is briefly explained in Figure 1.10 and Table 1.4.
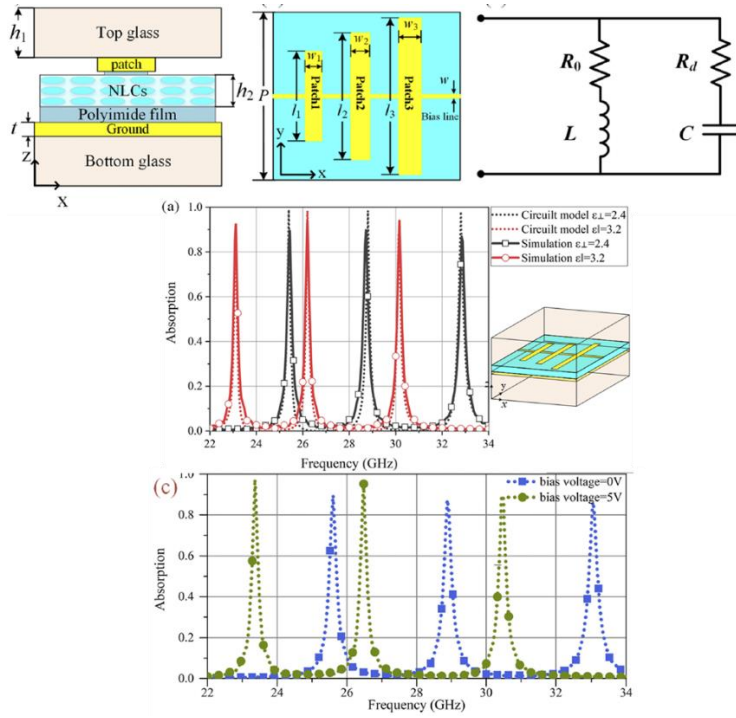
Figure 1.10. Structure and performance summary of Ka-band tunable metamaterial absorber using liquid crystal

Table 1.4. Summary on Ka-band tunable metamaterial absorber using liquid crystal

『Tunable triple-band millimeter-wave absorbing meta-surface based on nematic liquid crystal』	
Tuning method	Material tuning (Nematic liquid crystal)
Resonance frequency	$f_1 = 25.4$ GHz, $f_2 = 28.7$ GHz, $f_3 = 32.8$ GHz
Tuning ratio	$\frac{\Delta f}{f_1} = 9.5\%$, $\frac{\Delta f}{f_2} = 9.1\%$, $\frac{\Delta f}{f_3} = 8.58\%$
Bias voltage	DC 5V
Summary	Explanation by change of relative permittivity of nematic liquid crystal in short axis($\varepsilon_\perp = 2.4$) and long axis($\varepsilon_\parallel = 3.2$) Proof of circuit model and full wave simulation - Calculation of inductance ($L_1 = 4.99$ pH, $L_2 = 5.7$ pH, $L_3 = 6.4$ pH) and capacitance ($C_1 = 3.77$ pF, $C_2 = 5.37$ pF, $C_3 = 6.09$ pF) of metal strip
Advantage	- Low loss of nematic liquid crystal - Mature fabrication of liquid crystal - Relatively large tuning range
Disadvantage	- Temperature sensitivity of the effective permittivity of nematic liquid crystal - Continuous dc bias

1.2 Originality and contribution

In this study, we attempt for the first time to exploit the MEMS solution for realizing a frequency tunable metamaterial absorber for the Ka-band (26.5 – 40 GHz) which is a blind spot for the tunable absorber. We resolved the scaling issue of applying the MEMS solution in the Ka-band by designing the SRR unit cell to have a sub-mm scale stress-induced cantilever. Stress-induced cantilevers with initial out-of-plane deflection act as variable capacitances in SRR to realize frequency tunability. This realization is achieved by the ashing process with specific conditions. However, the general cantilever shape has limitations in terms of high uniformity and reproducibility. In this paper, the cantilever shape is constructed with semicircular geometry to improve uniformity and reproducibility. Moreover, an incremental etching hole is introduced to release the distribution of stress generation during the plasma process. With an improved realization of the semicircular cantilever, the tuning range and the tuning ratio of the Ka-band tunable metamaterial absorber have shown sufficient results compared to other absorbers in Ka-band.

1.3 Document structure

This dissertation is specifically organized by following research contents.

In chapter 2 of this thesis, the evolution of the shape of the stress-induced cantilever will be discussed.

In chapter 3, the 1st design of Ka-band MEMS tunable metamaterial absorber with stress-induced cantilever array will be thoroughly explained.

In chapter 4, the 2nd design of Ka-band MEMS tunable metamaterial absorber with stress-induced rectangular cantilever with incremental etch hole spacing to overcome the characteristic of having a larger width than length will be introduced and described in detail.

In chapter 5, a final evolved design of Ka-band MEMS tunable metamaterial absorber with stress-induced semicircular cantilever with incremental etch hole spacing to maximize uniformity would be described.

Finally, in chapter 6, a conclusion and eventual summary of this total dissertation on MEMS-driven metamaterial absorbers are organized.

CHAPTER 2. Stress-induced sub-mm scale cantilever

2.1 Initial design

As widely acknowledged, many papers presented studies on MEMS cantilevers with hundreds of micrometer-scale lengths. These MEMS cantilevers are released by various fabrication approaches. First of all, research based on wet-etching has been widely attempted. However, the larger the cantilever, the more possible the cantilever to fail by stiction from the high surface energy of wet chemicals. Secondly, cantilever releasing by vapor gas has also been widely studied. Despite its simplicity, it is not appropriate for a monolayer metal cantilever structure to generate sufficient deflection because the deflection of the cantilever is mainly dependent on the intrinsic stress of the metal film. Instead, some studies focus on the mechanical properties of MEMS cantilevers with an out-of-plane deflection by using plasma ashing [145, 146]. Figure 2.1 shows the results of MEMS cantilever beams fabricated by plasma ashing. This cantilever releasing method based on plasma ashing is a very strong tool since the deflection can be controlled by the various conditions of the ashing processes such as ashing cycles and ashing times. In this paper, the plasma ashing process which etches photoresist-based sacrificial layer will be utilized to realize cantilevers with deflection.
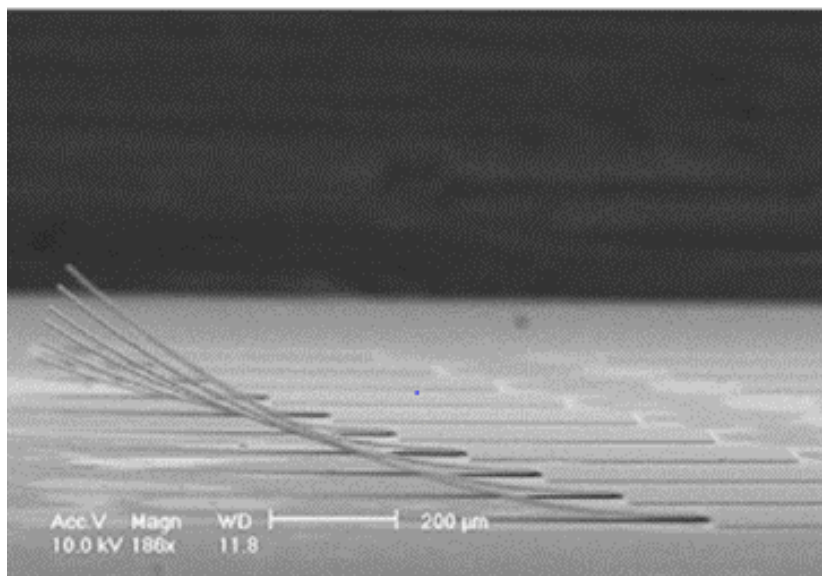
Figure 2.1. Deformation of electroplated MEMS cantilever beams released by plasma ashing [145]

Furthermore, a sub-mm scale cantilever with a sufficient stress gradient is required to work in the Ka-band regime. The initial design of the cantilever beam is tested to have 0.4 mm in length and 0.8 mm in width with a 20 μm square etch hole and 20 μm square etch hole.

As shown in Figure 2.2(a), Asher 1 (V15-G, Plasma finish) in Interuniversity Semiconductor Research Center is used for releasing AZ 4330 photoresist sacrificial layer. The plasma power induced by 2.45 GHz microwave, the chamber pressure, and the oxygen gas (O_2) flow are 300W, 150 Pa, and 150ml/min, respectively. The maximum ashing process time is 10 min, due to the excessive heat generation. The cantilever beam is released by 1 to 3 cycles of 10 min ashing cycles. The samples of absorbers are loaded in the mesh as shown in Figure 2.2(b).
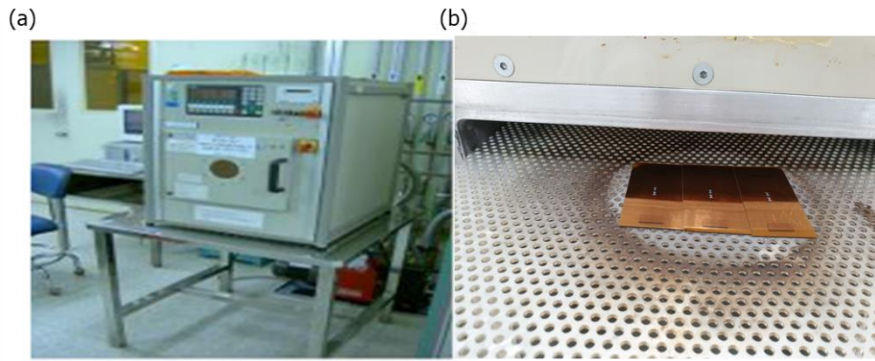
Figure 2.2. (a) Photographs of Asher 1 (b) Sample loading in asher chamber

Beam width affects lateral stress no matter how carefully and thoroughly releasees the cantilever beam as shown in Figure 2.3. The solution to break through difficulties is to cut one cantilever into a suitable size, where the length is much longer than the width.
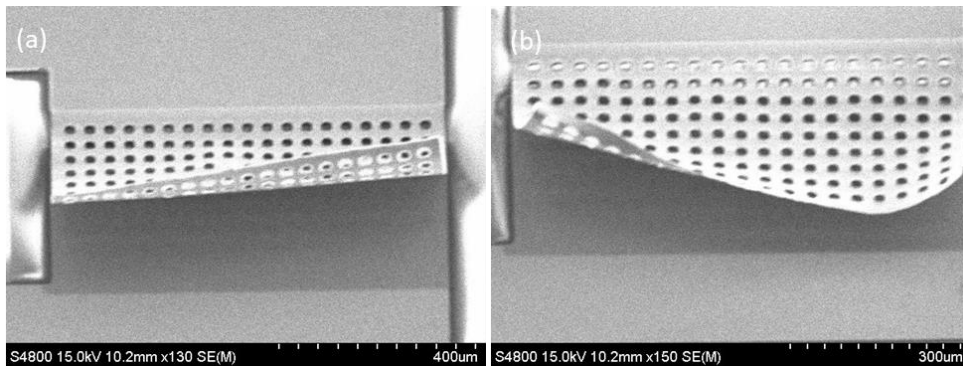
Figure 2.3. SEM image of sub-mm scale cantilever after releasing: (a) Non-uniform curvature of Au film (b) Strong stress generation in the lateral axis

2.2 Cantilever arrays with stress gradient

2.2.1 Preliminary experiment

Various experiments on cantilever beam shapes, metal selection, and beam parameters such as width or thickness have been conducted to improve the non-uniformity of the cantilever shown in the previous section. Various metal types such as gold, titanium, aluminum, gold-titanium bilayer, and chromium-titanium bilayer are tested to find out the most suitable for generating appropriate stress gradient. Also, thickness difference creates unpredictable stress gradient direction. Especially, a number of arrays is something to consider because more number of an array the more unfavorable to achieve uniformity as shown in Figure 2.4.
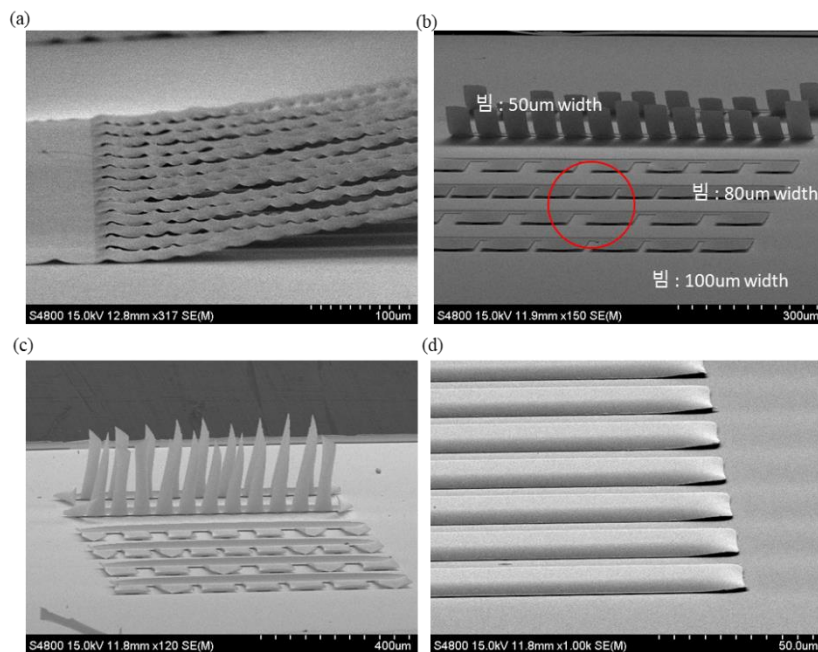
Figure 2.4. Failure examples: (a) Excessive ripple generation in Au film (b) Failure of releasing broad width cantilever beams (c) Excessive stress generation in titanium film (d) Opposite stress gradient in titanium-gold bilayer

2.2.2 Design

Considering previous experiments, the length, width, and the space of the cantilever beam are decided to be $l_b = 400$ μm, $w_b = 50$ μm, and $s = 12$ μm. Through experiments, it was determined that 1 um thickness of aluminum was the optimal film thickness for out-of-plane deformation. The initial design is described in schematic as shown in Figure 2.5.
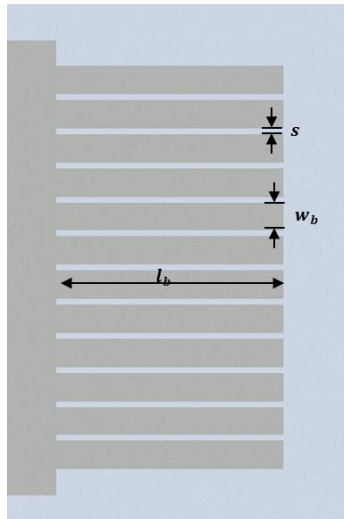
Figure 2.5. Parameters for the 1st design of cantilever arrays with stress gradient

2.2.2 Fabrication results

A stress-induced semicircle shape cantilever beam with 800 μm in length and 400 μm in width is fabricated by surface micromachining. The cantilever beam is composed of aluminum with a 1 μm thickness film. The Al film was sputtered above a 3.4 μm thick AZ4330 photoresist sacrificial layer which is thermally cured over 1 hour in 200 °C after spin coating at 5,000 rpm. The condition of the ashing process is the same as in Section 2.1. A total of 2 cycles of plasma ashing process are performed at intervals of one day for 10 minutes per cycle. Figure 2.6(a) is the SEM image of cantilever arrays released with curvature. Even though the sample in Figure 2.6(b) is released with relatively good uniformity, the majority of samples have failed to achieve array-to-array uniformity or beam-to-beam uniformity.
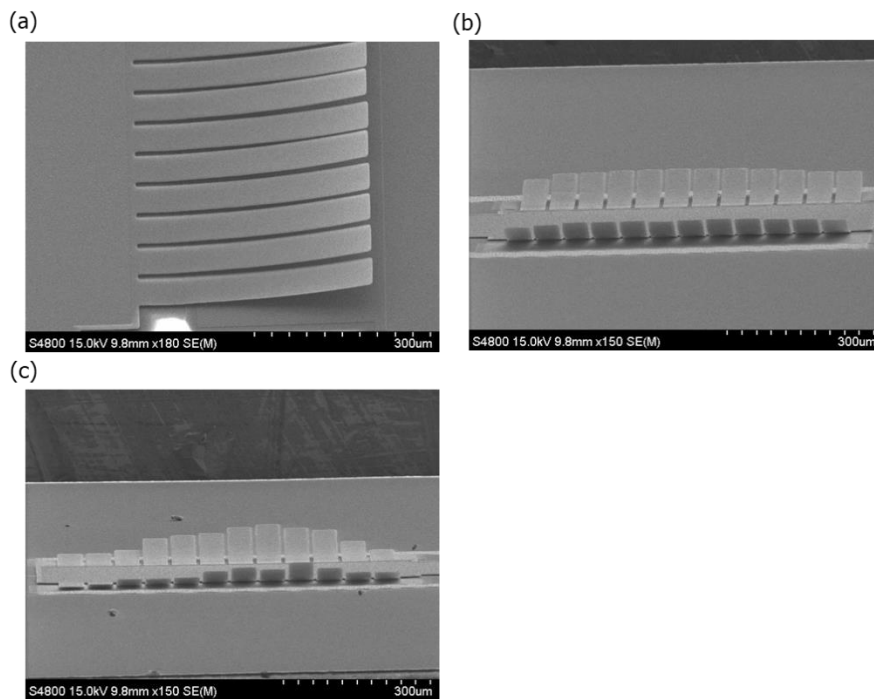
Figure 2.6. SEM image of fabricated cantilever array (a) lateral view of cantilever array with stress gradient (b) Cantilever array with better uniformity (c) Cantilever array with worse uniformity

2.3 Rectangular shape sub-mm scale cantilever with incremental etch hole spacing

2.3.1 Preliminary experiment

Low plasma power oxygen plasma ashing in RIE etcher (RIE 80 plus, Oxford) is tested to investigate the uniformity of the cantilever. RF power in the RIE chamber is 200 W and the oxygen flow is about 150 ml/min. Despite the expectation that less plasma power of the RIE process will improve uniformity compared to high power ashing chamber and the shape of the cantilever eliminates lateral stress generation, the etched holes at equal intervals are not conducive to the fabrication of the cantilever because the etch rate on the anchor side is faster. Figure 2.7 shows the remaining level of the sacrificial layer as the cycle increase. Therefore, a low plasma power process is not a good approach because it takes a long time if the etch pattern is not considered. Figure 2.8 shows that excessive oxygen plasma etching can deform metal film properties. Thus, time should be considered as an affecting variable in cantilever releasing.
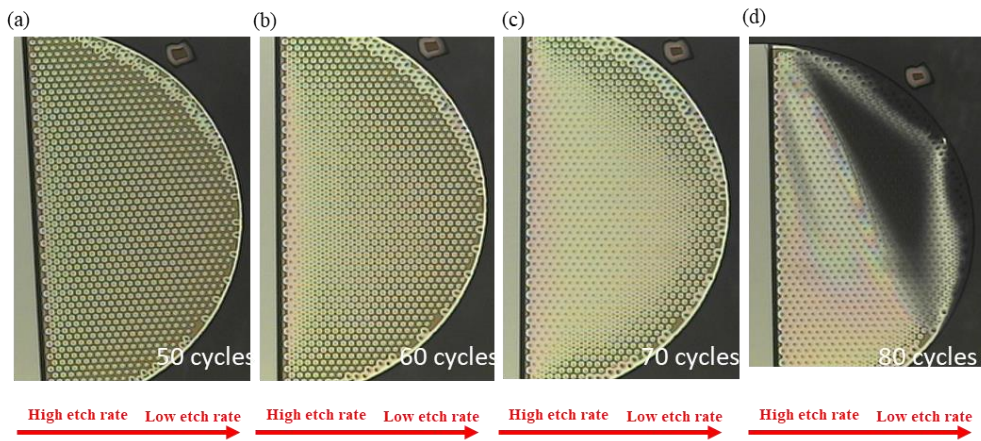
Figure 2.7. Microscope images after sacrificial layer cyclic etching in cantilever beams with equally spaced etching holes under low plasma power (a) 50 cycles (b) 60 cycles (c) 70 cycles (d) 80 cycles
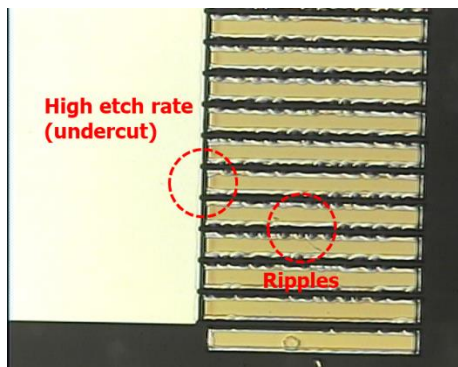
Figure 2.8. Ripple generation under long plasma etch time

2.3.2 Design

To release the cantilever beam as uniformly as possible by alleviating the thermal effect, the etch hole and the space are incrementally arranged from the edge. Figure 2.9 (a) shows the parameters for the etch hole array and spaces. The etch hole size is $d = 8$ μm. The first space length between the edge and the etch hole of the 1st column is $s_1 = 6$ μm. The second space length between the etch holes in the first column and the etch hole in the second column is $s_2 = 8$ μm. With the same principle, the space length is set to be ascending from the open end of the cantilever to the anchor of the cantilever by 2 μm as shown in Figure 2.9 (b). Summarized in Table 2.1, the detailed space is $s_3 = 10$ μm, $s_4 = 12$ μm, $s_5 = 14$ μm, $\cdots$, $s_{12} = 28$ μm, and $s_{13} = 30$ μm. These incremental changes of the etch hole space lead to sequential releasing from the edge. The designing above led to the total number of 391 etch holes and 95.9% of effective area. Effective area calculation is important in absorber samples which will be discussed later.
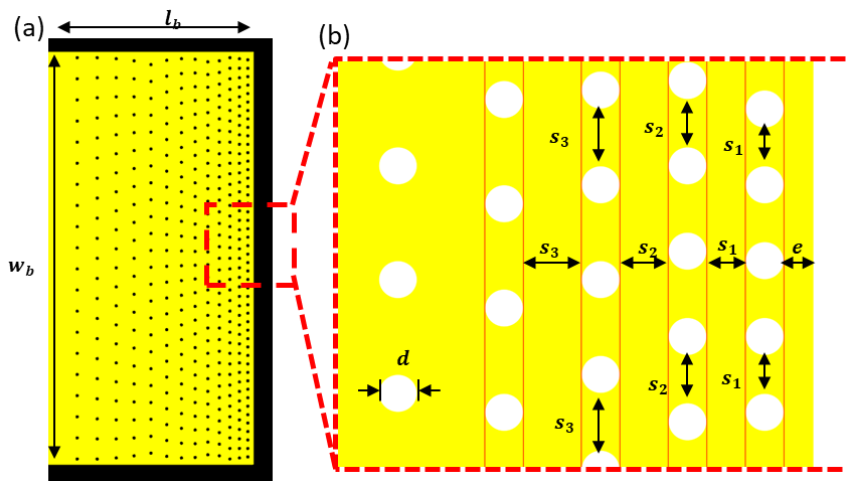
Figure 2.9. (a) Design parameters of cantilever beam (b) Etch hole arrangement

Table 2.1. Dimension and etch hole shape of rectangular cantilever beam

Parameters	Description	Value	Unit
d	The diameter of etch hole	8	μm
w_b	The width of the beam	800	μm
l_b	The length of the beam	400	μm
e	The length of the edge and 1st column	6	μm
s_1	The space between 1st column and 2nd column, The space between etch holes in 1st column	8	μm
s_2	The space between 2nd column and 3rd column, The space between etch holes in 2nd column	10	μm
s_3	The space between 3rd column and 4th column, The space between etch holes in 3rd column	12	μm
s_4	The space between the 4th column and the 5th column, The space between etch holes in the 4th column	14	μm
s_5	The space between the 5th column and the 6th column, The space between etch holes in the 12th column	16	μm
s_6	The space between the 6th column and the 7th column, The space between etch holes in the 6th column	18	μm
s_7	The space between the 7th column and the 8th column, The space between etch holes in the 7th column	20	μm
s_8	The space between the 8th column and the 9th column, The space between etch holes in the 8th column	22	μm
s_9	The space between the 9th column and the 12th column, The space between etch holes in the 9th column	24	μm
s_{10}	The space between the 10th column and the 11th column, The space between etch holes in the 10th column	26	μm
s_{11}	The space between the 11th column and the 12th column, The space between etch holes in the 11th column	28	μm
s_{12}	The space between the 12th column and the 13th column, The space between etch holes in the 12th column	30	μm
t_b	The thickness of the cantilever beams	1	μm

2.3.2 Fabrication

A stress-induced rectangular shape cantilever beam with 800 μm in length and 400 μm in width is fabricated by surface micromachining. The cantilever beam is composed of aluminum with a 1 μm thickness film. The Al film was sputtered above a 3.4 μm thick AZ4330 photoresist sacrificial layer which is thermally cured over 1 hour in 200 °C after spin coating at 5,000 rpm.

The Al thin film deposited by sputtering inevitably has residual stress during the deposition process. Residual stress is affected by various factors such as the thickness or shape of the thin film, the oxidation level of the thin film, the surface crystallization related to the pressure or temperature during the process, the difference in the thermal expansion coefficient, and impurities on the surface. The MEMS cantilever is subjected to significant thermal deformation in the additional oxygen plasma ashing process. The ashing process is conducted at a 300 W RF power, and an oxygen flow rate of 150 sccm with a V15-G plasma asher (SIEMENS). Previous studies have shown that the deflection of the cantilever is affected by complicated factors such as the plasma temperature distribution and the changes in the surface metal properties [146].

To release the cantilever beam as uniformly as possible by alleviating the thermal effect, a cyclic ashing process is performed. The step time of the ashing is 5 min per cycle. Sufficient cooling of the asher chamber is conducted for more than 10 min between steps.

Figure 2.10 shows the microscope image of a rectangular cantilever changing over the cycle from 0 to 9 cycles. The beam bending starts from the open-end tip of the cantilever. As the area of the dark part increases, the deflection increases. Figure 2.11 is a microscope image taken from the backside, and it can be seen that the sacrificial layer is released from the beam edge.
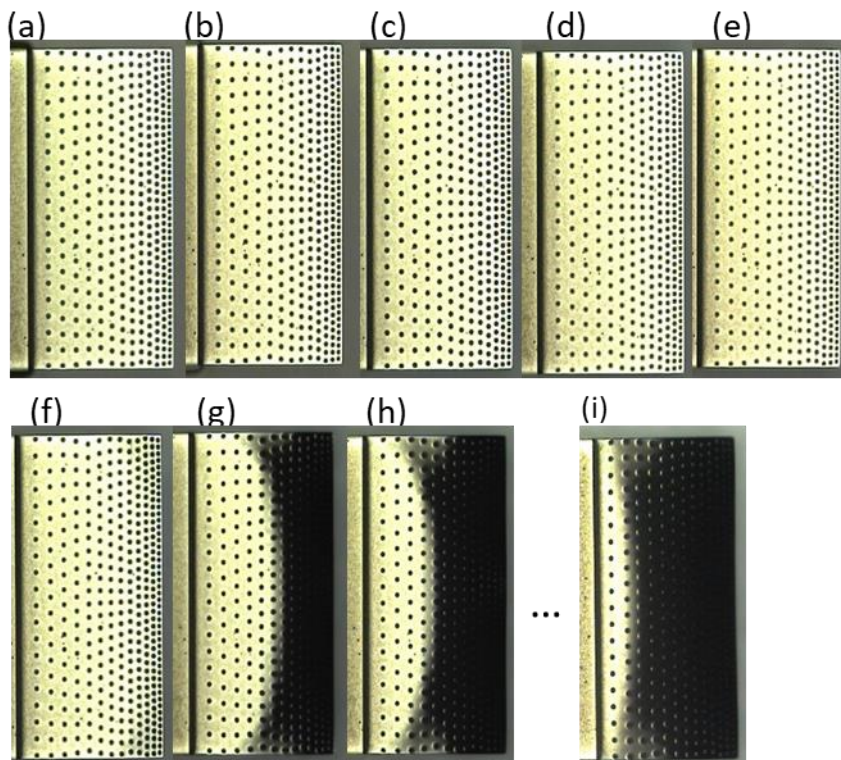
Figure 2.10. Top view optical images of cantilevers after cycles of ashing process: (a) 0 cycle (b) 1 cycle (c) 2 cycles (d) 3 cycles (e) 4 cycles (f) 5 cycles (g) 6 cycles (h) 7cycles (i) 9 cycles
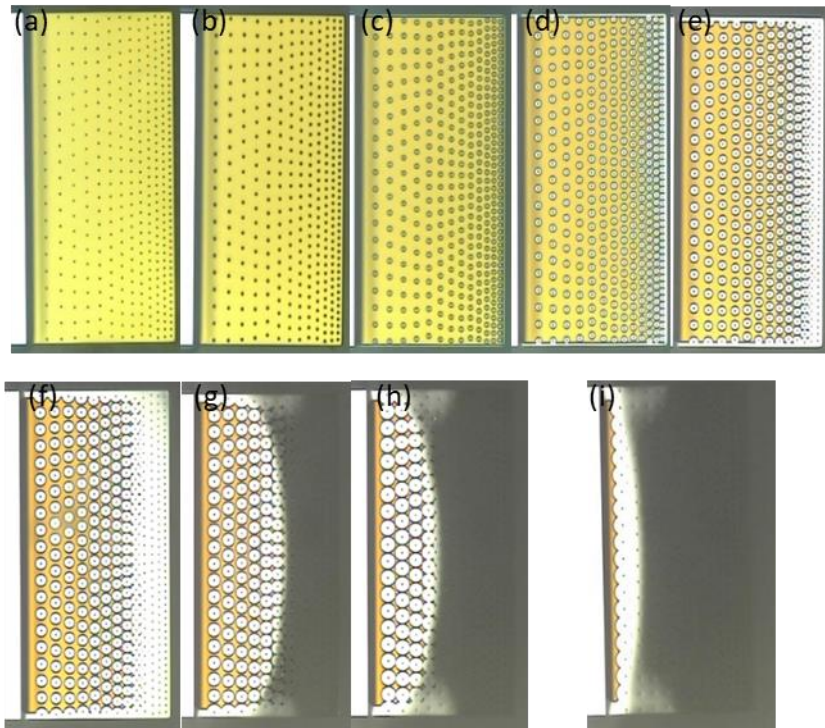
Figure 2.11. Backside view after of photoresist sacrificial layer residues after cycles of ashing process: (a) 0 cycle (b) 1 cycle (c) 2 cycles (d) 3 cycles (e) 4 cycles (f) 5 cycles (g) 6 cycles (h) 7cycles (i) 9 cycles

For more accurate investigation, sequential releasing of the rectangular cantilever is captured by SEM as shown in Figure 2.12. Beam deflection starts from the 5th cycle. The profile of the open end of the cantilever beam is measured using a 3D surface profiler as shown in Figure 2.13. The profile in Figure 2.13 (c) indicated that stress majorly acts in the lateral direction, showing a corrugated profile.
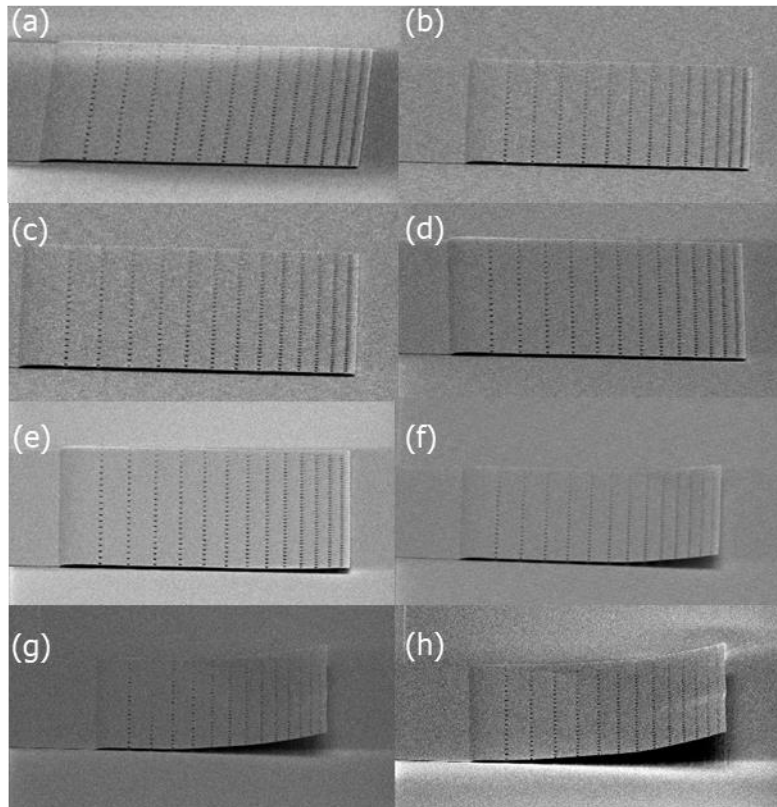
Figure 2.12. SEM images of MEMS cantilevers with semicircle shape after cycles of ashing process: (a) 0 cycle (b) 1 cycle (c) 2 cycles (d) 3 cycles (e) 4 cycles (f) 5 cycles (g) 6 cycles (h) 7cycles (i) 9 cycles
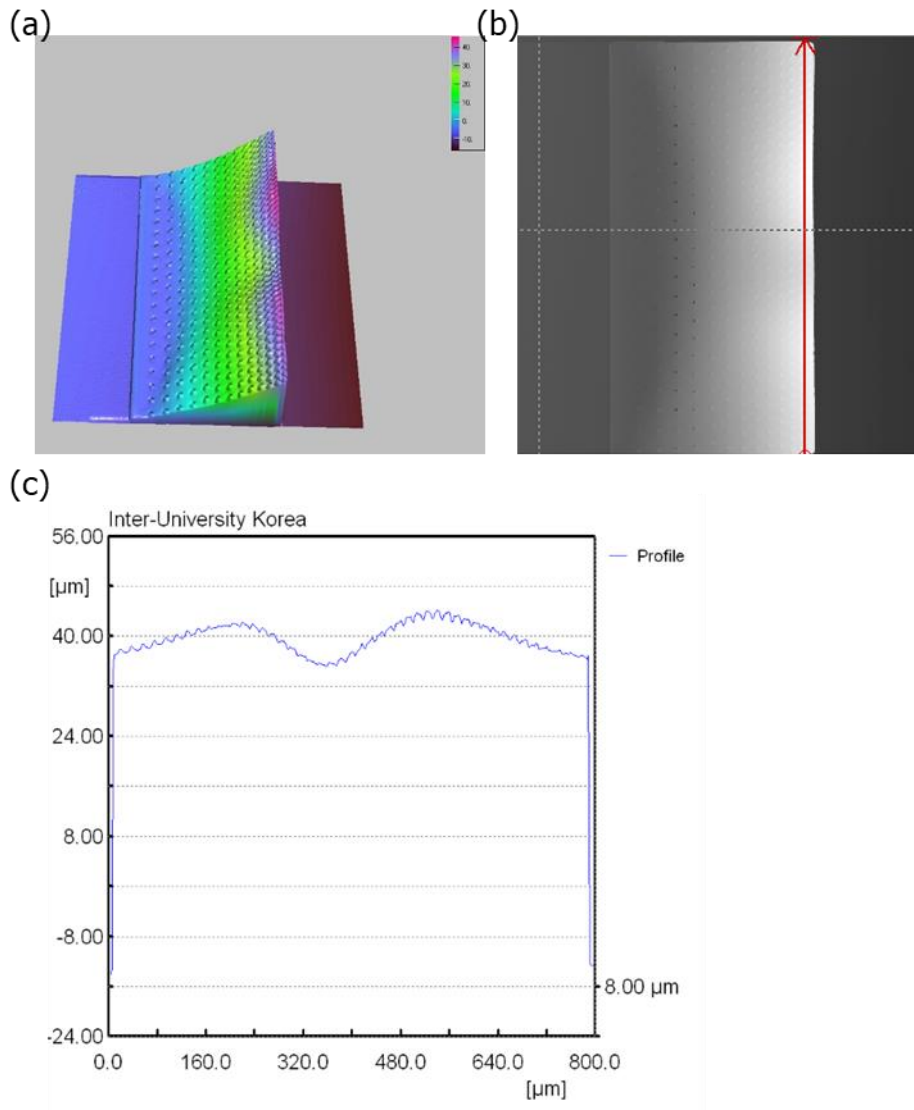
Figure 2.13. (a) Optical 3D surface profile of released MEMS cantilever (b) Profile measurement for the open end of cantilever (c) Profile of open end of rectangular cantilever

2.4 Semicircular sub-mm scale cantilever with incremental etch hole

2.4.1 Design of semicircular sub-mm scale cantilever with incremental etch hole

To release the cantilever beam as uniformly as possible by alleviating the thermal effect, the etch hole and the space is incrementally arranged from the edge. Figure 2.14 (a) shows the parameters for the etch hole array and spaces. The etch hole size is $d = 8$ μm. The first space length between the edge and the etch holes within the 1st radius is $s_1 = 6$ μm. The second space length between the etch holes in the first radius and the etch hole within the second radius is $s_2 = 8$ μm. With the same principle, the space length is set to be ascending from the edge of the cantilever to the anchor of the cantilever by 2 μm. As shown in Figure 2.14 (b). The detailed space is $s_3 = 10$ μm, $s_4 = 12$ μm, $s_5 = 14$ μm, ⋯, $s_{12} = 28$ μm, and $s_{13} = 30$ μm. These parameters are organized in Table 2.3. These incremental changes of the etch hole space lead to sequential releasing from the edge. Designing above lead to total number of 451 etch hole and 93.9% of effective area.
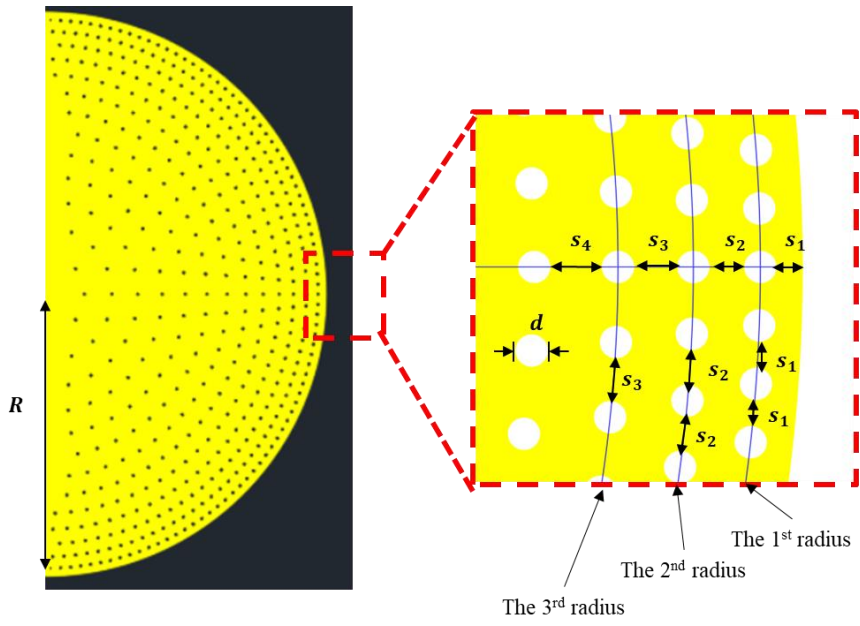
Figure 2.14. (a) Design parameters of cantilever beam with semicircle shape (b) Etch

hole arrangement

Table 2.2. Dimension and etch hole shape of semicircle cantilever beam

Parameters	Description	Value	Unit
d	The diameter of etch hole	8	μm
s_1	The space between edge and the 1st radius, The space between holes in the 1st radius	6	μm
s_2	The space between the 1st radius and the 2nd radius, The space between holes in the 2nd radius	8	μm
s_3	The space between the 2nd radius and the 3rd radius, The space between holes in the 3rd radius	10	μm
s_4	The space between the 3rd radius and the 4th radius, The space between holes in the 4th radius	12	μm
s_5	The space between the 4th radius and the 5th radius, The space between the holes in the 5th radius	14	μm
s_6	The space between the 5th radius and the 6th radius, The space between holes in the 6th radius	16	μm
s_7	The space between the 6th radius and the 7th radius, The space between holes in the 7th radius	18	μm
s_8	The space between the 7th radius and the 8th radius, The space between holes in the 8th radius	20	μm
s_9	The space between the 8th radius and the 9th radius, The space between holes in the 9th radius	22	μm
s_{10}	The space between the 9th radius and the 10th radius, The space between holes in the 10th radius	24	μm
s_{11}	The space between the 10th radius and the 11th radius, The space between holes in the 11th radius	26	μm
s_{12}	The space between the 11th radius and the 12th radius, The space between holes in the 12th radius	28	μm
s_{13}	The space between the 12th radius and the 13th radius, The space between holes in the 13th radius	30	μm
R	The radius of the cantilever beam	390	μm
t_b	The thickness of the cantilever beams	1	μm

2.4.2 Fabrication

A stress-induced semicircle shape cantilever beam with radius an $R = 390$ μm is fabricated by surface micromachining. The cantilever beam is composed of aluminum with a 1 μm thickness film. The Al film was sputtered above a 3.4 μm thick AZ4330 photoresist sacrificial layer which is thermally cured over 1 hour in 200 °C after spin coating at 5,000 rpm. Figure 2.15 is a magnified microscope after cantilever beam patterning. The cantilever beam profile is measured by the surface profiler before the ashing process as depicted in Figure 2.16.
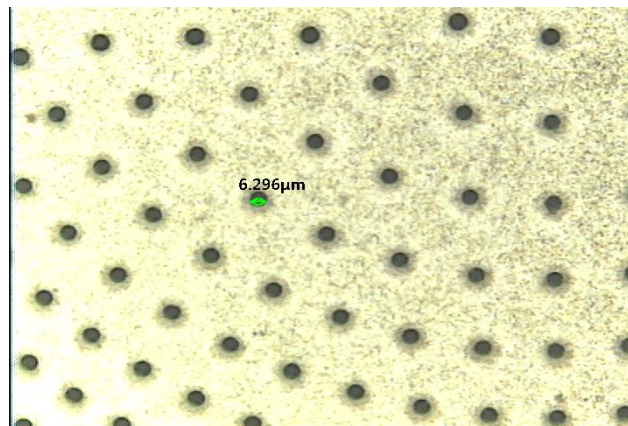
Figure 2.15. Magnified microscope image after cantilever patterning.
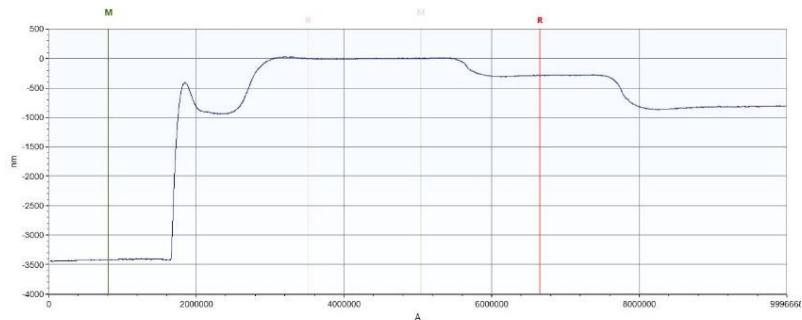
Figure 2.16. Cantilever profile before release

The ashing process is conducted at a 300 W RF power, and an oxygen flow rate of 150 sccm with a V15-G plasma asher (SIEMENS). Previous studies have shown that the deflection of the cantilever is affected by complicated factors such as the plasma temperature distribution and the changes in the surface metal properties.

To release the cantilever beam as uniformly as possible by alleviating the thermal effect, a cyclic ashing process is performed. The step time of the ashing is 5 min per cycle. Sufficient cooling of the asher chamber is conducted for more than 10 min between steps.

Figure 2.17 shows the microscope image of the semicircular cantilever changing over the cycle. The beam bending starts from the end tip of the cantilever. As the area of the dark part increases, the deflection increases. Figure 2.18 is a microscope image taken from the backside, and it can be seen that the sacrificial layer is released from the beam edge.
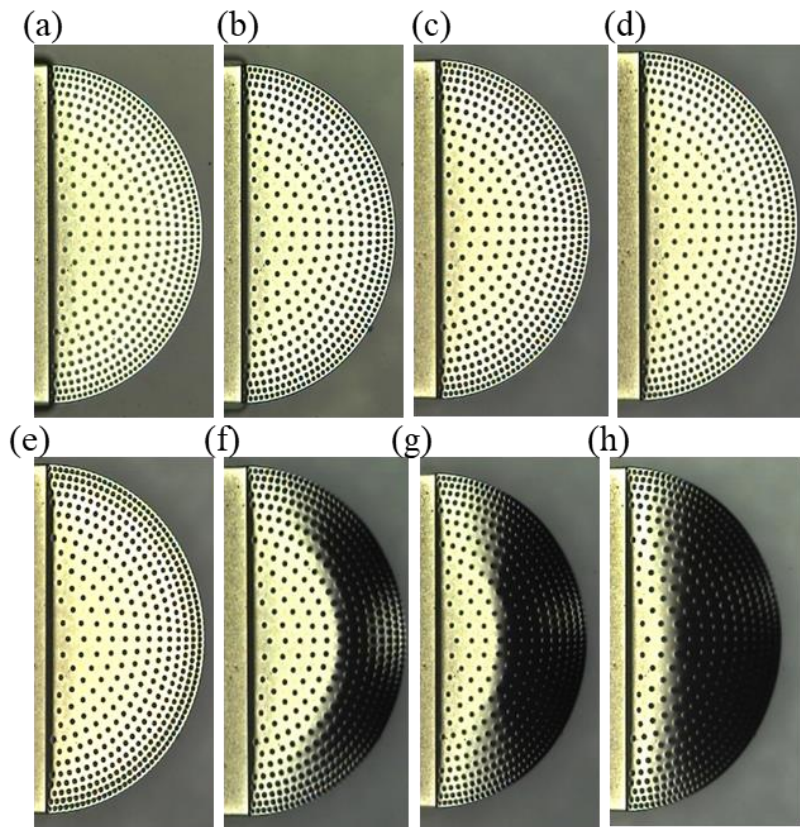
Figure 2.17. Top view optical images of cantilevers after cycles of ashing   process :
(a) 0 cycle (b) 1 cycle (c) 2 cycles (d) 3 cycles (e) 4 cycles (f) 5 cycles (g) 6 cycles
(h) 7cycles
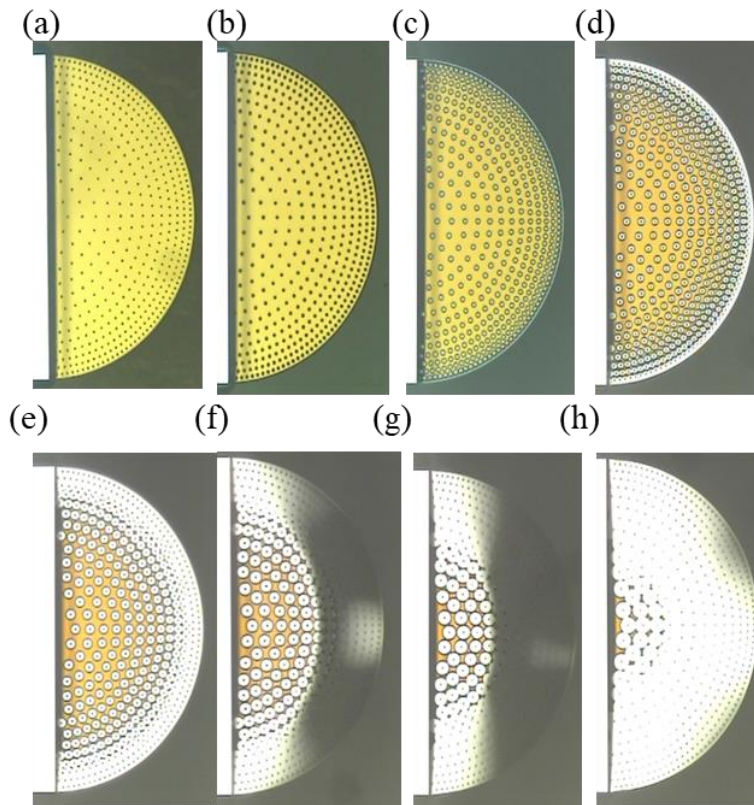
Figure 2.18. Backside view after of photoresist sacrificial layer residues after cycles of ashing process : (a) 0 cycle (b) 1 cycle (c) 2 cycles (d) 3 cycles (e) 4 cycles (f) 5 cycles (g) 6 cycles (h) 7cycles

Figure 2.19 (a) to (h) show the SEM image from 1 cycle to 7 cycles of the oxygen plasma ashing. SEM image indicated that sacrificial layer holding on semicircular cantilever unit 3 cycles of ashing process and starts to bend upward from 4 cycles of ashing. At each step, the maximum end-tip deflection is measured using an optical 3D surface profiler (NanoFocus uSurf) as described in Figure 2.20 (a). The cantilever shows no change until 3 cycles of ashing, but shows a deflection of 20 μm at 4 cycles, 31.7 μm at 5 cycles, 38.5 μm at 6 cycles, and 59.4 μm at 7cycles as shown in Figure 2.20 (b).
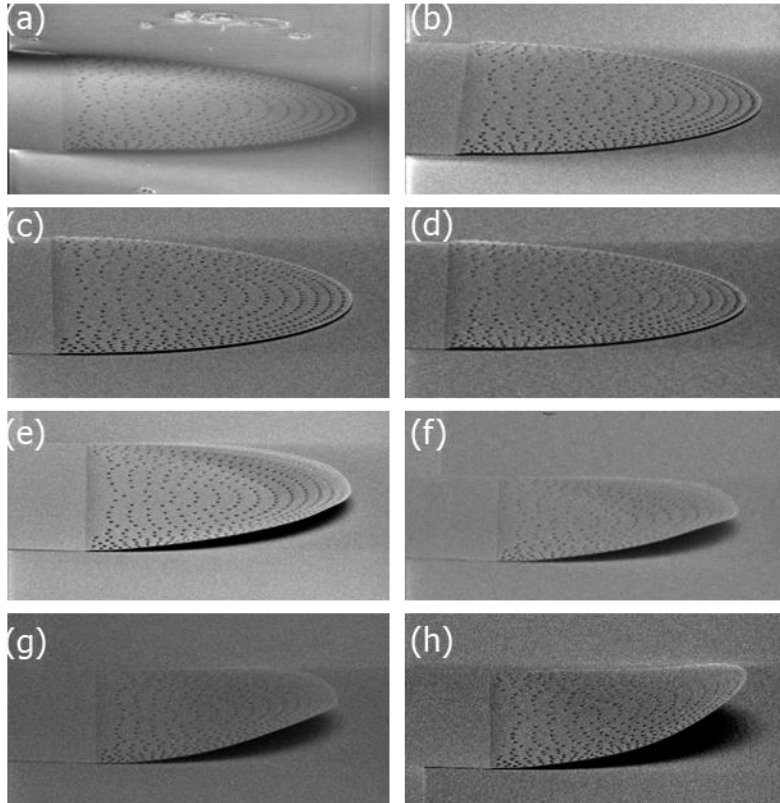
Figure 2.19. SEM images of MEMS cantilevers with semicircle shape after cycles of ashing process : (a) 0 cycle (b) 1 cycle (c) 2 cycles (d) 3 cycles (e) 4 cycles (f) 5 cycles (g) 6 cycles (h) 7cycles
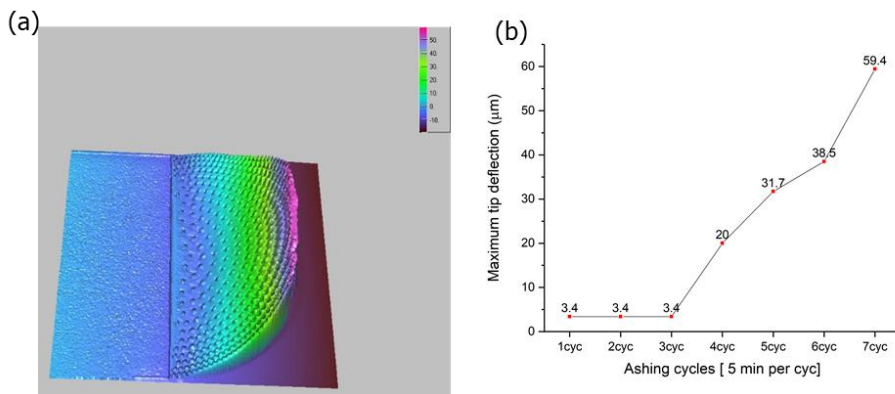
Figure 2.20. (a) 3D surface profile image of the stress-induced cantilever after 7 cycles of plasma ashing (b) Maximum deflection with cycle change

CHAPTER 3. The 1st design of MEMS tunable metamaterial absorber with cantilever arrays for continuous tuning

3.1 General overview

The entire schematic view of the proposed MEMS-driven frequency tunable metamaterial absorber is shown in Figure 3.1. The absorber is designed to be characterized with a waveguide measurement setup which will be described in section 3.4. From the bottom to the top, the absorber consists of an aluminum ground plane on the backside, a glass substrate, electrode pads/bias lines/driving electrodes which are all made of aluminum, silicon dioxide layers on the driving electrodes, and bias lines for electrical isolation, and two SRR unit cells. Each SRR unit cell contains 4 sets of aluminum cantilever arrays, and each array consists of 12 cantilevers as shown in Figure 3.1 (b). Each cantilever beam at the initial off-state is curved upward due to a stress gradient in the aluminum film as described in Figure 3.1 (c), bending downward to the on-state (Figure 3.1 (d)) when an electrostatic driving voltage is applied to the electrode pads. The resonant frequency shifts from the initial off-state to the on-sate due to the capacitance change that occurs by the deflection of the cantilever beams.
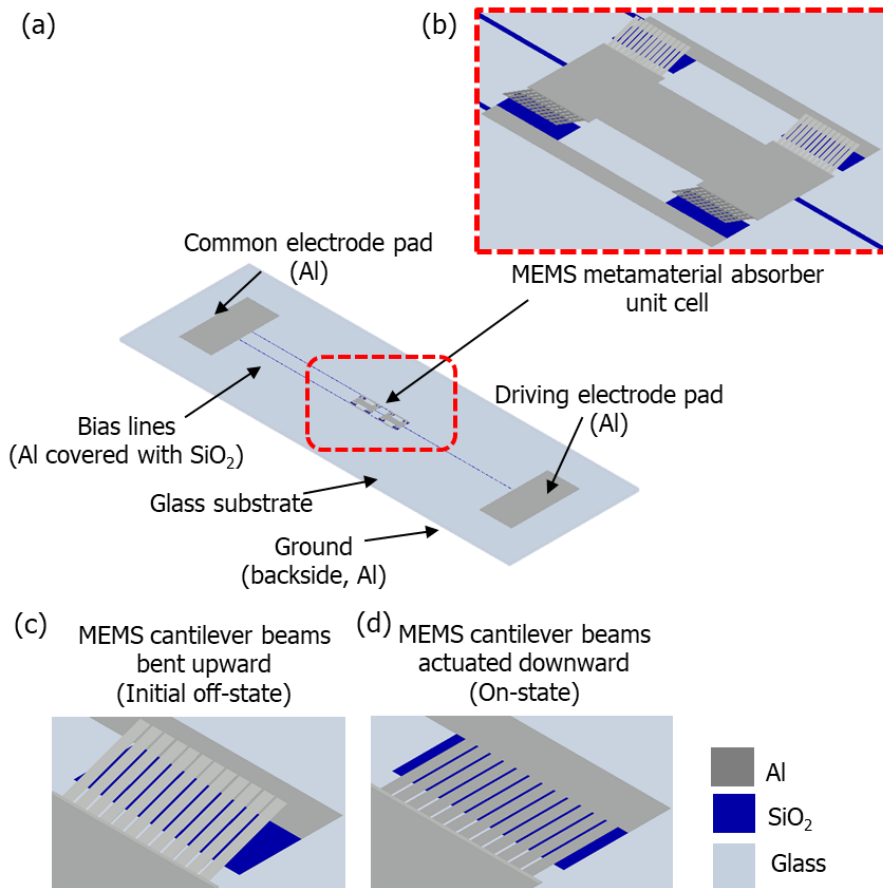
Figure 3.1. Design of the 1st absorber (a) Perspective illustration of the 1st absorber sample (b) Schematic of unit cell (c) Initial state of MEMS cantilever beams bent upward (d) MEMS cantilever beams actuated downward

3.2 Design

Figure 3.2 shows the unit cell schematic and parameters used for designing the 1st absorber. As shown in Figure 3.2 (a), the SRR structure of the unit cell is in a symmetry shape. Also, 12 cantilevers in each bottom electrode site are aligned with 12 μm space. The detailed value of the parameters is described in Table 3.1.
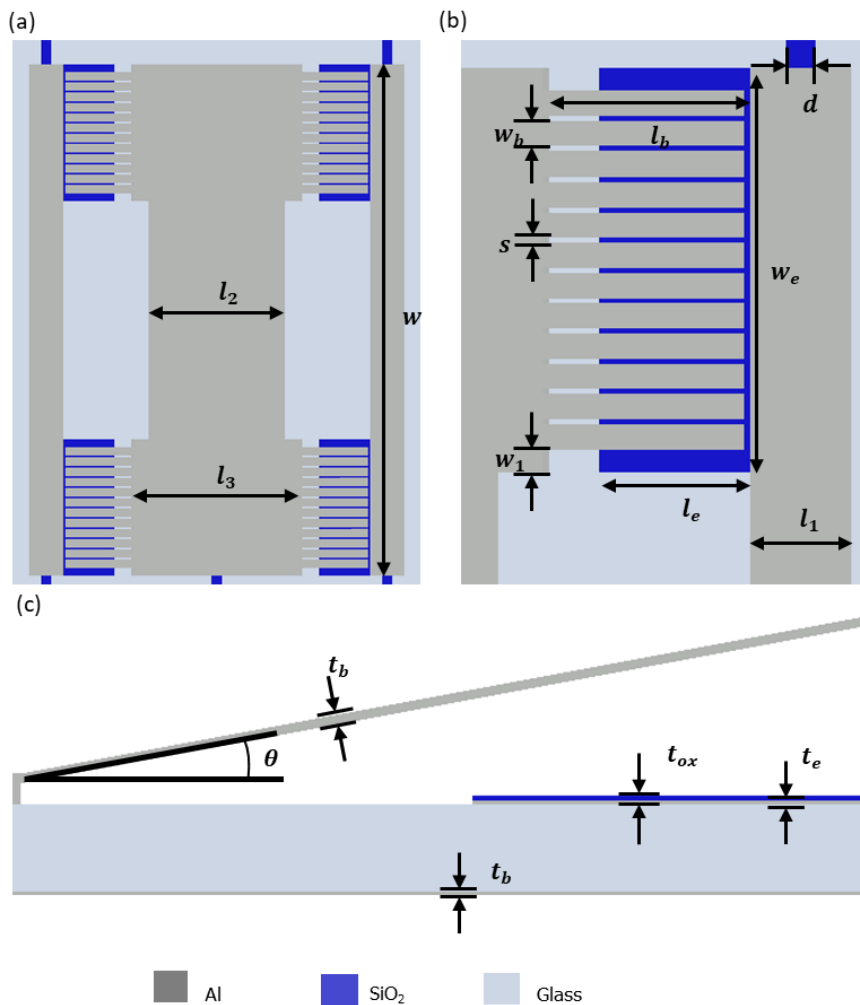
Figure 3.2. Design parameters of the 1st absorber (a) Unit cell parameters (b) Parameters of cantilever array and bottom layer (c) Parameters shown in lateral view

Table 3.1. Dimension of the 1st design

Parameters	Description	Value	Unit
d	The line width of the electrode line	40	μm
l_1	The edge length of the unit cell	200	μm
l_2	The middle length of the anchor	800	μm
l_3	The length of the anchor	1	mm
l_e	The length of the dielectric film	300	μm
w	The width of the SRR unit cell	3	mm
w_e	The width of the dielectric film	800	μm
l_b	The length of the cantilever beam	400	μm
w_b	The width of the cantilever beams	50	μm
s	The space between cantilever beams	10	μm
w_1	The margin of the array edge	45	μm
t_b	The thickness of the cantilever beam	1	μm
g	The gap of the initial sacrificial layer	2.5	μm
t_{ox}	The thickness of the silicon oxide	500	nm
t_e	The thickness of the electrode pad	500	nm
h	The thickness of the glass substrate	500	μm
t_g	The thickness of backside Al	200	nm

3.2.1 Split ring resonator and simulation

Figure 3.3. is the equivalent circuit for the metamaterial absorber because the cantilever functions as variable capacitance. The frequency tunability can be realized by the following equation:

$$f_r = \frac{1}{2\pi\sqrt{LC_{var}}} \qquad \text{Eqn. 3.1}$$

where, f_r is resonant frequency, L and C_{var} are inductance and capacitance of the SRR, respectively.
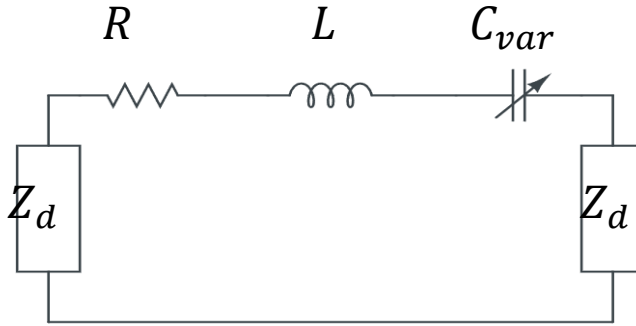
Figure 3.3. The equivalent circuit of metamaterial absorber

In order to design and optimize the electromagnetic (EM) response of the proposed absorber, commercial full-wave EM simulation software (Ansys HFSS) is used. Figure 3.4 shows the electric field distribution of the proposed metamaterials absorber unit cell. The electric field was strongly distributed between the cantilever and aluminum of the SRR. Accordingly, SRR capacitance (C_{var}) can be regulated by a cantilever beam angle.
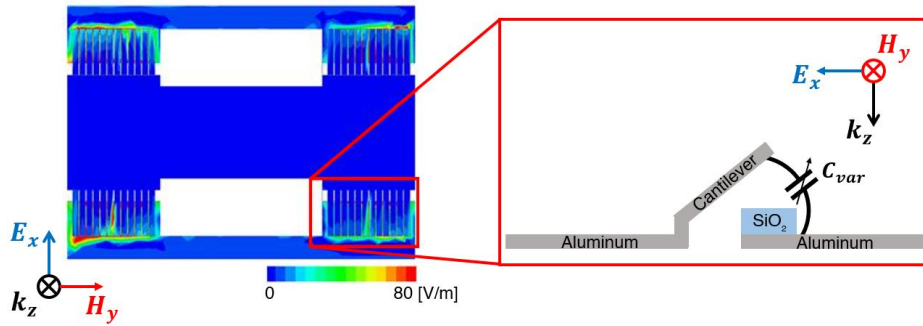
Figure 3.4. Electric field distribution of the proposed metamaterial absorber unit cell.

Initially simulated EM characteristics of the designed absorber are shown in Figure 3.5. For simplicity of the simulation, MEMS cantilever beams are assumed to be flat, linear structures, instead of the upward curved structures that the fabricated MEMS cantilevers beams would really have. Figure 3.5 (a) shows the simulated reflection and transmission coefficient when the cantilever beam has a flat structure. The initial flat cantilever beam structure had -18 dB of reflection coefficient at 26.4 GHz of resonance frequency. Since the bottom plane was totally covered with metallic ground, the transmission coefficient was below -60 dB. Accordingly, the normalized real and imaginary impedance ($\frac{Z_M}{Z_0}$) were 0.78 and 0.12, respectively, as shown in Figure 3.5 (c). As a result, the proposed metamaterials absorber had 98.5% absorptivity at 26.4 GHz as shown in Figure 3.5 (b). To check frequency tunability, the reflection coefficients were simulated according to the cantilever beam angle variation. As expected from Figure 3.5 (d), the absorption frequency was increased from 26.4 GHz to 28.4, 30.2, 32.3 and 33.5 GHz when the cantilever beam angle was increased from 0° to 2°, 4°, 6° and 8°, respectively. Therefore, the frequency tunability was confirmed by numerical simulation according to the cantilever beam angle variation.

62
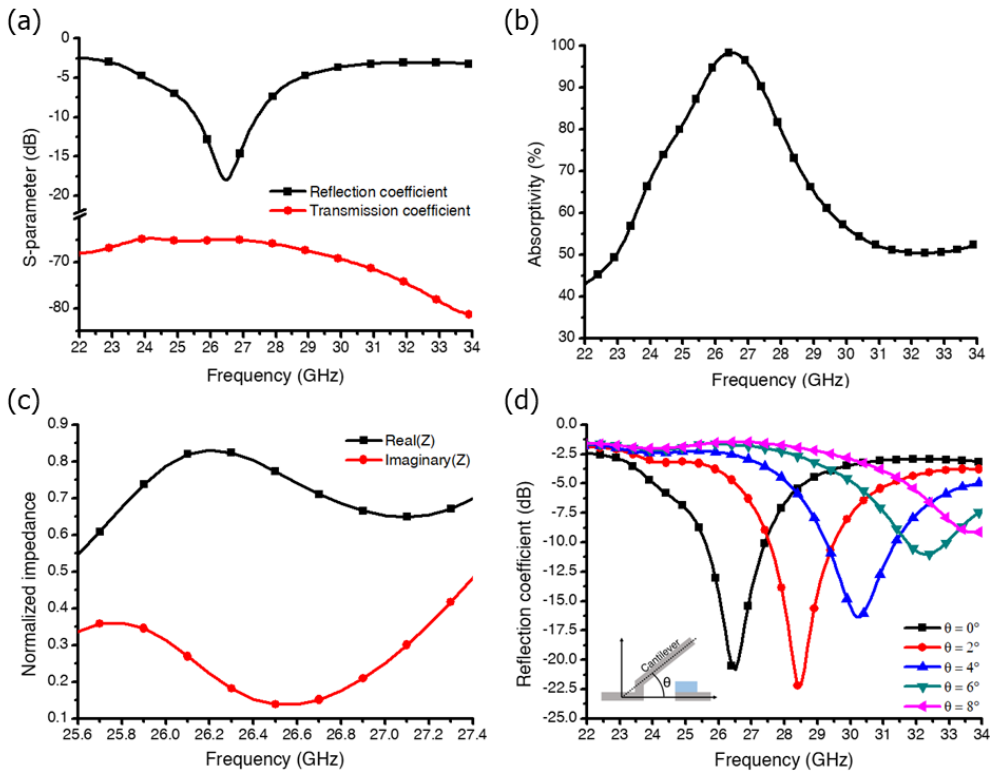
Figure 3.5. Analysis of the electromagnetic characteristics of the proposed metamaterial absorber. (a) Reflection and transmission coefficients when cantilever beam angle is 0° (b) Absorptivity calculated from the simulated *S*-parameter results (c) Normalized impedance from free space impedance of the proposed metamaterial absorber (d) Reflection coefficient results according to the cantilever beam angle variation.

3.2.2 Capacitance of cantilever with stress gradient

Furthermore, the beam height is also correlated with the curvature of the entire beam, and each beam height and curvature is correlated with the C value in the LC resonator, so the beam height affects the resonant frequency of the absorber. In the SRR structure resonator of this study, capacitance is formed between the beams and the bottom electrode.

Assuming that the beam profile is $g(x)$, it can be roughly obtained by the following equation.

$$C_{beam} \cong \int_{x_0}^{x_L} \frac{\varepsilon_r \varepsilon_0 w_b}{g(x)} dx \qquad \text{Eqn. 3.2}$$

where ε_r is the effective permittivity considering the air layer and the oxide layer, w_b is the beam width, and x_L and x_0 are the integral ranges.

Therefore, since the beam height d is roughly $\frac{1}{C}$ and the resonance frequency f is proportional to $\frac{1}{\sqrt{C}}$, the resonance frequency value in the absorber is greatly affected by the height difference between the Al beam and the bottom electrode. That is, the frequency f is roughly proportional to $\sqrt{d}$. Furthermore, if an external force acts and the cantilever beam is deflected and the height difference between the beams is reduced, the frequency shifts and the value drops. In this paper, the height of the cantilever beam was adjusted by electrostatic driving to change the frequency.

- **Numerical approach in simplest form**

For a brief description of the mechanical behavior of the beam with the width (w_b) and the length (L), the simplest way is to start with the capacitance of the curled beam at position x. It is better to set the parameter x by assuming the position of the anchor of the beam as $x = 0$, with the silicon oxide layer and ground to be inclined from $(x = L_0)$ to $(x = L)$ as shown in Figure 3.6
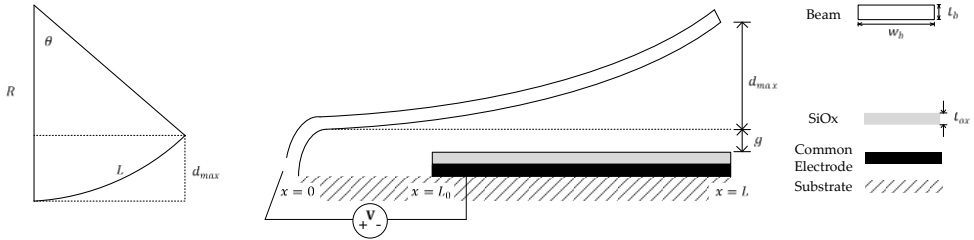
Figure 3.6. Cantilever profile for capacitance calculation

Ignoring the fringing effect, the capacitance of the silicon oxide can be calculated by the relative permittivity of silicon oxide $(\varepsilon_{r,ox})$ and the thickness of the silicon oxide layer (t_{ox}).

$$C_{ox} = \frac{\varepsilon_{r,ox}\varepsilon_0 w_b (L - L_0)}{t_{ox}} \qquad \text{Eqn. 3.3}$$

where ε_0 is the vacuum permittivity.

Additionally, assuming the profile of the cantilever after the ashing process to fit the curvature approximately with radius (R) and arc length (L), it is possible to calculate the air-gap capacitance using the maximum tip end deflection (d_{max}). The radius of curvature can be briefly calculated by solving the following relationship.

$$R\left(1 - \cos\left(\frac{L}{R}\right)\right) = d_{max} \qquad \text{Eqn. 3.4}$$

Thus, the simplest approximation by which to calculate the capacitance of the air gap between the silicon oxide layer and the beam can be written in the following form.

$$C_{air-gap} = \varepsilon_0 w_b \int_{x_0}^{x_L} \frac{1}{g + R\left(1 - \cos\left(\frac{x}{R}\right)\right)} dx \qquad \text{Eqn. 3.5}$$

where g is the initial gap of the sacrificial layer.

Thus, the capacitance between the single cantilever and the ground is the serial summation of the silicon oxide capacitance and the air-gap capacitance.

$$C_i = \frac{C_{ox}C_{air-gap}}{C_{ox} + C_{air-gap}} \qquad \text{Eqn. 3.6}$$

In the reference paper, if the beam has an ideal curvature, the length in the x-direction is L, and the height d at the end of the beam, the pull-in voltage can be roughly calculated as follows.

That is, the tip deflection $\delta(x)$ at position x, with the curvature $q(x)$ caused by a concentrated load can be expressed by Young's modulus (E), the moment of inertia of the beam (I), the width of the beam (w_b), and the length of the beam (L) [147].

$$\delta(x) = \frac{x^2}{6EI}(3L - x)w_b q(x)dx \qquad \text{Eqn. 3.7}$$

Here, $q(x)$ can be modeled by the following expression.:

$$q(x) = \frac{\kappa_{eff}\varepsilon_0}{2}\left(\frac{V}{g + R\left(1 - \cos\left(\frac{x}{R}\right)\right)}\right)^2 \qquad \text{Eqn. 3.8}$$

where κ_{eff} is the effective dielectric constant for the gap and V is the applied

voltage. Here, the effective dielectric for the gap between the beam the common electrode is calculated to be 1.048.

Thus, the tip deflection caused by the applied voltage can be determined known by integrating over the x-axis.

$$\delta(V) = \frac{L w_b \kappa_{eff} \varepsilon_0 V^2}{4EI} \int_{L_0}^{L} \left(\frac{x}{g + R\left(1 - \cos\left(\frac{x}{R}\right)\right)} \right)^2 dx \qquad \text{Eqn. 3.9}$$

3.2.3 Electrostatic driving of cantilever

In the case of an electrostatically driven MEMS cantilever, assuming that the cantilever is an Euler-Bernoulli cantilever, the potential energy of the cantilever is expressed as the sum of electrical potential energy (U_e) and bending strain energy (U_m).

$$U = U_e + U_m \qquad \text{Eqn. 3.10}$$

First of all, if the initial profile of the beam is called $g(x)$ and the reduced deflection function when voltage V is applied is called $w(x)$, in the case of U_e is in following equation [148].

$$U_e = -\int F_e(x) dx = -\int \frac{V^2}{2} \frac{\partial C(x)}{\partial(g(x) - w(x))} = -\int \frac{\varepsilon w_b V^2}{2(g(x) - w(x))} dx \qquad \text{Eqn. 3.11}$$

Moreover, bending strain energy U_m could be written in following form.

$$U_m = \frac{EI}{2} \int \left(\frac{d^2 w}{dx^2} \right) dx \qquad \text{Eqn. 3.12}$$

Where E is Young's modulus, and I is a cross-sectional area moment.

In the same vein, for a general upward curved cantilever beam, assuming that w(x) is a cubic equation with respect to x, w(x)=0 at x = 0 and the beam is not linear, then it is available to assume $w(x)$ to be linear combination of polynomial by

67

Taylor expansion.

$$w(x) = \eta_a x^2 + \eta_b x^3 \qquad\qquad \text{Eqn. 3.13}$$

With this assumption, the beam must satisfy to be in a static equilibrium state.

$$\frac{\partial U}{\partial \eta_a} = \frac{\partial U}{\partial \eta_b} = 0 \qquad\qquad \text{Eqn. 3.14}$$

Here, η_a and η_b are known, and if voltage V is applied, the beam deflection height in static equilibrium can be known.

Furthermore, when η_a and η_b are known, the equilibrium state is converted to a non-equilibrium state under the conditions that pull-in occurs.

$$\frac{\partial^2 U}{\partial \eta_a^2} = \frac{\partial^2 U}{\partial \eta_b^2} = 0 \qquad\qquad \text{Eqn. 3.15}$$

- ■ Analytical approach

The pull-in voltage of a single curled cantilever beam can be simply calculated using an analytic approach. Assuming that the beam has uniform curvature showing the maximum tip end deflection (d_{max}), the pull-in voltage ($V_{\text{pull-in}}$) can be expressed by the Young's modulus of metal (E), the possion ratio of metal (ν), the initial gap (g), and the dimensions of the cantilever beam. The analytic equation for the pull-in voltage is as in the following expression [149].

$$V_{PI} = \left(1 + 1.015\,\frac{d_{max}}{g}\right)\left(\frac{2t_b^3 gE/(1-\nu^2)}{8.37\varepsilon_0 l_b^4\left(\frac{5}{6g^2} + \frac{0.19}{g^{1.25}w_b^{0.75}} + \frac{0.19}{g^{1.25}l_b^{0.75}} + \frac{0.4t_b^{0.5}}{g^{1.5}w_b}\right)}\right)^{\frac{1}{2}} \qquad \text{Eqn. 3.16}$$

However, in the absorber unit cell structure of this paper, the beam and the bottom electrode are not precisely aligned, so a more complex formula must be used to obtain analytically accurate results. Therefore, it is much precise, to use commercial finite element method (FEM) simulation on calculating the pull-in voltage as shown in Figure 3.7.
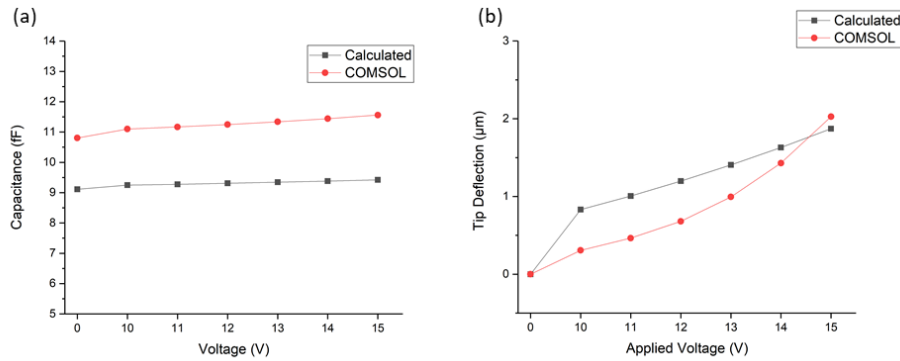
Figure 3.7. Comparison of numerical calculation and FEM simulation on (a) capacitance (b) tip deflection

3.2.4 Stress analysis & PR ashing

The metal film deposited on the sacrificial layer of the steel modifier inevitably has residual stress during the deposition process. Residual stress is expressed as compressive stress or tensile stress due to various conditions such as the thickness or shape of the thin film, the difference in the degree of oxidation of the thin film, the crystallization difference according to process conditions such as pressure or temperature, the difference in the coefficient of thermal expansion between the substrate and the thin film, and impurities on the surface. Therefore, during the sputtering process, a stress is applied on the metal beam by the main causes rooted

by a difference in the coefficient of thermal expansion of the glass substrate and the metal on a polymer-based hardbaked photoresist. This metal beam is additionally subjected to an oxygen plasma ashing process in the form of dry etching. At this point, the -C_xH_y bond of the photoresist-based sacrificial layer under the metal beam is decomposed into carbon monoxide, carbon dioxide, and water vapor by active oxygen, generating a huge amount of heat. As a result, the Al beam receives a thermal stress at the bottom due to the difference in temperature between the upper and lower part of the film. At this time, according to the magnitude of the stress, the metal beam fixed on one side has a specific bending and the height difference is shown at the other end. In particular, ideally, if the stress of the beam has a linear relationship with the thickness and it is assumed that the thickness of the beam is significantly smaller than the width, the height difference (d) and the stress (σ) at the beam end have the following relationship according to the Euler beam theory [146].

$$\frac{\sigma_{top} - \sigma_{bottom}}{t} = \frac{2E}{1 - v^2} \frac{d}{L^2} \qquad \text{Eqn. 3.17}$$

In this case, E is Young's modulus and v is Poisson's ratio.

3.3 Fabrication

3.3.1 Fabrication process

The overall fabrication process for the proposed absorber is illustrated in Figure 3.8. A 4-inch, 525-µm-thick borosilicate glass wafer is used as the substrate for the absorber. The wafer is cleaned in a 4:1 mixture of sulfuric acid (H_2SO_4) and hydrogen peroxide (H_2O_2) to remove contaminants. On the backside of the wafer, a 300-nm-thick aluminum layer is deposited by means of metal sputtering as a ground layer (Figure 3.8 (a)). On the topside, common electrodes for the bias pads, driving electrodes and bias lines are patterned by metal sputtering of a 500-nm-thick aluminum layer and a lift-off process using negative photoresist (DNR-L300, DONGJIN SEMICHEM CO. (Figure 3.8 (b)-(d)). Next, a 500-nm-thick silicon dioxide layer is deposited using plasma enhanced chemical vapor deposition (PECVD) and patterned by reactive ion etching process using carbon tetrafluoride gases to prevent electrical shorting between the MEMS cantilevers and driving electrodes (Figure 3.8 (e)-(g)). After that, a positive photoresist (AZ 4330) is spin-coated at the speed of 5,000 rpm and patterned by a photolithography step as a sacrificial layer. The sacrificial layer is then thermally cured on the hot plate at the temperature of 210°C for 1 hour in order to make it stable to the subsequent processing steps (Figure 3.8 (h)). The final thickness of the sacrificial layer after this thermal treatment is about 2.5 µm. Next, cantilever beam arrays are patterned by aluminum sputtering and a lift-off process using negative photoresist, again the DNR-L300 (Figure 3.8 (i)-(k)). Finally, oxygen plasma ashing of the sacrificial

photoresist layer is used to release the cantilevers without stiction problem (Figure 3.8 (l)). The ashing process is performed under a RF power of 300 W, an oxygen flow rate of 150 sccm and a chamber pressure of 100 Pa as in Section 2.

(a) Backside Al deposition   (b) 1st photolithography   (c) Al sputtering

(d) Metal lift-off   (e) SiOx deposition   (f) 2nd photolithography

(g) SiOx etch   (h) 3rd photolithography & PR thermal curing   (i) 4th photolithography

(j) Al sputtering   (k) Metal lift off   (l) Oxygen plasma ashing
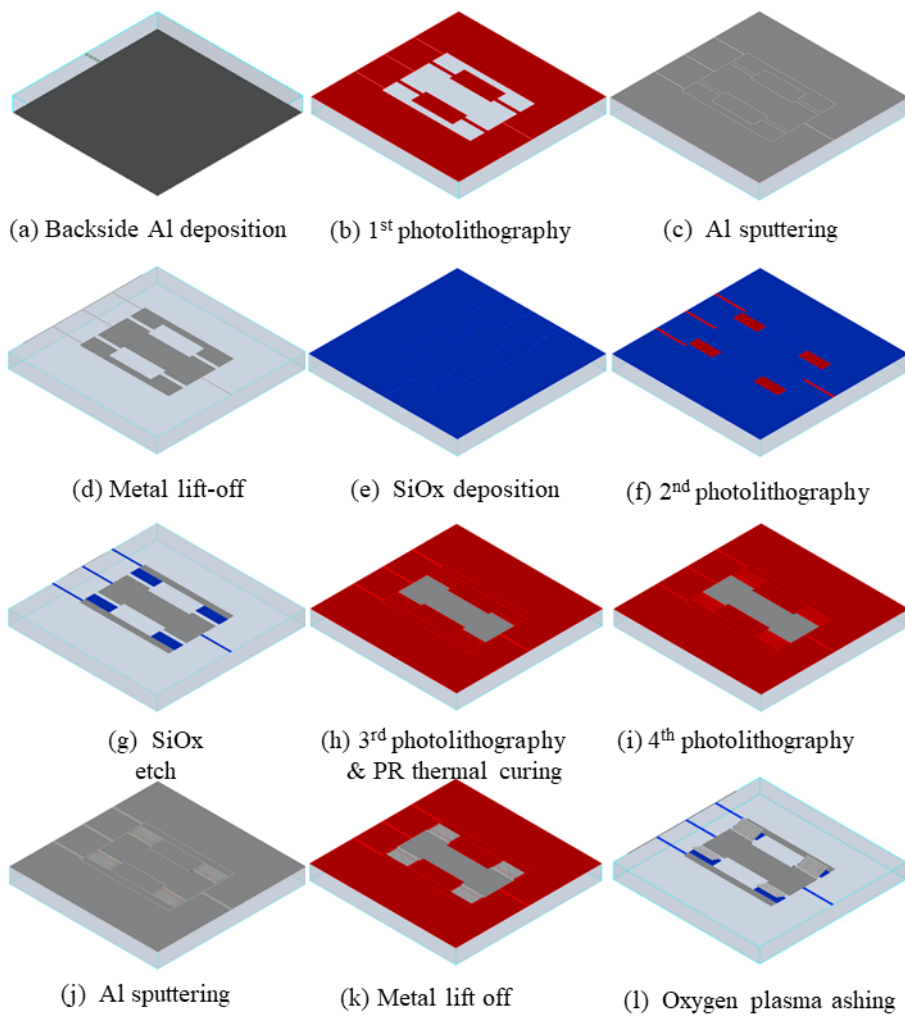
Figure 3.8. Fabrication process flow

Table 3.2. Fabrication process flow - recipe runsheet

Process flow		
[1] 1st photolithography		
Cleaning	Wet station	SPM10 min
QDR	Wet station	DI water 6min, Spin dry
Spin coating	Spin coater	Target: PR 2 μm thickness HMDS 500 rpm×5 sec, 2500 rpm×7 sec DNR-L-300-40 2000 rpm × 40 sec (*negative PR)
Soft bake		90 ℃, 90 sec
Exposure	Aligner 3	TSA, soft contact 200 mJ (25 mW × 8 sec)
PEB		110 ℃, 90 sec
Develop	Wet station	DPD-200 60 sec
QDR	Wet station	DI water 6min, Spin dry
[2] Al deposition		
Al depo.	SRN sputter	Al 5000 Å
[3] Metal lift-off		
Lift-off	Ultrasonic sonicator	Acetone 10min
QDR	Wet station	DI water 6min, Spin dry
[4] SiO2 deposition		
SiO2 depo.	Oxford PECVD	Target 5000 Å recipe: ISRC 3000 Å/min × 100 sec
[5] 2nd photolithography		
Spin coating	Spin coater	Target: PR 2 μm thickness AZ4330 500 rpm×5 sec, 4000 rpm×35 sec
Soft bake	Wet station	110 ℃, 60 sec
Exposure	Aligner 3	TSA (top side alignment), soft contact 400 mJ (20 mW × 20 sec)
Develop	Wet station	AZ 300K 2min 30 sec
Rinsing	Wet station	DI water 6 min
PEB		5 min
[6] SiO2 etch		
SiO2 etch	Dielectric ICP Etcher	Target 5000 Å, recipe: ISRC 3083 Å/min × 1 min 40 sec PR selectivity 1.:1
PR strip	SPM	10 min
[7] 3rd photolithography and thermal curing		
Spin coating	Spin coater	Target: PR 2 μm thick, after AZ4330 500 rpm×5 sec, 4000 rpm×35 sec
Bake		110 ℃, 60 sec
Exposure	Aligner 3	TSA (top side alignment), soft contact 400 mJ (20 mW × 20 sec)
Develop	Wet station	AZ 300K 2min 30 sec
Rinsing	Wet station	DI water 6 min
Sacrificial layer thermal curing		200 ℃ 1hr
[8] 4th photolithography		
Spin coating	Spin coater	Target: PR 2 μm thickness HMDS 500 rpm×5 sec, 2500 rpm×7 sec DNR-L-300-40 2000 rpm × 40 sec (*negative PR)
Soft bake		90 ℃, 90 sec
Exposure	Aligner 3	TSA, soft contact 200 mJ (25 mW × 8 sec)
PEB		110 ℃, 90 sec
Develop	Wet station	DPD-200 60 sec
QDR	Wet station	DI water 6min, Spin dry
[9] Al deposition		
Al depo.	SRN sputter	Al 10000 Å
[10] Metal lift-off		
Lift-off	Ultrasonic sonicator	Acetone 10min
QDR	Wet station	DI water 6min, Spin dry
[11] Al deposition		
Backside Al depo.	SRN sputter	Al 2000 Å
[12] Dicing		
[13] Ashing and beam bending		

Ashing	PR asher 1	10 min + 1day resting + 10 min, 150 sccm, 300 W

3.3.2 Fabrication results

Figure 3.9 (a) shows the photo of the fabricated MEMS tunable metamaterial absorber sample. Only two out of 70 samples survived to verify. However, one sample has failed to measure in the waveguides. Figure 3.9 (b) is the microscope image of the upper cell and the lower cell. In the microscope image, it can be decided whether the cantilever can be released or not. As shown in the figure, cantilevers with stress gradient show dark image due to the diminish of light reflection. Figure 3.9 (c) is the perspective SEM image of the metamaterial unit cell. Moreover, the stress gradient can be verified by SEM image as shown in Figure 3.9(d).
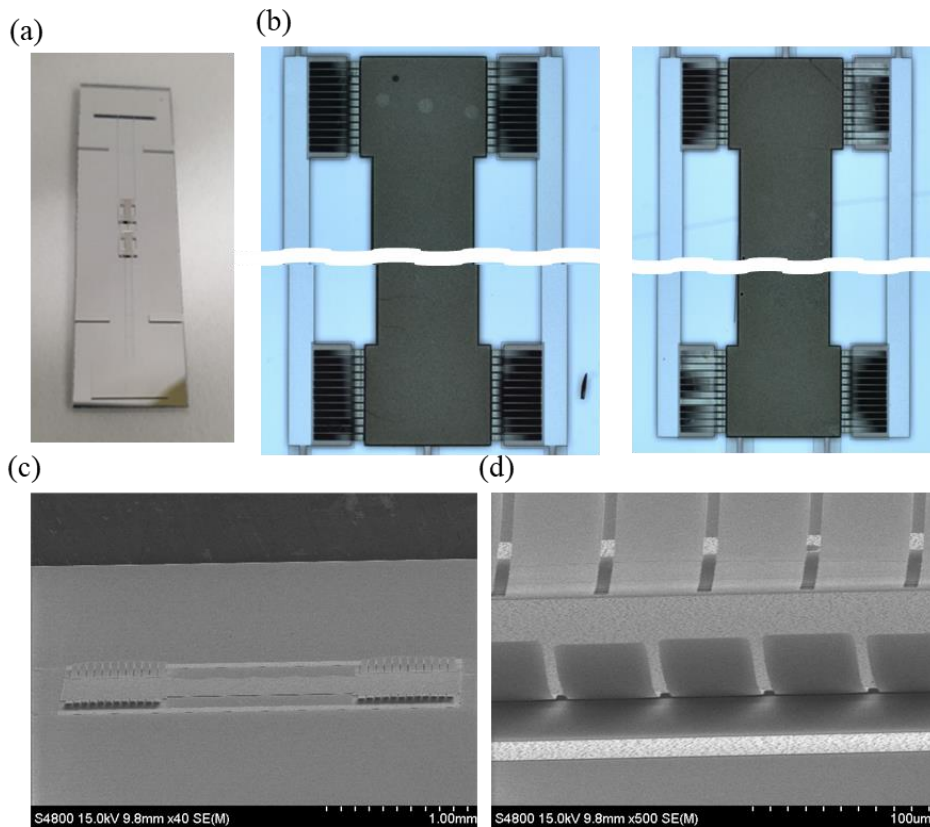
Figure 3.9. Fabrication results of the 1st absorber design (a) Photographs of absorber sample (b) Microscope image of upper and lower unit cell (c) SEM image of metamaterial unit cell (d) SEM images on cantilevers with stress gradient

In two unit cells, the total height profile of 96 beams was actually measured through a 3d surface profiler as shown in Figure 3.10. The mean is 41.52 μm, the standard deviation is 15.4 μm, and the maximum value is 66 μm, and the minimum value is 6.01 μm. The whole distribution is depicted in Figure 3.11.
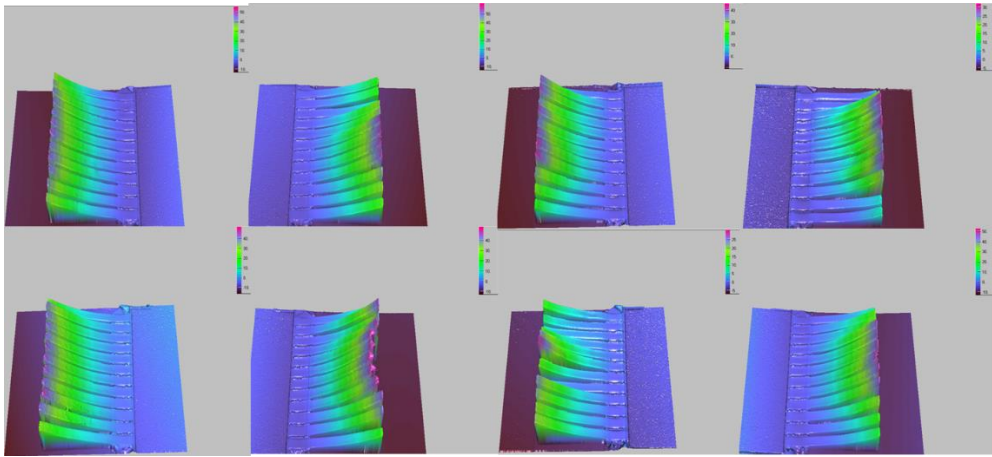
Figure 3.10. 3D surface profiler measurement of cantilever curvature
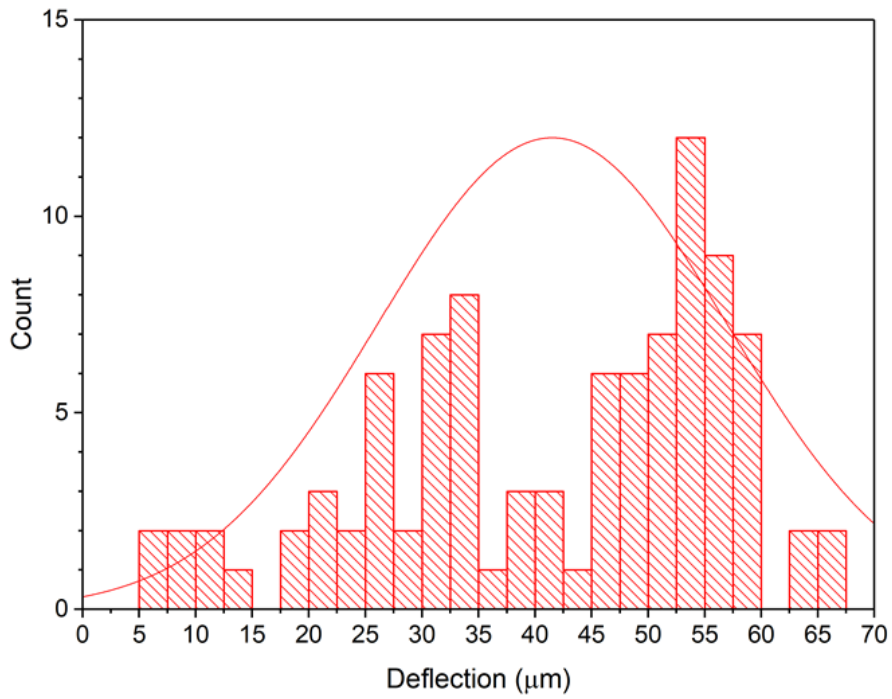
Figure 3.11. Distribution of total 96 cantilevers measured by 3D surface profiler

3.4 Simulation

With commercial FEM simulation tools one for electromagnetic simulation (HFSS ANSYS) and the other for electromechanical simulation (COMSOL Altsoft), the prior linear curve simulation can be slightly modified. The simulation procedure is explained in Figure 3.12. From the measured data in Section 3.3.2 using a 3D surface profiler, the initial geometry of the entire unit cell array can be constructed. With this geometry, the capacitance at 0, 10, 11, 12, 13, 14, and 15 V and deflection profile at 10, 11, 12, 13, 14, and 15 V can be calculated by using the FEM simulation of COMSOL. With this simulated data, the entire geometry of the unit cell array at 10, 11, 12, 13, 14, and 15 V can also be constructed. With this geometry at each step voltage, the electromagnetic full-wave simulation can be conducted using another commercial FEM simulation tool, HFSS.

(a)

(b)

Measured profile (0V)

Simulated profile (10V)
Simulated profile (11V)
Simulated profile (12V)
Simulated profile (13V)
Simulated profile (14V)
Simulated profile (15V)
Flat profile (Pull-in)
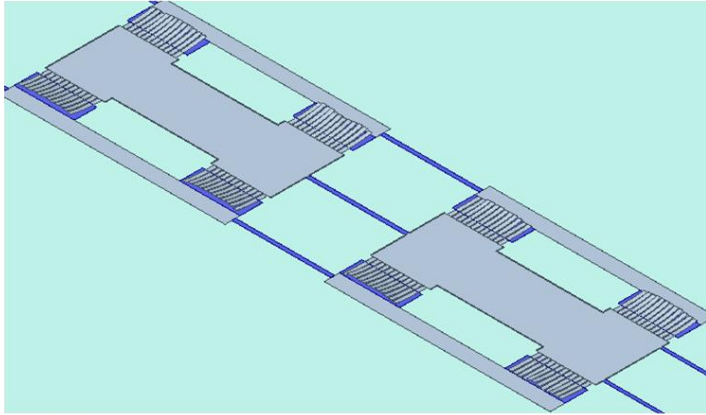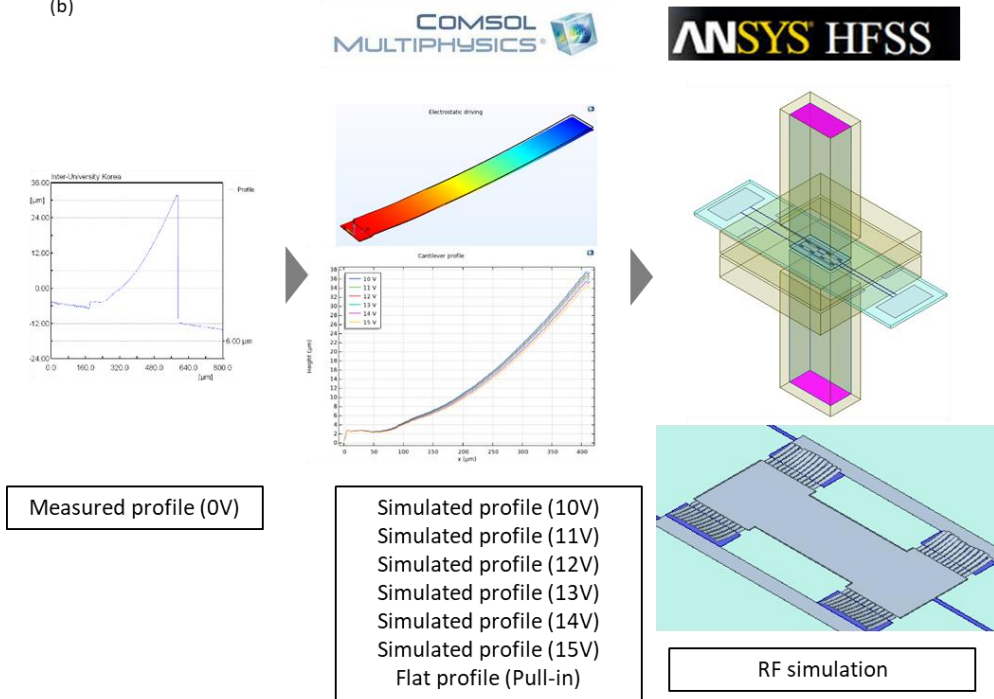
RF simulation

Figure 3.12. Simulation process (a) Geometry construction for simulation from measured profile (b) Simulation steps and process

78
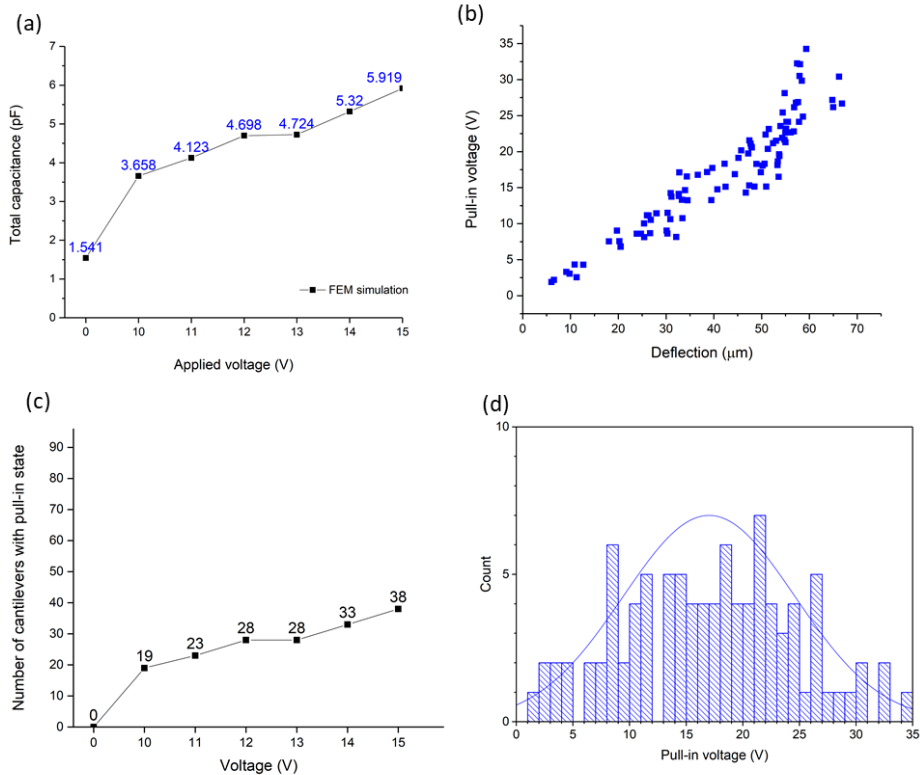
Figure 3.13. Simulation results (a) Total capacitance calculated with FEM tool (b) Plot of pull-in voltage according to deflection (c) Number of cantilevers in pull-in state using FEM simulation (d) Distribution of simulated pull-in voltage

Figure 3.13 (a) is the simulated value of capacitance at each driving voltage. As shown in Figure 3.13 (b), pull-in voltage can be different from each other even though the cantilever has the same deflection. This graph verifies, it is extremely difficult to predict the behavior of the pull-in mechanism. The number of pulled-down cantilever is counted concerning the results from the FEM simulation. As shown in Figure 3.14, the state at 12 and 13 V is similar. In addition, we saw the distribution of pull-in voltage with 96 distributed cantilever profiles as shown in Figure 3.13 (d). As a result of the simulation, the average pull-in voltage was

approximately 17.018 V. However, in the absorber unit cell structure in this paper, it is difficult to accurately define the pull-in voltage of the entire absorber because the cantilever beams are bundled in an array form.

For the electromagnetic analysis, a commercial software HFSS ANSYS ® based on the finite element method is used. From the data of the end-tip deflection measured by the 3D surface profiler, S-parameters of the cantilever array structure at an initial off-state are simulated using HFSS. Here, the dielectric constant of borofloat 33 glass is assumed to be 4.2, and aluminum is assumed as a perfect conductor. Also, from the initial off-state structure, the structural change of the entire cantilever arrays is simulated using COMSOL when 10, 11, 12, 13, 14, and 15 V are sequentially applied. From the simulated structural shape at each voltage, S-parameters are simulated using HFSS. The simulated results are shown in the graph at Figure 3.14.
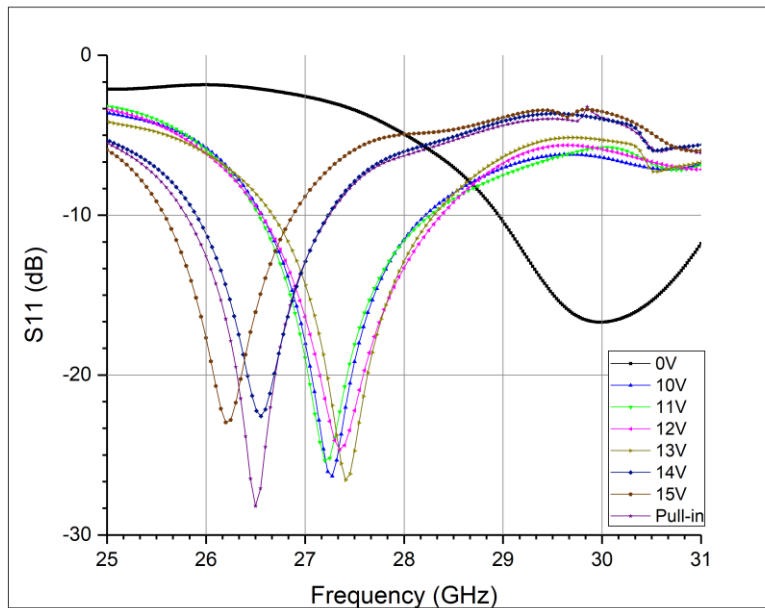
Figure 3.14. Simulated reflection coefficient form the simulated structure

3.5 Experiment

3.5.1 Experiment setup

The *S*-parameters of the fabricated sample were measured by employing an Agilent network analyzer (N5227B, Keysight Technologies Corporation). The measurement setup is shown in Figure 3.15. After the calibration of the network analyzer, the fabricated absorber sample was precisely aligned and embedded between two waveguides (34WCAK_Cu WR-34, A-info Corporation). The form factor of the waveguide is 8.636 mm × 4.318 mm, and the corresponding frequency range is from 22 GHz to 33 GHz. In Figure 3.16, the dimension of the waveguide is well described.
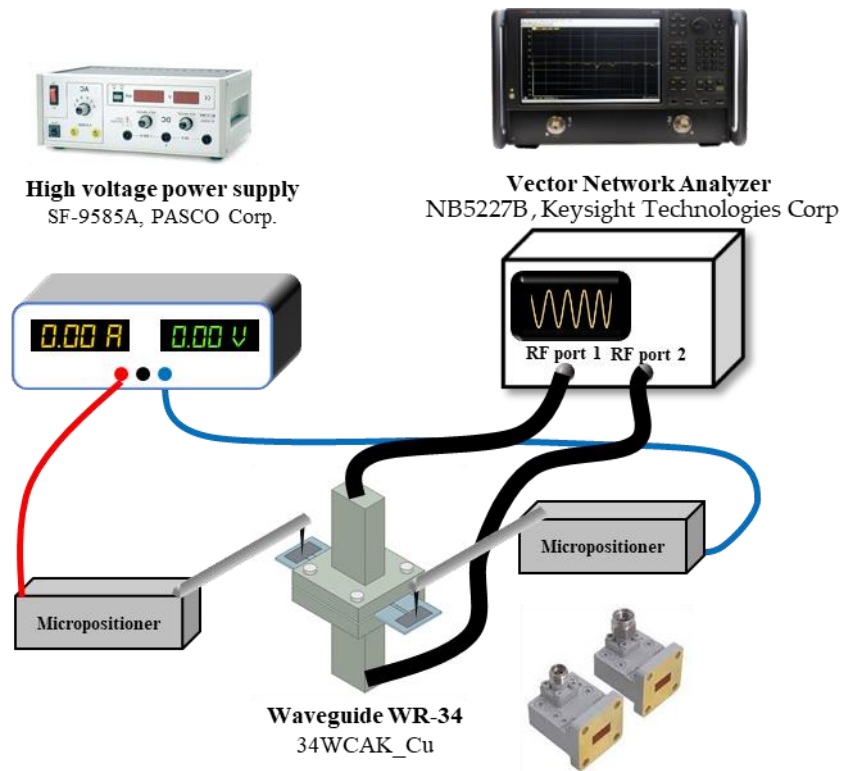
Figure 3.15. Experiment setup (a) Schematic block diagram of the measurement setup, (b) Photograph of the measurement setup; (c) Photograph of the probe tips contacted with the electrodes for biasing the MEMS cantilevers.
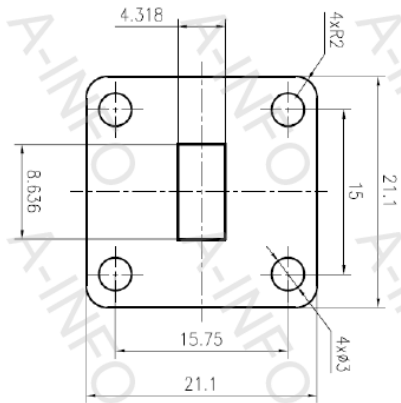
Figure 3.16. Dimension of the waveguide

After the assembly process, the probe tips of the micro-positioner are made to contact with both the driving electrode and the common electrode for applying a driving voltage to reconfigure the cantilever arrays. After connecting the micro-positioner to a power supply, a DC bias voltage is gradually applied to the electrodes of the absorber sample while measuring the reflection coefficient using the network analyzer. Only the reflection coefficient was measured to calculate absorptivity, because the backside of the absorber sample was completely covered with the deposited aluminum layer. The applied bias voltage is swept from 0 V to the pull-in voltage of the MEMS cantilever arrays

3.5.2 Experiment results

It was assumed that the peak of the resonant frequency would suddenly shift at the pull-in voltage. Because the pull-in voltage is the voltage at which the cantilever array undergoes stiction momentarily, the pull-in voltage is assumed to be the voltage when the resonant frequency shows a sudden shift according to the network analyzer. Figure 3.17 (a), (b), and (c) are the results of the reflection coefficient, the transmission coefficient, and absorptivity, respectively, measured while applying voltage from 5 V to 15 V. When 0, 5, 10, 11, 12, 13, 14, 15 V are sequentially applied, the absorption frequencies are 28, 27.9, 27.1, 26.6, 26.2, 26.1, 25.9, and 25.5, respectively. The results are depicted in Table 3.3

Table 3.3. Summary on measurement results

Applied voltage	Resonance frequency	Reflection coefficient	Transmission coefficient	Absorptivity
0 V	28.0 GHz	-5.68 dB	-39.30 dB	72.9 %
5 V	27.9 GHz	-5.70 dB	-43.57 dB	73.0 %
10 V	27.1 GHz	-11.23 dB	-53.74 dB	92.5 %
11 V	26.6 GHz	-14.08 dB	-57.24 dB	96.1 %
12 V	26.2 GHz	-16.40 dB	-61.85 dB	97.7 %
13 V	26.1 GHz	-16.50 dB	-58.90 dB	97.8 %
14 V	25.9 GHz	-16.02dB	-59.49 dB	97.5 %
15 V	25.5 GHz	-33.60dB	-57.33 dB	99.9 %
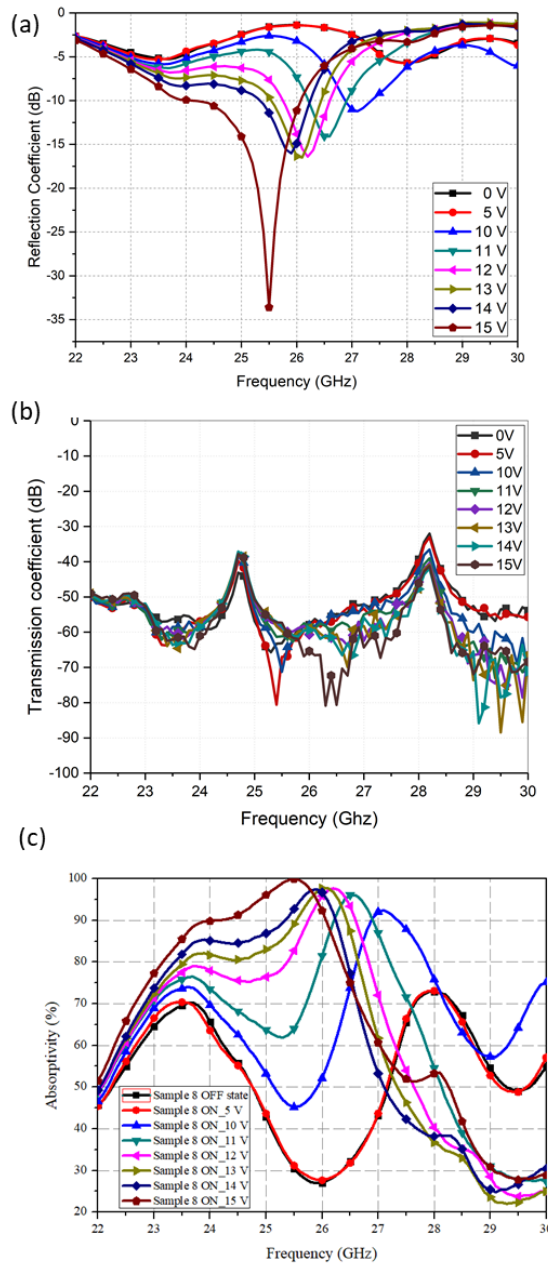
Figure 3.17. Measurement results of the 1st absorber: (a) Reflection coefficient (b) Transmission coefficient and (d) Absorptivity

3.6 Summary

To find out the mechanism of the 1st design MEMS tunable metamaterial absorber with stress-induced cantilever arrays, a vast amount of the simulations is conducted. To figure out explainable logic on the average effect of non-uniform and non-linear pull in movement, simulation is conducted with the real existing cantilever profile (#94 cantilever) that has the most similar value to the average of total of 96 cantilevers as shown in Figure 3.18. Converting non-uniform state to uniform state array, the simulation results show an extremely narrow tuning range, unlike the real measurement. Even more, in the initial state, there is a gap between the simulation and the actual measured value. No matter what method exists, a cause cannot be found. This leads to the conclusion of the study was a failure. What we believed to be analog tuning was actually seeing the digital drive as continuous as the number of cantilevers increased.
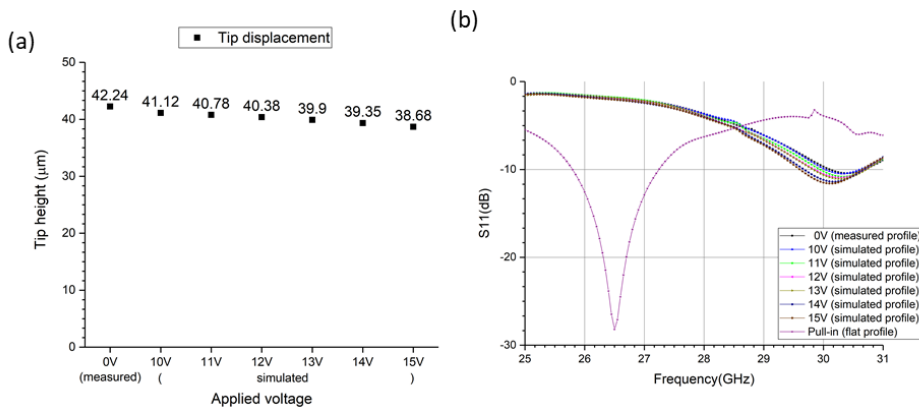
Figure 3.18. (a) Simulation results on deflection of the 1st cantilever out of 96 (b) S-parameters simulation results with virtual structural shape having uniform and nonlinear 96 identical profile

86

CHAPTER 4. The 2nd design of MEMS tunable metamaterial absorber with rectangular shape sub-mm scale stress-induced cantilever with an incremental etch hole spacing for digital driving

4.1 General overview

Figure 4.1 (a) shows the total illustration of the finally evolved MEMS tunable metamaterial absorber. The absorber design is characterized for a waveguide measurement setup which will be discussed later. The absorber sample consists of two SRR unit cells, a silicon oxide layer for electrical isolation, one common electrode, four driving electrodes, bias lines, a borosilicate glass substrate, and a backside metal plane. Aluminum is used for all the SRR unit cells, electrodes, bias lines, and backside metal plane. Each unit cell consists of four stress-induced cantilever beams in total, which are driven as a set, tied in pairs of two left and two right. The inset image of Figure 4.1 (b) shows a schematic view of the unit cells in the absorber. When a pull-in voltage is applied to the electrodes, the cantilever bends downward by electrostatic force and creates a large capacitance change followed by an LC resonance frequency change. Figure 4.1 (c) shows the schematic view of a cantilever beam with upward bending at the initial off state, and Figure 4.1 (d) shows the schematic view of a cantilever beam after applying a pull-in voltage
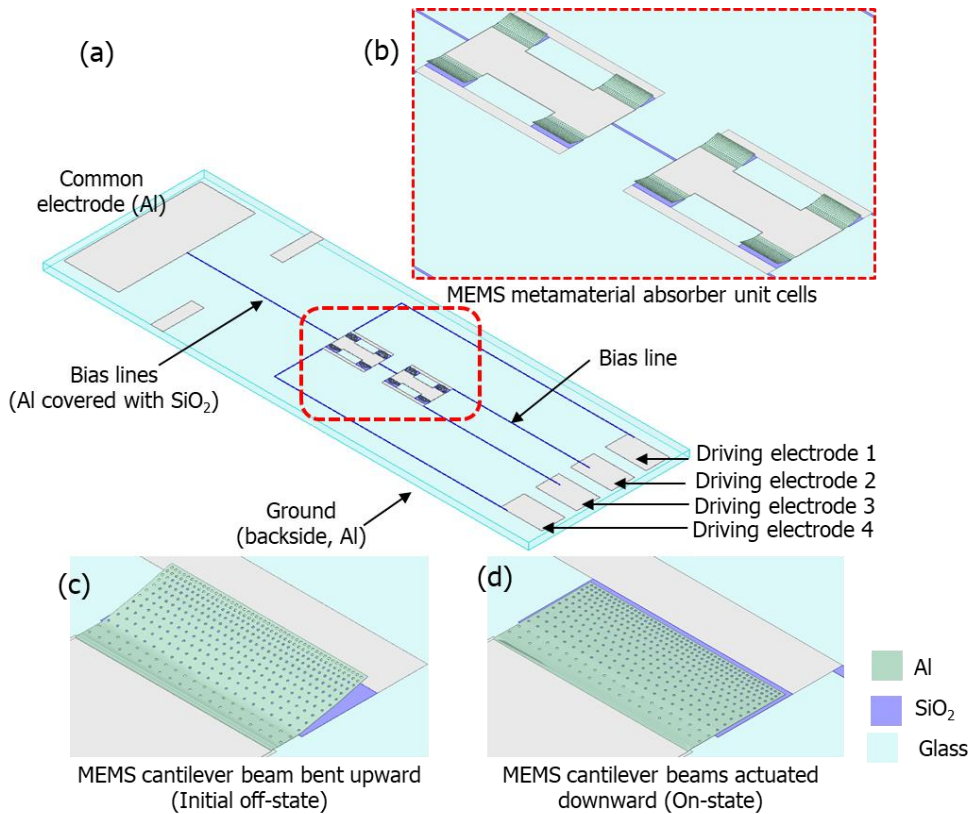
Figure 4.1. Design of the 2nd absorber (a) Schematic of absorber sample (b) Unit cell array (c) Cantilever initially bent upward (d) Cantilever pulled down

As shown in Figure 4.2, driving electrode 1 and 2 are connected to two right side cantilevers of the upper unit cell, and to two right side cantilever of the lower unit cell, respectively. For the left side, the left two cantilever of the lower unit cell are driven by electrode 3, and the left two cantilever of the upper unit cell are driven by electrode 4. After pull-in state, the gap between the cantilever and the common electrode affects the capacitance between those two. Therefore, the increase of capacitance changes the resonance frequency to shift to lower frequency. Here, pull-in voltage will sequentially applied from electrode 1 to electrode 4 making total 5 reconfiguration state as shown in Figure 4.2.
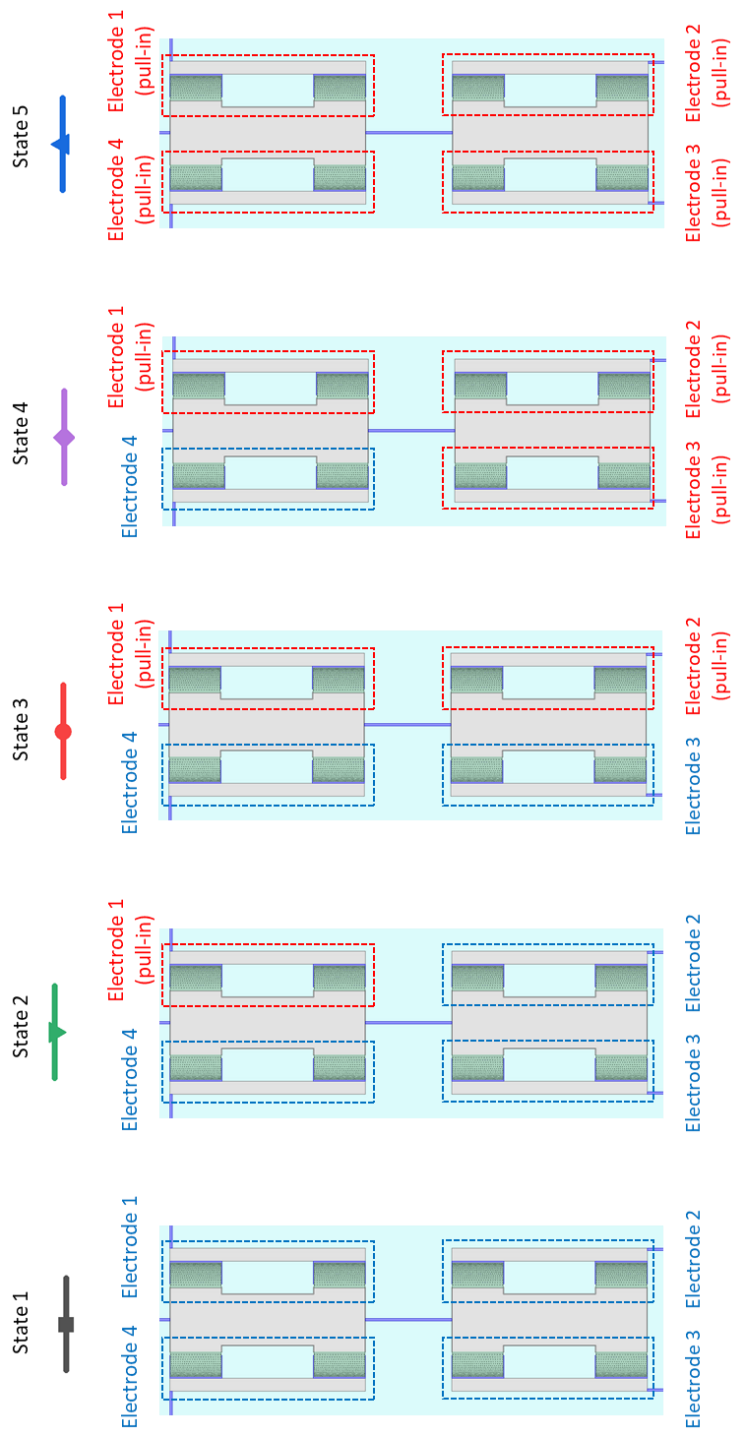
Figure 4.2. Numbering of electrodes and voltage apply sequence according to state

4.2 Design

Figure 4.3 (a) shows the parameters of the metamaterial absorber. Figure 4.3 (b) and (c) describe the bottom driving electrode and the thickness of each layer, respectively. Moreover, Figure 4.3 (d) and (e) show the etch hole distribution in the cantilever, which is the same as Section 2.4. The detailed values of the parameters are described in Table 4.1. and Table 4.2.
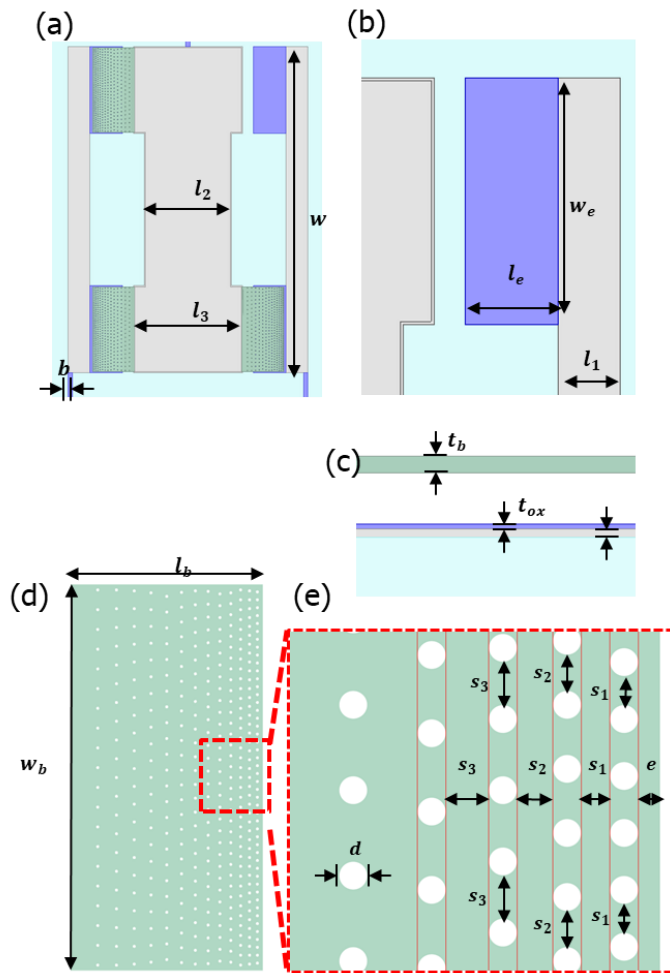
Figure 4.3. Design parameters of the 2nd absorber (a) Unit cell parameters (b) Unit cell parameters of bottom layer (c) Parameters shown in lateral view (d) Design parameters of cantilever beam with semicircle shape (e) Etch hole arrangement

Table 4.1. Dimension of the 2nd absorber

Parameters	Description	Value	Unit
b	The line width of the electrode line	40	μm
l_1	The edge length of the unit cell	200	μm
l_2	The middle length of the anchor	800	μm
l_3	The length of the anchor	1	mm
l_e	The length of the dielectric film	300	μm
w	The width of the SRR unit cell	3	mm
w_e	The width of the dielectric film	800	μm
l_b	The length of the cantilever beam	400	μm
w_b	The width of the cantilever beams	800	μm
t_b	The thickness of the cantilever beam	1	μm
g	The gap of the initial sacrificial layer	2.5	μm
t_{ox}	The thickness of the silicon oxide	300	nm
t_e	The thickness of the electrode pad	500	nm
h	The thickness of the glass substrate	500	μm
t_g	The thickness of backside Al	200	nm

Table 4.2. Parameters of rectangular cantilever

Parameters	Description	Value	Unit
d	The diameter of etch hole	8	μm
e	The length of the edge and 1st column	6	μm
s_1	The space between 1st column and 2nd column, The space between etch holes in 1st column	8	μm
s_2	The space between 2nd column and 3rd column, The space between etch holes in 2nd column	10	μm
s_3	The space between 3rd column and 4th column, The space between etch holes in 3rd column	12	μm
⋮	⋮	⋮	⋮
s_{12}	The space between 12th column and 13th column, The space between etch holes in 12th column	28	μm
s_{13}	The space between etch holes in 12th column	30	μm

4.3 Fabrication

The overall fabrication process before the last step release is the same as Section 3.3. Therefore, the overall process is described in Section 3.3.1. Likewise, the ashing condition is the same as in Section 2.5.

Finally, as described in Section 2, the MEMS cantilever is released with a cyclic plasma ashing process. However, because the driving voltage is patterned below the cantilever to function as a capacitor, the etching rate of the sacrificial layer is faster in the actual sample than in the sample fabricated in Section 2. The backside aluminum ground plane also affects heat generation and increases the etching rate. Therefore, the 5 min step time is sustained until 5 cycles, and then, a shorter step time is applied to slow down the etching rate. The resting time between cycles is over at least 15 min. For the absorber, the additional step time is set to 1 or 2 min.

Figure 4.4 (a) is the fabrication result of the absorber sample. The perspective view of the absorber unit cell array is shown in Figure 4.4 (b). Further magnified vie of stress-induced cantilever with incremental etch hole spacing from the open end of the cantilever is shown in Figure 4.4 (c). For a clear investigation of the cantilever profile, an SEM image is captured as shown in Figure 4.4 (d). The figure mentioned above verifies the developed uniformity of cantilever arrays. However, this cantilever still has nonuniformity at the open end of the cantilever.
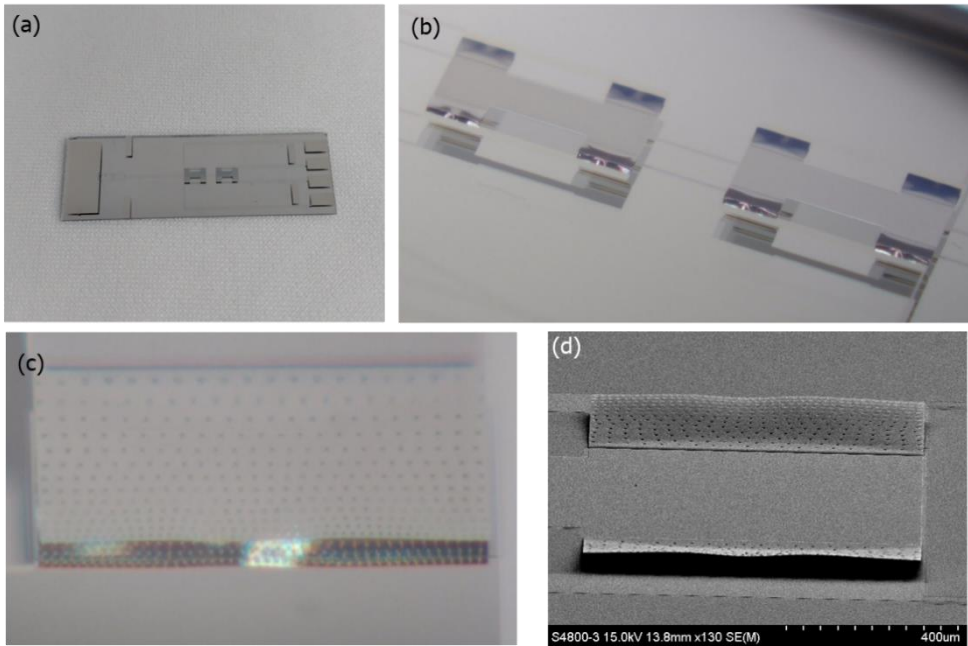
Figure 4.4. Fabrication results of the 2nd absorber (a) Optical image of fabricated MEMS tunable metamaterial absorber sample (b) Unit cell array (c) Lateral view on release semicircle shape cantilever (d) SEM image on the lateral view of semicircle shape cantilever in the unit cell

Figure 4.5 is the microscope image of the upper and lower unit cells. The dark site of the cantilever indicated the degree of releasing. Total 9 samples are fabricated and every cantilever is measured by 3D surface profile. Figure 4.6. is the 3D surface profile of one absorber sample.
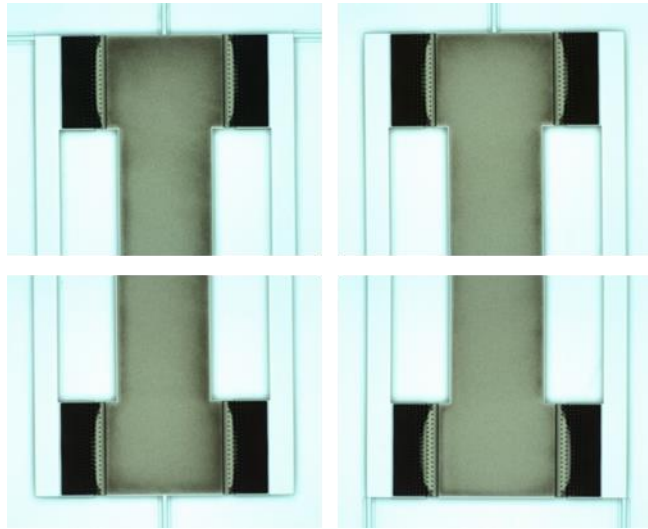
Figure 4.5. Microscope image of fabricated MEMS tunable metamaterial absorber

sample (a) Upper cell (b) Lower cell
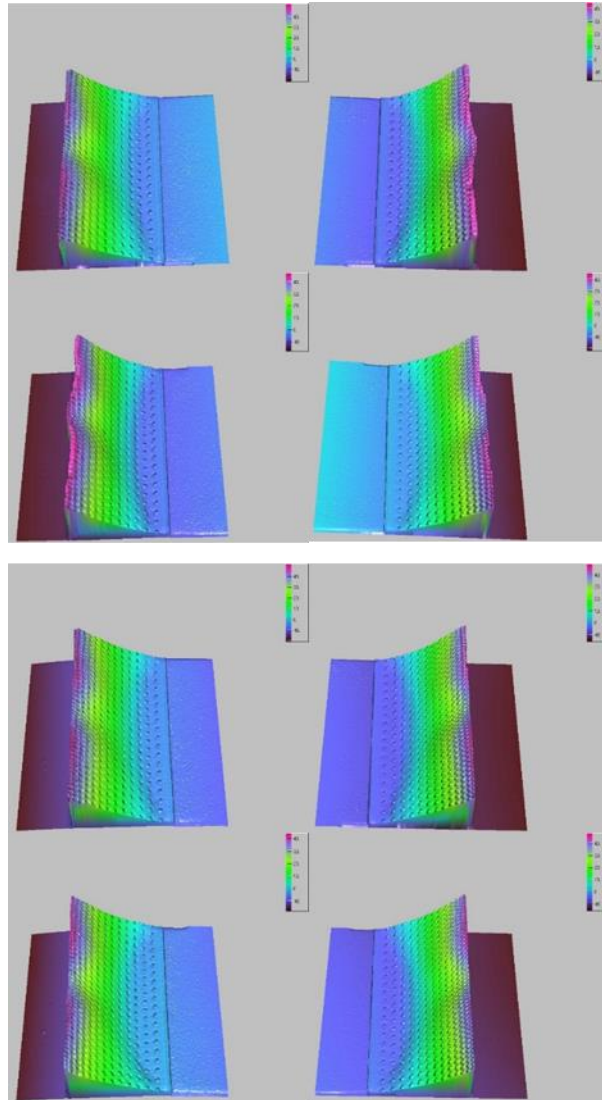
Figure 4.6. Optical 3D surface profile of each cantilever in absorber sample (a) Upper cell (b) Lower cell

Even though it is hard to define the surface profile by one parameter, data of the maximum deflection on the cantilever are written in Table 4.3.

Table 4.3. Data on the maximum deflection of each semicircular cantilever in each fabricated sample

(unit : μm)

Sample	Unit cell (upper)				Unit cell 2 (lower)			
	Left		Right		Left		Right	
#1	52.3	47.5	45.0	46.4	51.7	45.0	49.6	48.9
#2	40.0	46.6	50.0	48.0	50.2	40.2	50.2	49.4
#3	51.2	48.7	47.7	48.6	50.8	46.9	46.2	45.0
#4	49.0	50.3	48.5	53.9	47.9	45.5	54.5	46.5
#5	53.1	51.0	54.6	56.9	52.7	47.6	42.4	52.0
#6	46.0	48.8	37.3	47.5	46.6	46.8	49.6	41.8
#7	44.9	49.7	50.3	51.5	49.2	40.5	54.3	49.7
#8	39.7	45.0	46.2	47.6	44.5	43.7	46.8	46.2
#9	60.5	56.8	48.0	48.3	60.8	62.3	65.8	62.6

4.4 Simulation

The simulation setup and procedure will be later described in Section 5.4. Since it is impossible to copy the schematic of the released cantilever due to the 3D randomness of the surface, the center profile of the rectangular cantilever is exported into an excel data point. With these data, it is assumed that the rectangular has a uniform profile in terms of the later axis. These ideal profile structures are then simulated by a commercial FEM simulation tool.

The simulation results are organized in Table 4.4. The frequency sweep of full-wave simulation results on the reflection coefficient and the absorptivity is shown in Figure 4.7.

Also, electro-mechanical simulation is performed to calculate pull-in voltage. Pull-in voltage is calculated to be in the range of 40 to 50 V, according to the deflection.

Table 4.4. Simulation results of the 2nd design

State	Resonance frequency	Reflection coefficient	Transmission coefficient	Peak absorptivity
State 1	31.09 GHz	-10.30 dB	- 62.94 dB	90.67 %
State 2	30.08 GHz	-19.35 dB	- 63.56 dB	99.84 %
State 3	29.28 GHz	-13.06 dB	- 63.30 dB	95.06 %
State 4	28.49 GHz	-23.80 dB	- 64.53 dB	99.58 %
State 5	27.87 GHz	- 15.79 dB	- 63.52 dB	97.37 %
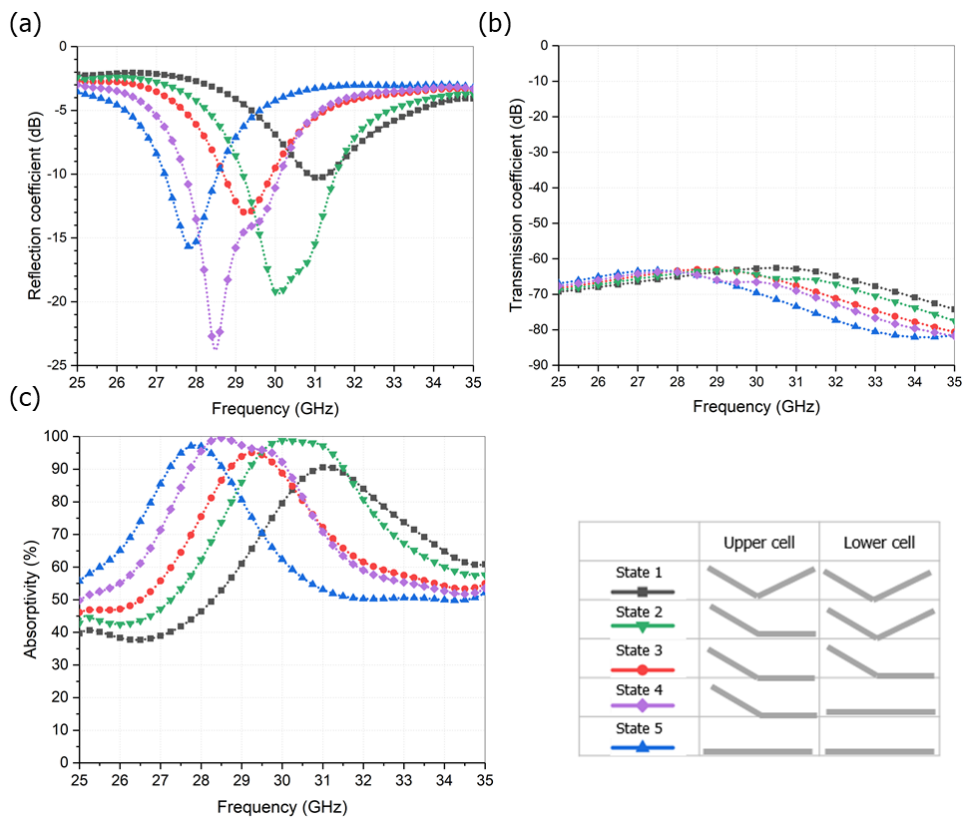
Figure 4.7. Simulation results of the 2nd absorber: (a) Reflection coefficient (b) Transmission coefficient and (d) Absorptivity

4.5 Experiment

The experiment setup and procedure will be later described in Section 5.5. The 8th sample in Table 4.3. is used for measurement. Table 4.5 show the results of the reflection coefficient and absorptivity, respectively, measured while applying 120 V of DC bias on electrode 1 to electrode 4 sequentially. Even though FEM simulation results indicated under 50 V pull-in voltage, the actual rectangular cantilever did not display a sudden shift until 50 V. Sudden frequency shift in network analyzer appears near 100 V.

The resonance frequencies of the 5 different reconfiguration states from the initial off-state to all pulled-down state, are 32.24, 32.11, 31.88, 31.53, and 30.12 GHz, respectively. Figure 4.8. presents the reflection coefficient graphs.

Table 4.5. Measurement results of the 2nd design

State	Resonance frequency	Reflection coefficient	Transmission coefficient	Absorptivity
State 1	32.24 GHz	- 7.85 dB	- 35.74 dB	83.59 %
State 2	32.11 GHz	- 7.13 dB	- 35.13 dB	80.63 %
State 3	31.88 GHz	- 8.33 dB	- 35.53 dB	85.31 %
State 4	31.53 GHz	- 7.91 dB	-34.99 dB	83.81 %
State 5	30.12 GHz	- 10.34 dB	- 35.58 dB	90.75 %
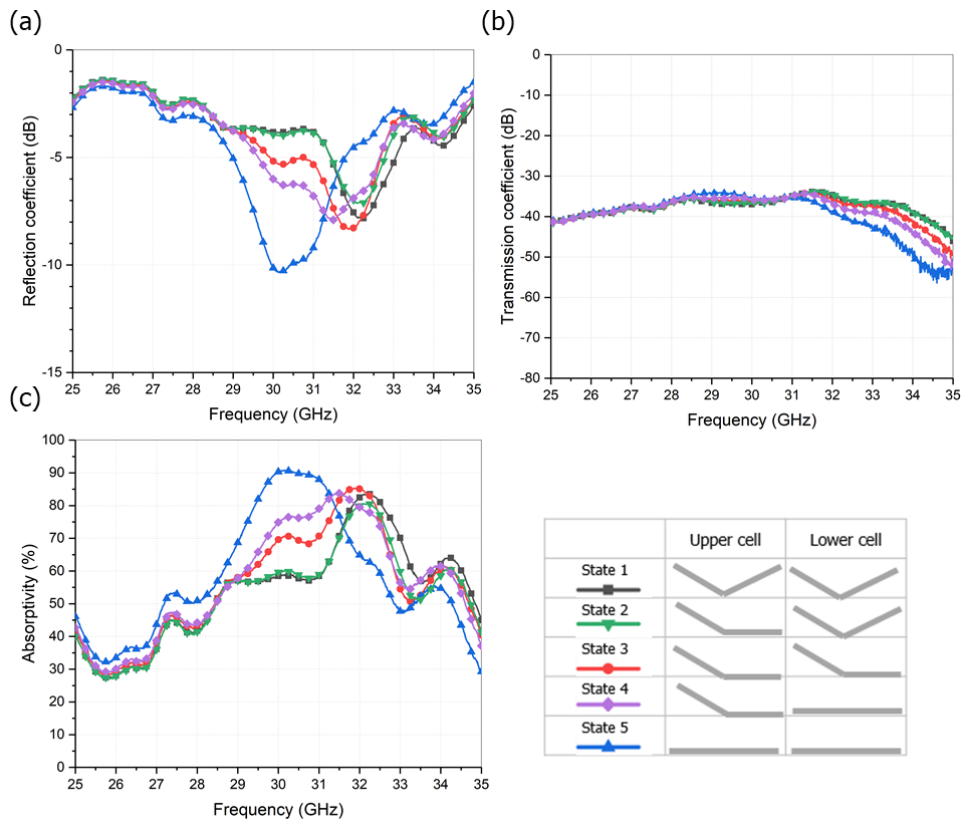
Figure 4.8. Measurement results of the 2nd absorber: (a) Reflection coefficient (b) Transmission coefficient and (d) Absorptivity

4.6 Summary

The 2nd design absorber with rectangular stress-induced cantilever with incremental etch hole spacing clearly shows better and much fabrication results compared to the 1st design absorber with a stress-induced cantilever array. However, the tuning range from the initial off state 1 to all the pulled down state 5 is only Δf=2.12 GHz, and the tuning ratio ($\frac{\Delta f}{f}$) is only 6.6%. In the case of the resonant frequency, the difference between the experimental and simulation results is almost up to 3.04 GHz error. Although the uniformity of the fabrication process result has increased remarkably, the difficulty of mechanical driving operation is considerable and substantial. The cause can be inferred from the simulation of the pull-in voltage and the fact that there is a large gap between it and the actual operation. This driving difficulty seems to be due to the fact that the driving of both vertices of the cantilever beam is not normal. Also, the metal film at the open end of the cantilever will not be straight, so the drive will not be in clear movement.

CHAPTER 5. The 3rd design of MEMS tunable metamaterial absorber with semicircular sub-mm scale stress-induced cantilever with an incremental etch hole spacing for digital driving

5.1 General overview

Figure 5.1 (a) shows the total illustration of the finally evolved MEMS tunable metamaterial absorber. The absorber design is characterized by a waveguide measurement setup which will be discussed later. The absorber sample consists of two SRR unit cells, a silicon oxide layer for electrical isolation, one common electrode, four driving electrodes, bias lines, a borosilicate glass substrate, and a backside metal plane. Aluminum is used for all the SRR unit cells, electrodes, bias lines, and backside metal plane. Each unit cell consists of four stress-induced cantilever beams in total, which are driven as a set, tied in pairs of two left and two right. The inset image of Figure 5.1 (b) shows a schematic view of the unit cells in the absorber. When a pull-in voltage is applied to the electrodes, the cantilever bends downward by electrostatic force and creates a large capacitance change followed by an LC resonance frequency change. Figure 5.1 (c) shows the schematic view of a cantilever beam with upward bending at the initial off state, and Figure 5.1 (d) shows

the schematic view of a cantilever beam after applying a pull-in voltage.
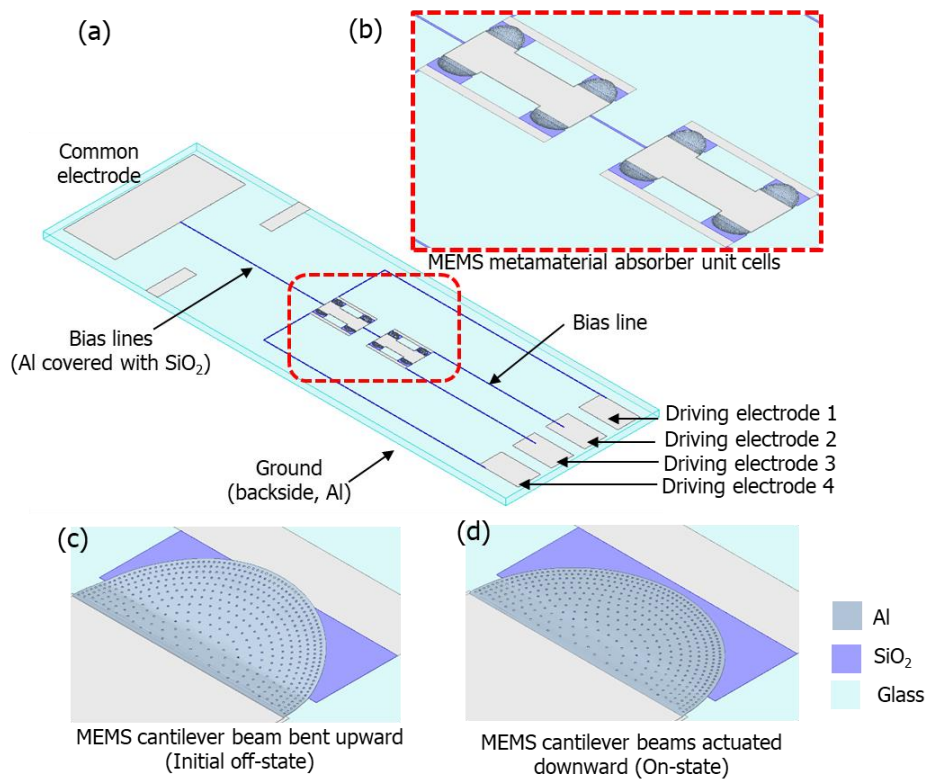
Figure 5.1. Design of the 3rd absorber (a) Schematic of absorber sample (b) Unit cell array (c) Cantilever initially bent upward (d) Cantilever pulled down

As shown in Figure 5.2, driving electrode 1 is connected to two right side semicircular cantilevers of the upper unit cell, and driving electrode 2 is connected to two right side semicircular cantilevers of the lower unit cell. For the left side, the left two semicircular cantilevers of the lower unit cell are driven by electrode 3. Finally, driving electrode 4 controls the two left semicircular cantilevers of the upper unit cell. Therefore, if the high voltage over pull-in voltage is applied to one of the electrodes, the cantilever undergoes a pull-in state. Then, the gap between the cantilever and the common electrode affects the capacitance between those two. Therefore, the increase of capacitance changes the resonance frequency to shift to a lower frequency.

In this research, as shown in Figure 5.2, the high voltage over pull-in voltage will be sequentially applied from electrode 1 to electrode 4. Each electrode has only two states, initially bent upward off-state and pulled down on the state. However, in this thesis, the absorber is designed to have 5 different reconfiguration states. Thus, at each reconfiguration state, the resonant frequency will be measured with S-parameters with a network analyzer that would be explained later.
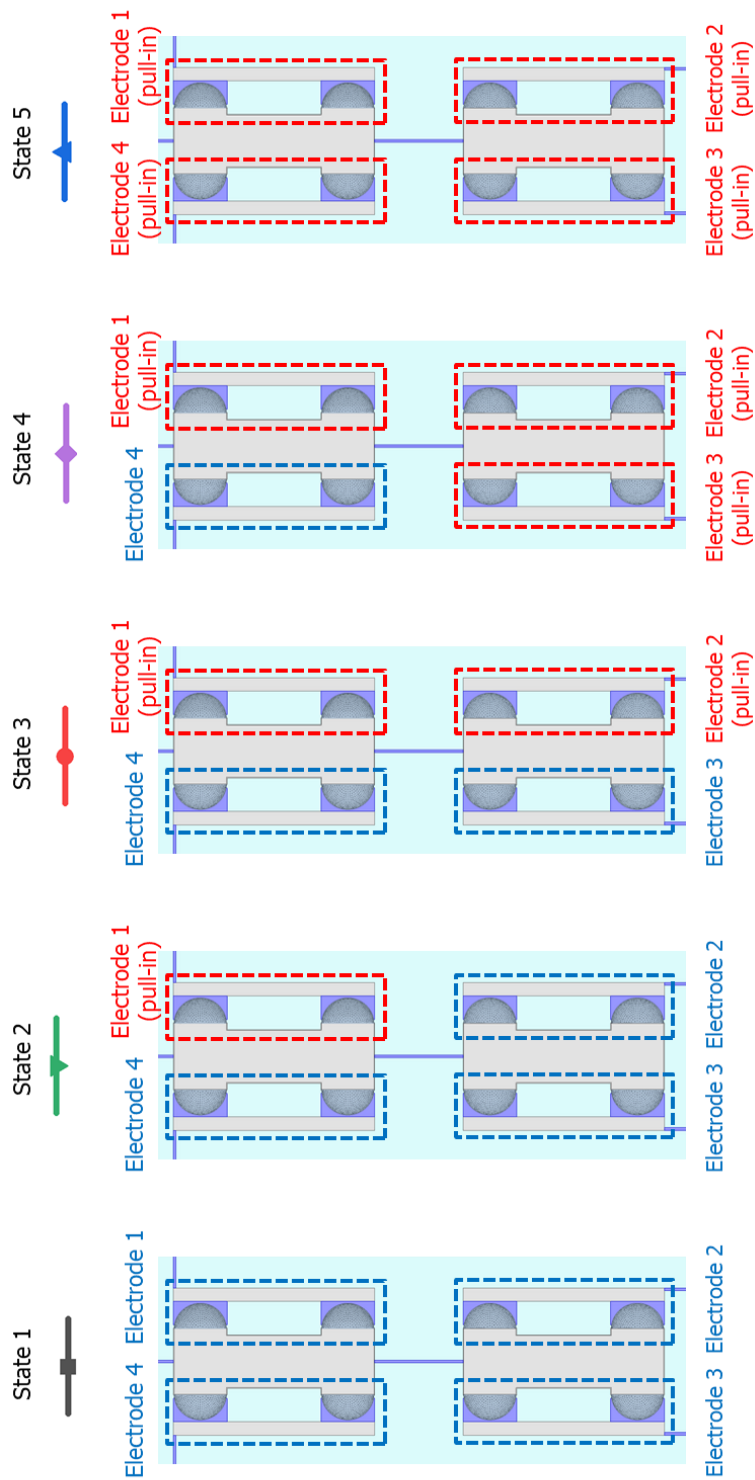
Figure 5.2. Numbering of electrodes and voltage apply sequence according to state

5.2 Design

5.2.1 Electromagnetic properties

Figure 5.3 (a) shows the electric field distribution of the proposed MEMS tunable metamaterial absorber unit cell in the TE mode. The electric field is strongly formed between the cantilever and the driving electrode. Parametric studies by full-wave FEM simulation using commercial software (ANSYS HFSS) are performed to design and optimize the electromagnetic response of the proposed metamaterial absorber. First, a simulation of the electromagnetic characteristics of the designed absorbers is conducted when all the cantilevers are pulled down in the unit cells. For the simulation, MEMS cantilever beams are assumed to have a flat profile with no etch hole. Figure 5.3 (b) is the reflection coefficient and transmission coefficient from the simulation results. For all cantilevers pulled down, the reflection coefficient is calculated to be -15.15 dB at 28.48 GHz of the resonance frequency. The transmission coefficient is calculated to be -63.52 dB because the backside plane of the absorber is deposited with the metallic ground. Additionally, the simulation results for the normalized impedance of the real and imaginary parts are 0.65 and 0.23 shown in Figure 5. 3 (c).
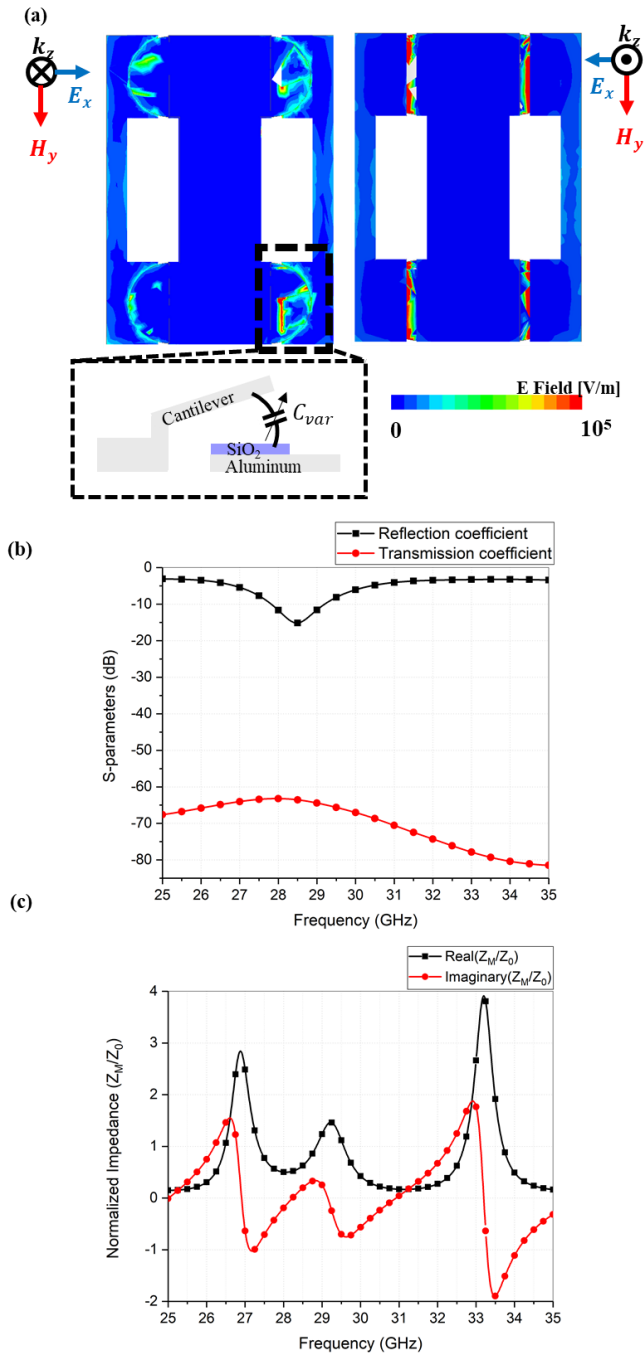
Figure 5.3. (a) Electric field distribution in the proposed MEMS tunable metamaterial absorber unit cell (b) Simulated *S*-parameters when all cantilevers are pulled down (c) Real and imaginary parts of the normalized impedance ($\frac{Z_M}{Z_0}$)

5.2.2 Design parameter

Figure 5.4 (a) shows the parameters of the metamaterial absorber unit cell. Also, the dimension of the bottom metal layer under semicircular shape stress-induced cantilever is described in Figure 5.4 (b). Moreover, the thickness dimension of a substrate, backside ground metal film, bottom metal film layer, silicon oxide thickness, and beam thickness is depicted in Figure 5.4 (c). Figure 5.4 (d) and (e) are the same form factor from Section 2.5.
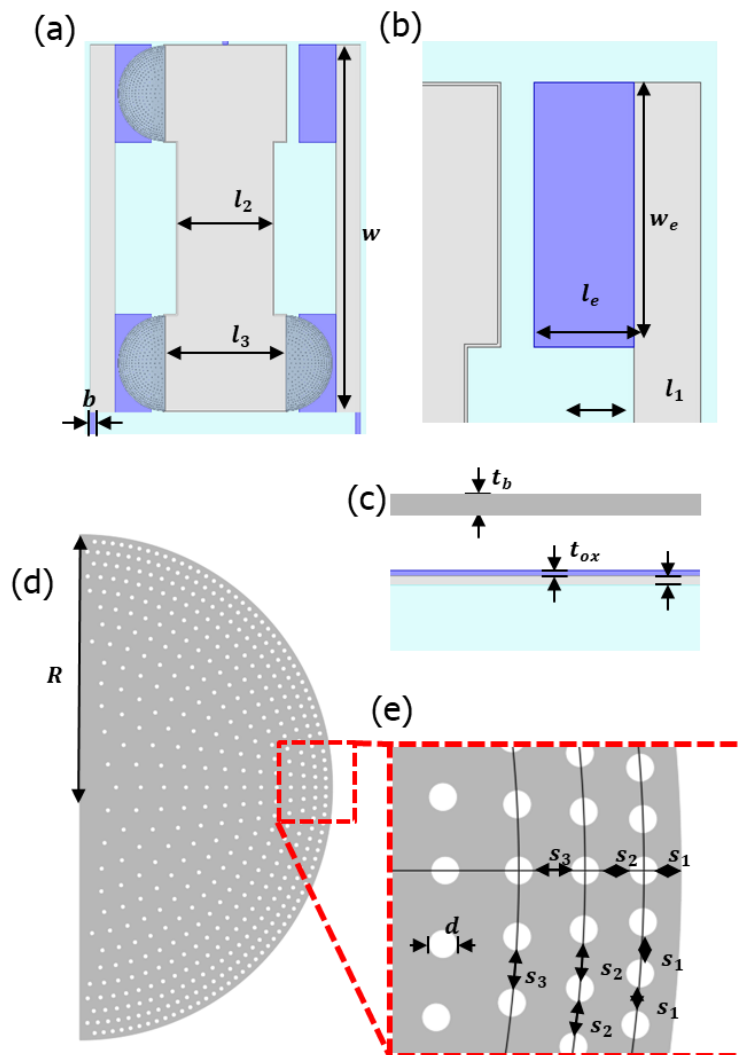
Figure 5.4. Design parameters of the 3rd design (a) Unit cell parameters (b) Unit cell parameters of bottom layer (c) Parameters shown in lateral view (d) Design parameters of cantilever beam with semicircle shape (e) Etch hole arrangement

The detailed values of the parameters are described in Table 5.1. and Table 5.2. The same values in Section 2 are used for the parameters of the etch hole and space in the stress-induced MEMS cantilever

Again, the etch hole spacing described in Table 5.2 increases linearly to achieve uniformity of cantilever profile after oxygen plasma ashing. By arranging to etch holes more densely the near the edge of the cantilever, cantilevers have a gradual deflection from the outside

Table 5.1. Dimension of the 3rd design absorber

Parameters	Description	Value	Unit
b	The line width of the electrode line	40	μm
l_1	The edge length of the unit cell	200	μm
l_2	The middle length of the anchor	800	μm
l_3	The length of the anchor	1	mm
l_e	The length of the dielectric film	300	μm
w	The width of the SRR unit cell	3	mm
w_e	The width of the dielectric film	800	μm
R	The radius of the cantilever beam	390	μm
t_b	The thickness of the cantilever beam	1	μm
g	The gap of the initial sacrificial layer	3.4	μm
t_{ox}	The thickness of the silicon oxide	300	nm
t_e	The thickness of the electrode pad	500	nm
h	The thickness of the glass substrate	500	μm
t_g	The thickness of backside Al	300	nm

Table 5.2. Parameters of semicircular cantilever

Parameters	Description	Value	Unit
d	The diameter of etch hole	8	μm
s_1	The space between edge and 1st radius, The space between holes in 1st radius	6	μm
s_2	The space between 1st radius and 2nd radius, The space between holes in 2nd radius	8	μm
s_3	The space between 2nd radius and 3rd radius, The space between holes in 3rd radius	10	μm
⋮	⋮	⋮	⋮
s_{12}	The space between 11th radius and 12th radius, The space between holes in 12th radius	28	μm
s_{13}	The space between 12th radius and 13th radius, The space between holes in 13th radius	30	μm

5.3 Fabrication

The overall fabrication process before the last step releasing is the same as Section 3.3. Therefore, the overall process is described in Section 3.3.1. Likewise, the ashing condition is the same as in Section 2.5.

Finally, as described in Section 2, the MEMS cantilever is released with a cyclic plasma ashing process. However, because the driving voltage is patterned below the cantilever to function as a capacitor, the etching rate of the sacrificial layer is faster in the actual sample than in the sample fabricated in Section 2. The backside aluminum ground plane also affects heat generation and increases the etching rate. Therefore, the 5 min step time is sustained until 4 cycles, and then, a shorter step time is applied to slow down the etching rate. The resting time between cycles is over at least 15 min. For the absorber, the additional step time is set to 2 min.

The key strategy to release semicircular cantilever with stress-gradient is to measure the cantilever aspect at each cycle and sufficient cooling of both sample and the plasma chamber. This look-up fabrication process is the key strategy to achieving end-tip deflection uniformity.

In total, 18 absorber samples are fabricated. The fabricated absorber samples are individually released. A total of 144 sub-mm scale MEMS cantilever beams with a stress gradient from 18 absorber samples are released and measured by a 3D surface profiler.

The fabrication results are described in Figure 5.5. Figure 5.5 (a) is the optical image of the fabricated sample size of 35.45 mm × 11.75 mm. Figure 5.5 (b)

is the perspective view of two metamaterial unit cells aligned in the middle of the absorber sample 4.318 mm apart from each other. The uniform release of stress-induced cantilever beams can be verified. Unlike rectangular shape cantilever, semicircular has maximum deflection at the perpendicular point from the semicircle center. The results from Figure 5.5 (c) verify the release shape and profile of the sub-mm scale semicircular cantilever with stress gradient. Figure 5.5 (d) is the later SEM image of a semicircular cantilever.
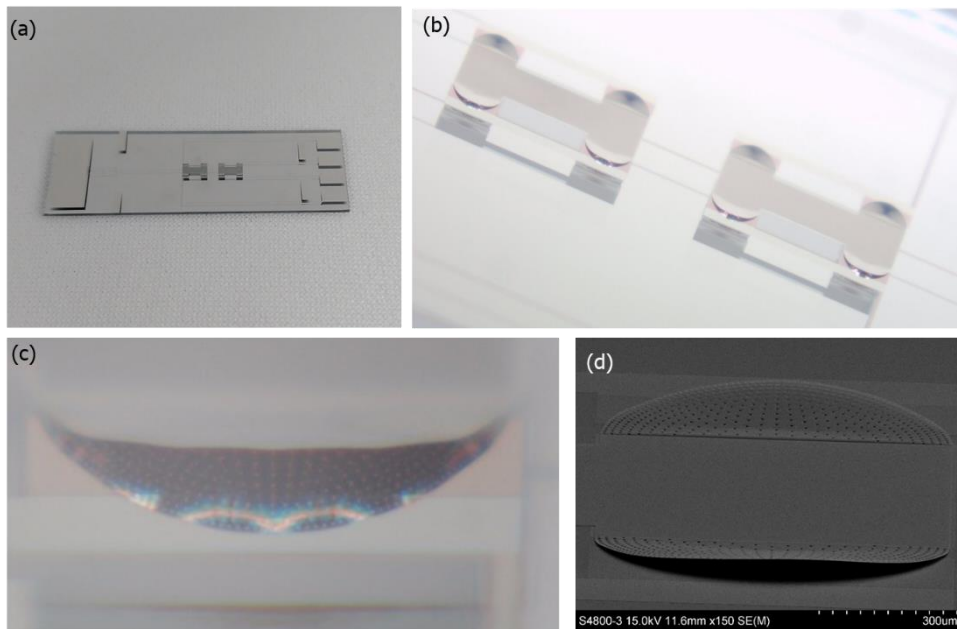
Figure 5.5. (a) Optical image of fabricated MEMS tunable metamaterial absorber sample (b) Unit cell array (c) Lateral view on release semicircle shape cantilever (d) SEM image on lateral view of semicircle shape cantilever in unit cell

Figure 5.6 (a) shows the glowing image under strong light intensity. At the maximum deflection point, the light reflects from the aluminum film showing dazzling images. Figure 5.6 (b) is the perspective view of the MEMS tunable metamaterial absorber unit cell. During releasing, cantilever deflection can be easily confirmed by a general microscope as shown in Figure 5.6 (c). The dark site kept growing after every cycle of the ashing process.
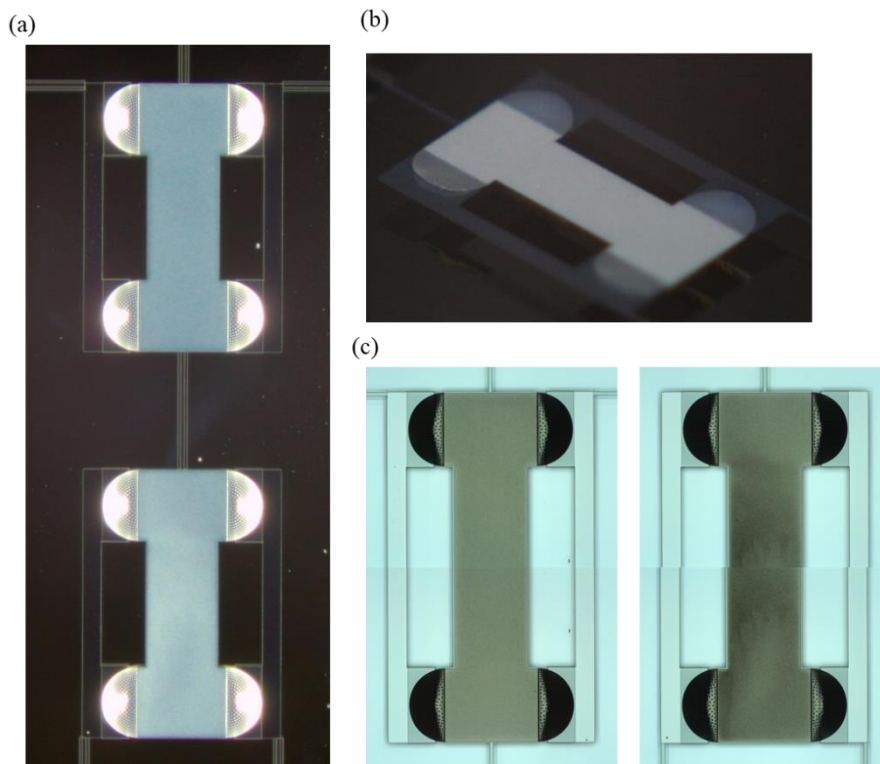
Figure 5.6. (a) Microscope image of fabricated unit cell array glowing light reflection (b) Perspective view on unit cell microscope image (c) Microscope image on each unit cell with semicircle shape cantilever bent upward

Every 144 cantilevers in 18 absorbers are three-dimensionally measured by a 3D surface profiler (Nanofocus), Figure 5.7. is a 3D surface profile image of one of the 18 samples. Even though it is hard to define the surface profile by one parameter, the semicircular cantilever shows only one maximum deflection point near the center of the edge. Therefore, in this work, data on the maximum deflection of the semicircular cantilever are accumulated in Table 5.3. The average and standard deviation within the same absorber sample are calculated in the right 2 columns of the table.
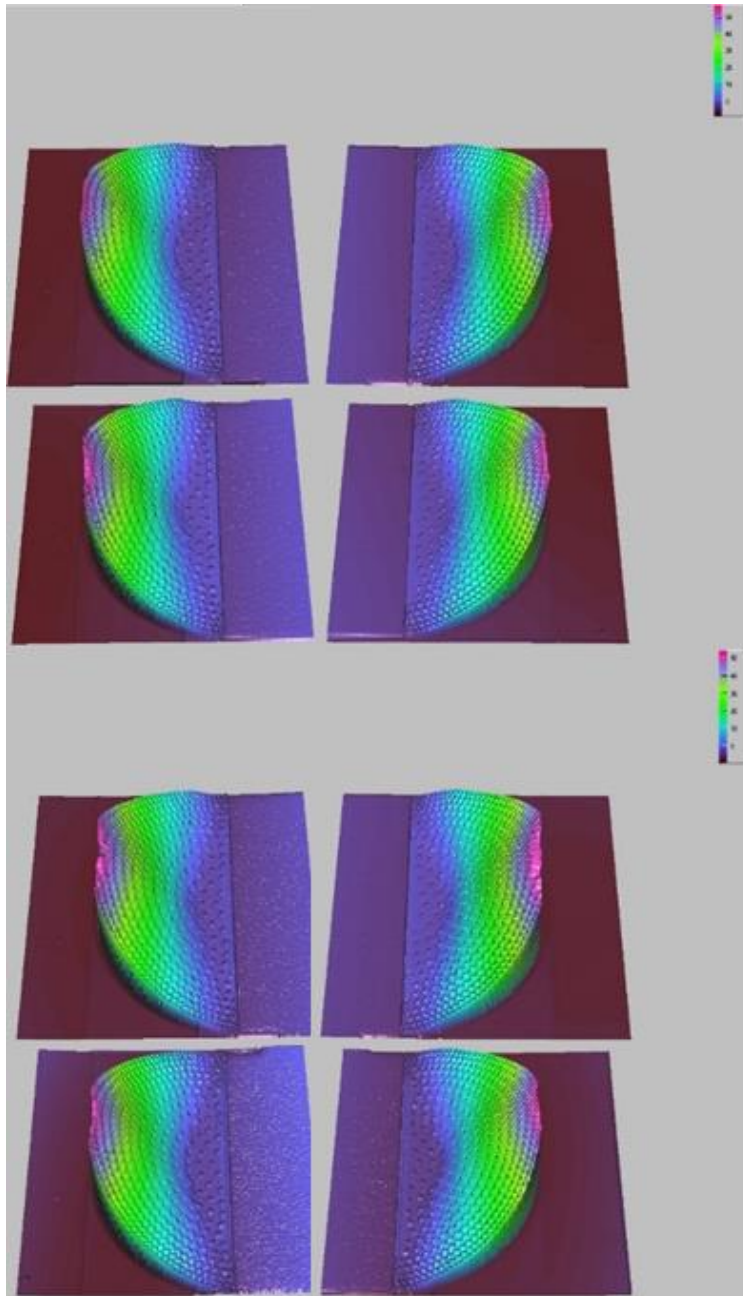
Figure 5.7. Optical 3D surface profile of released MEMS cantilevers in absorber sample

Table 5.3. Data on the maximum deflection of each semicircular cantilever in each fabricated sample   (unit : μm)

Sample	Unit cell (upper)				Unit cell 2 (lower)				Average	Standard deviation
	Left		Right		Left		Right			
#1	57.6	54.5	57.0	56.6	53.9	55.0	54.6	57.0	55.8	1.3
#2	42.0	50.9	40.4	53.0	46.6	49.6	40.0	46.0	46.1	4.6
#3	57.7	57.5	61.3	51.2	57.4	56.8	48.0	59.4	56.2	4.1
#4	56.9	55.9	63.8	64.7	55.1	50.0	55.2	65.0	58.3	5.2
#5	52.3	54.3	55.9	56.0	57.3	65.1	57.7	58.3	57.1	3.5
#6	48.9	50.9	46.2	54.9	48.0	49.8	43.2	56.2	49.8	4.0
#7	40.0	48.0	42.5	52.0	40.8	47.2	45.3	44.8	45.1	3.7
#8	48.5	51.5	52.4	51.6	44.7	45.7	46.0	42.4	47.9	3.5
#9	47.9	50.4	54.0	52.5	50.3	44.0	52.5	51.4	50.4	3.0
#10	43.9	43.0	43.3	48.5	47.8	45.9	44.0	44.5	45.1	1.9
#11	52.6	59.8	58.0	59.4	56.7	58.5	56.6	57.5	57.4	2.1
#12	61.9	58.5	60.5	54.3	50.4	55.7	62.9	56.2	57.6	3.9
#13	48.1	47.5	48.8	44.4	44.8	43.8	46.3	45.9	46.2	1.7
#14	47.1	48.3	53.5	51.7	47.7	45.2	52.7	50.0	49.5	2.7
#15	45.4	59.2	61.0	58.8	57.3	59.0	61.0	62.1	58.0	5.0
#16	47.3	50.5	51.1	52.9	45.0	44.7	48.3	48.6	48.6	2.7
#17	46.0	45.8	50.2	52.3	46.3	45.4	49.6	47.5	47.9	2.4
#18	53.0	52.5	56.2	57.8	58.8	56.7	58.0	56.8	56.2	2.2

The average value of the average deflection of each sample is 51.8 μm, and the average standard deviation among each standard deviation of the absorber sample is 3.1 μm.

The end-tip deflection data are plotted in Figure 5.8 by the number of additional ashing cycles with a 2 min step time after the 4 cycles of the 5 min step time in the ashing process. Thirty-two cantilever end-tip deflections from 4 samples

are measured after the additional 4 cycles of the 2 min ashing process. Moreover, 48 cantilever end-tip deflections from 6 samples are measured after an additional 5 cycles of the 2 min ashing process. Next, 32 cantilever end-tip deflections from 4 samples are measured after an additional 6 cycles of the 2 min ashing process, and 32 cantilever end-tip deflections from 4 samples are measured after an additional 7 cycles of the 2 min ashing process. The average deflections are 45.6, 49.0, 56.5, and 57.0 μm, and the standard deviations of the deflection are 3.3, 3.3, 3.6, and 3.9 μm after 4, 5, 6, and 7 cycles of additional ashing, respectively. Furthermore, the deflection of the end-tip can be controlled by modifying the step time and the total number of the plasma ashing cycles.
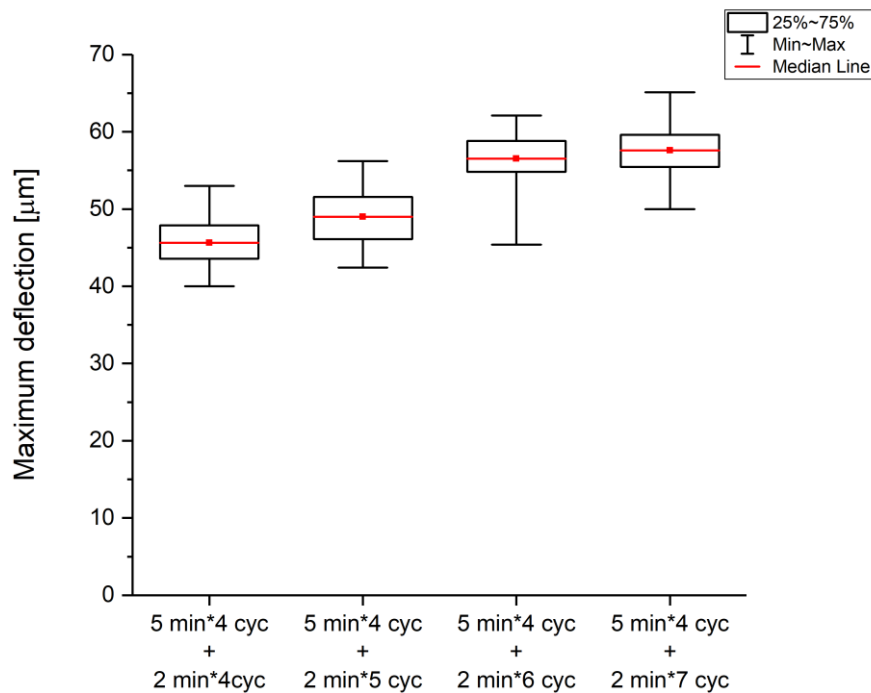
Figure 5.8. End-tip deflection of the MEMS cantilever according to the number of ashing cycles

5.4 Simulation

5.4.1 Simulation setup

Full wave simulation is performed with a commercial FEM simulation tool (HFSS, ANSYS). Electromagnetic simulation is performed with a total schematic of the metamaterial unit cell, absorber sample, and waveguide. These schematics are built by the parameter of absorber described in Section 5.2.2. and waveguide dimension explained in Section 3.5. The real measured profile of the cantilever by a 3D surface profiler is utilized as a schematic of the cantilever. As already mentioned before, the form factor of WR-34 is 8.636 mm × 4.318 mm. The bias lines, the common electrode, and the driving electrode are not built as a model due to the computing memory limitation. Also, the screw used to tighten up the upper and lower waveguide is assumed to as a titanium metal. All the material properties except for the borofloat glass are derived from the system library. The solution type of the simulation is driven modal, and the network analysis is utilized as driven options. Figure 5.9. shows the port information and boundary condition of full-wave electromagnetic simulation. Port 1 is set as the upper waveguide input terminal, and port 2 is set as the lower waveguide. The line is defined in each port excitation since the electric field direction is always parallel to the shorter dimension in a rectangular waveguide. The position is drawn considering the dimension of WR-34. Furthermore, two boundary conditions are set in the model. The aluminum backside ground plane for the absorber is set as finite conductivity. Another boundary condition, the

119

radiation box, is built to restrain space for accurate electromagnetic field calculation. The number of passes are restricted to 35 times due to the computing memory limitation. The maximum Delta S is 0.025. The number of passes, and minimum converged passes are 2,2, respectively. The rest of the simulation option is set to default. The sweep type is interpolating.
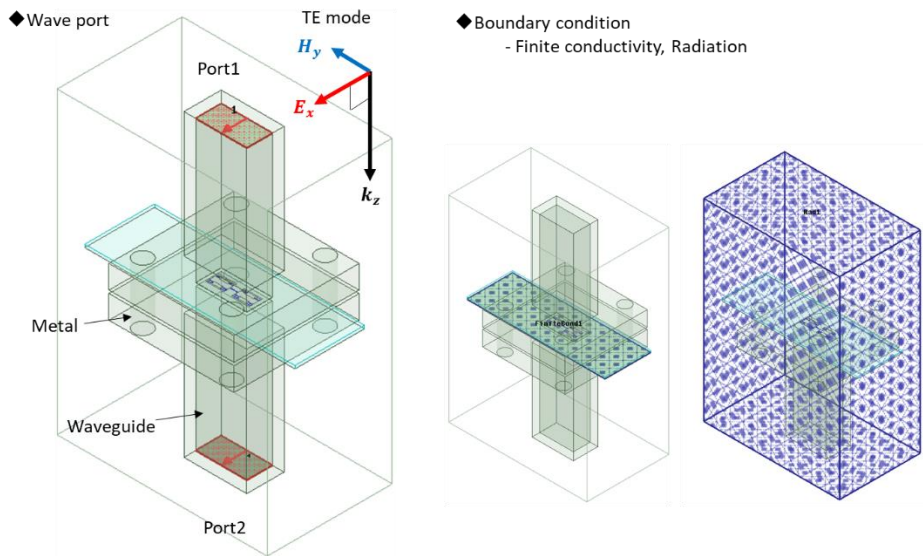
Figure 5.9. Simulation setup in HFSS

The most significant simulation variable is to know the exact dielectric constant and tangent loss of the absorber substrate because the glass permittivity is the key factor in calculating impedance matching. For the free space dielectric constant of borofloat glass, the dielectric constant and tangent loss were measured at the Korean Institute of Material Science. A split cylinder cavity resonator (EMLabs,

CR-728) is used as the method for low loss, a thin glass substrate. In dielectric constant measurement, the glass substrate was polished until the thickness is under 250 μm by the CMP process. The length and the width for measurement are 34 mm and 50 mm. The commercial post calculation software (N1500A, Keysight Corp.) is used to calculate the dielectric constant. The real part of the dielectric constant is about 4.4769, and the tangent loss is 0.008799. However, since this research is for TE mode waveguide, the dielectric is the measure before the dielectric constant used in this thesis is 4.2, and tangent loss is assumed as 0.07. Table 5.4 shows the different values of the dielectric constant of a borofloat glass.

Table 5.4. Dielectric constant of Borofloat 33

	Dielectric constant (ε_r)	Tangent loss ($\tan \delta$)	Frequency in document
Schott datasheet	4.5	0.012	24 GHz
Corning datasheet	4.6	0.004	1 MHz
Dssemicon datasheet	4.6	0.0037	1 MHz
Watanabe et al. [150]	5.4	0.006	28 GHz
Sissoko et al. [151]	3.9	0.012	upto 7 GHz
Zhao et al. [152]	4.4	0.0058	1GHz
DARPA NETEX	4.3	0.0047	
Measurement in KIMS	4.476974	0.008799	28 GHz

5.4.2 Simulation results

To examine the tunability of the proposed absorber, the reflection coefficients are simulated according to different reconfiguration states depending on the voltage applied to the separate electrodes. As mentioned before, four pairs of cantilevers are actuated separately by each electrode. Assuming that the voltage is turned on sequentially from electrode 1 to electrode 4, the eight cantilevers bent upwards undergo a reconfiguration state change by pulling down two by two. Therefore, the two unit cells undergo 5 different states including an initial state. Full-wave electromagnetic simulation is performed with the five different structures from the five states. The structure of the pulled-down cantilevers is assumed to be flat in the simulation. The structure of the MEMS cantilevers bent upward is constructed by the profile from the test cantilever sample with a 50.0 μm maximum deflection at the end-tip. At initial off-state, when all the cantilevers are bent upward, the simulated resonance frequency, the reflection coefficient, and the transmission coefficient are 32.95 GHz, -9.11 dB, and -65.27 dB, respectively. When the right two semicircular cantilevers of upper cells are pulled down, in which is reconfiguration state 2, the simulated resonance frequency, the reflection coefficient, and the transmission coefficient are 32.42 GHz, -35.43 dB, and -65.90 dB, respectively. For the reconfiguration state 3, in which the two right cantilevers of each cell are pulled down, the simulated resonance frequency, the reflection coefficient, and the transmission coefficient are 30.47 GHz, -11.98 dB, and -64.68 dB, respectively. After, the left two wings are pulled down in the lower cell, the simulated resonance frequency, the reflection coefficient, and the transmission coefficient are 29.00 GHz, -24.17 dB, and -64.68 dB, respectively. Finally, when all the cantilevers are pulled

down in both upper and lower cells, the simulated resonance frequency, the reflection coefficient, and the transmission coefficient are 28.48 GHz, -15.15 dB, and -63.52 dB, respectively.

Also, the peak absorptivity at each resonance frequency is 87.72, 99.97, 93.66, 99.62, and 96.94%, respectively All the numbers previously mentioned are well descripted in Table 5.5.

Figure 5.10 shows the simulated results of the 5 states with different reconfigurations of the metamaterial absorber. The simulation results of state 2 and state 4 show an additional minor resonance point due to the asymmetry of the structure in the upper cell and lower cell at state 2 and state 4. This will be thoroughly discussed later in Section 5.6.

Table 5.5. Simulation results of the 3rd design

State	Resonance frequency	Reflection coefficient	Transmission coefficient	Peak absorptivity
State 1	32.95 GHz	-9.11 dB	- 65.27 dB	87.72 %
State 2	32.42 GHz	-35.43 dB	- 65.90 dB	99.97 %
State 3	30.47 GHz	-11.98 dB	- 63.21 dB	93.66 %
State 4	29.00 GHz	-24.17 dB	- 64.68 dB	99.62 %
State 5	28.48 GHz	-15.15 dB	- 63.52 dB	96.94 %
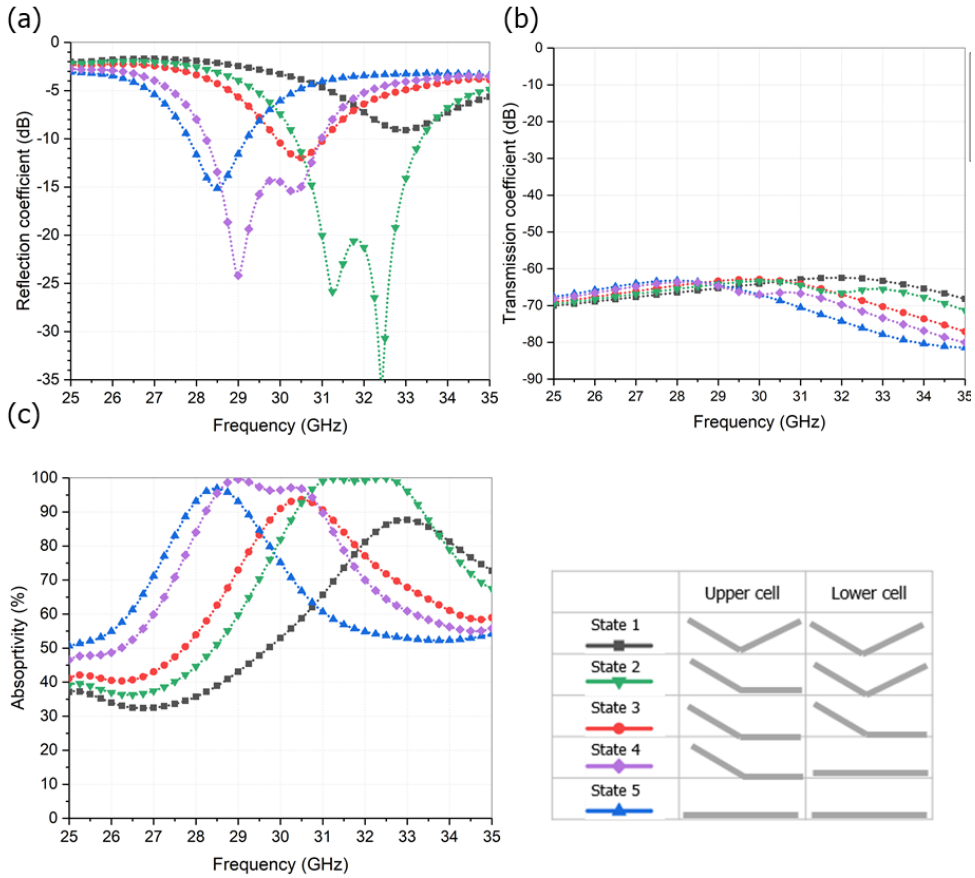
Figure 5.10. Simulation results of the 3rd absorber: (a) Reflection coefficient (b) Transmission coefficient and (c) Absorptivity

A simulation of the electromechanics is also performed with the FEM simulation tool. The pull-in voltage is calculated with the same structure used for the electromagnetic simulation, cantilevers with slightly higher deflection and slightly lower deflection. Each initial deflection is set to be 40, 50, and 60 μm, respectively. The pull-in voltage is calculated to be 37.9 V for the stress-induced semicircle shape cantilever with 50.0 μm of initial deflections. The calculated capacitance between the cantilever with 50.0 μm deflection and the bottom driving electrode is 0.130 pF. Assuming the semicircle shape is pulled down to a flat profile, the capacitance is

0.469 pF from the simulation result. Since the absorber has a total of 8 cantilevers, the total capacitance change is 8 times the single cantilever contains. However, when the pull-in occurs, the cantilever sticks to the bottom oxide layer meaning a lower profile than the initial flat profile. Moreover, the semicircular cantilever has a narrow analog tuning range since the pull-in occurs after only 10 µm deflection is pulled down. Figure 5.11 (a) shows the electromechanical simulation by a commercial FEM tool called COMSOL. Figure 5.11 (b) is the deflection graph according to the applied voltage.
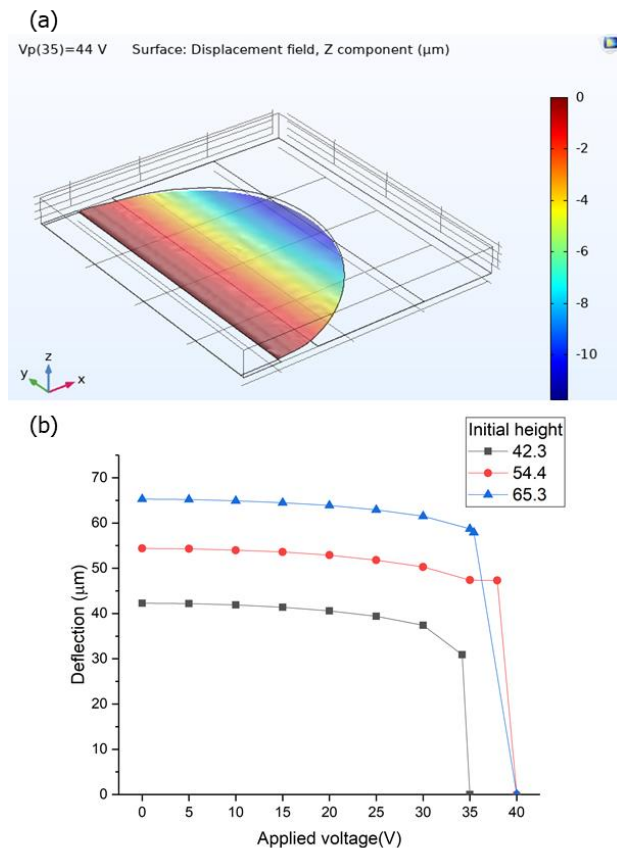
Figure 5.11. COMSOL simulation of electrostatic driving

5.5 Experiment

5.5.1 Experiment setup

The absorber sample used for the experiment showed 8 MEMS cantilevers end-tip deflections of 46.0, 45.8, 50.2, 52.3, 46.3, 45.4, 49.6, and 47.5 μm. The average end-tip deflection is 47.9 μm, and the standard deviation is 2.4 μm.

Since the absorber size is larger than the waveguide and the absorber sample is aligned between two waveguides, it is extremely difficult to align and implement the absorber sample between waveguides. Therefore, for the experiment, the absorber sample is implemented with a printed circuit board (PCB) to accurately align the absorber sample between the waveguides. This absorber sample is attached to a customized PCB jig with epoxy while electrodes on the absorber are connected to the extended bias lines in the PCB jig with wire bonding.

Figure 5.12 (a) is the schematic of the absorber sample, PCB jig, and bottom PCB jig. PCB jigs have a hole in the middle. After, integrating two PCB jigs into the absorber sample, driving electrodes in the absorber sample are connected to the wire in the PCB by wire bonding. Gold wire bonding is conducted outside the laboratory (Daesin semiconductor corp.) After alignment of the absorber-jig sample and two waveguides, four screws are locked up as shown in Figure 5.12 (b). The real photographs of the absorber-PCB jig sample and implementation process are depicted in Figure 5.13.
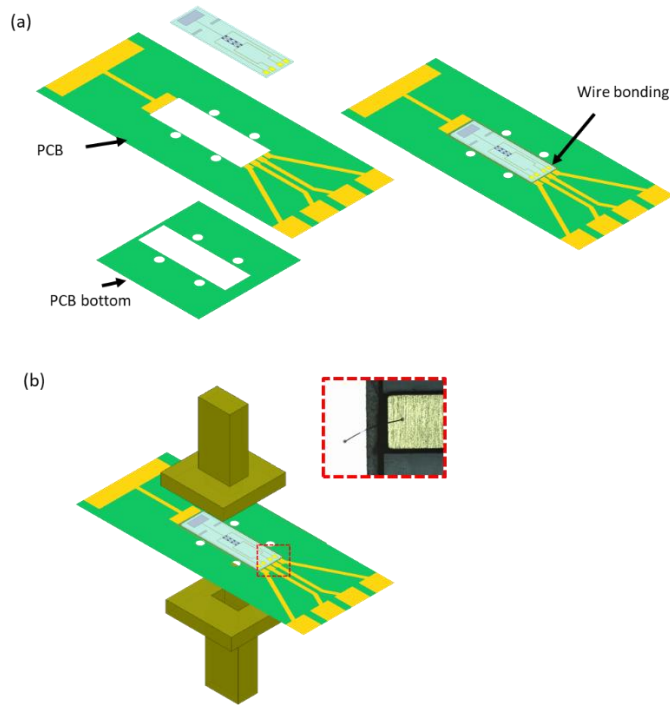
Figure 5.12. Waveguide implementation setup: (a) Fabrication schematic of absorber sample and PCB jig layer (b) Implementation of wire-connected absorber-PCB sample and waveguide Inset : microscope image of connection with wire
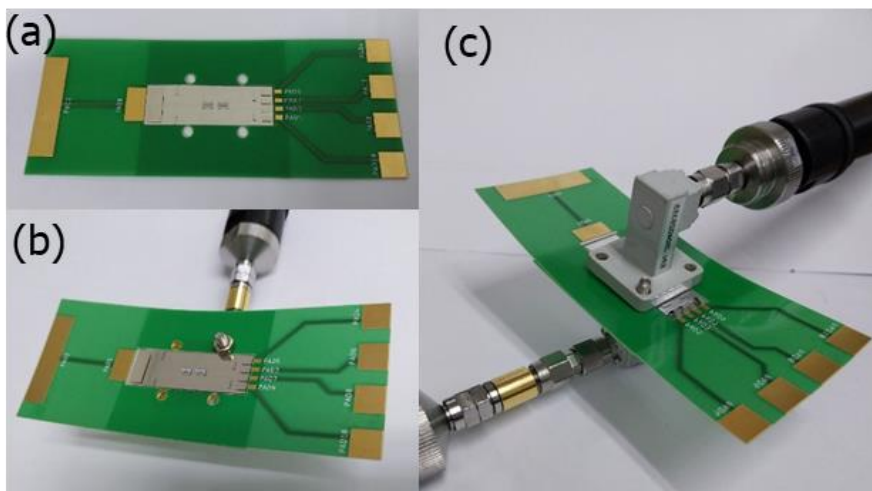
bonding

Figure 5.13. Waveguide implementation setup: (a) Photographs of wire-

connected absorber-PCB sample (b) Absorber sample fixed to lower wave guide (c) Fully integrated sample and waveguide

The reflection coefficients of the fabricated sample were measured with an Agilent network analyzer (N5227B, Keysight Technologies Corporation). The overall measurement setup is shown in Figure 5.14. The fabricated absorber sample connected to the PCB jig is precisely aligned and embedded between the two waveguides (34WCAK_Cu, A-info Corporation) after the calibration of the network analyzer. For measuring the 22 to 33 GHz frequency range, the corresponding waveguide form factor is 8.636 mm × 4.318 mm. After the assembly process, the wires are made to contact with all the driving electrodes and the common electrode for applying a driving voltage to reconfigure the cantilever arrays. After connecting the wires to the switches and a power supply, 80 V of DC bias is sequentially applied from electrode 1 to electrode 4 of the absorber sample while measuring the *S*-parameters using the network analyzer. After the instantaneous frequency movement of the graph was seen and stabilized, the *S*-parameters are measured. Figure 5.15 is the photographs of the network analyzer and waveguide setup.
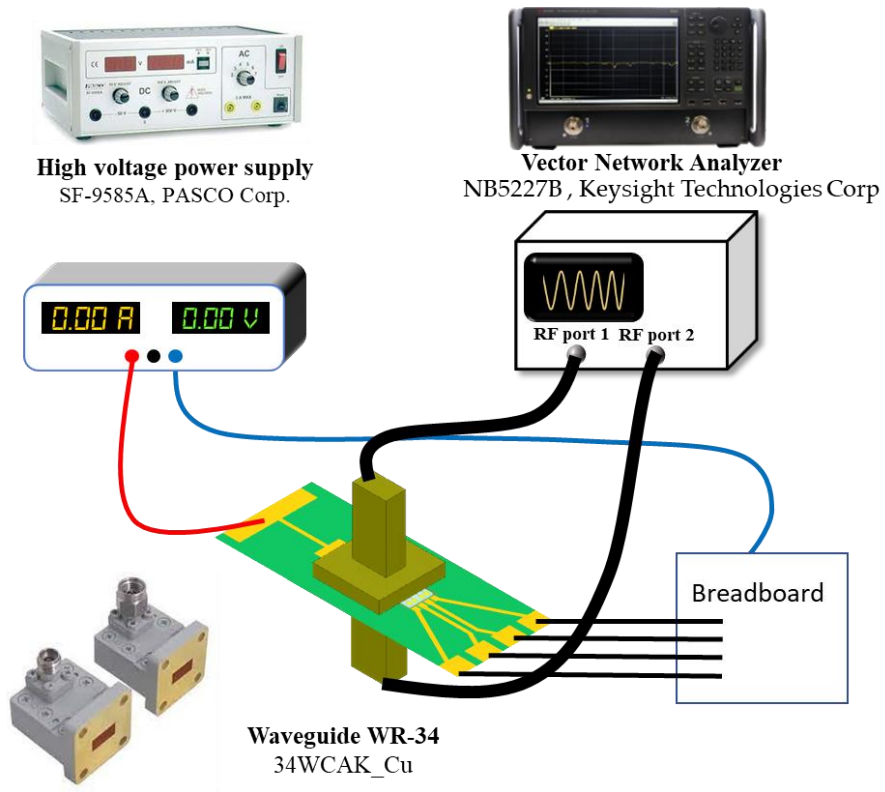
Figure 5.14. Experiment setup: Network analyzer, High voltage power supply,

Wave guide

Figure 5.15. Photographs network analyzer and waveguide setup

5.5.2 Preliminary experiment

To verify that the LC resonance structure is formed by the cantilever structure, a simple measurement of *S*-parameters is performed. First of all, borofloat glass substrate only with backside aluminum film ground plane is measured with same waveguide and same network analyzer. This is a sort of knowing the dielectric constant of a glass substrate and the process of calibration for the next RF characterization. As shown in Figure 5.16, any resonance occurs in the 25 to 35 GHz frequency range. Therefore, the reflection coefficient is below 3dB and the transmission coefficient is near -60 dB.
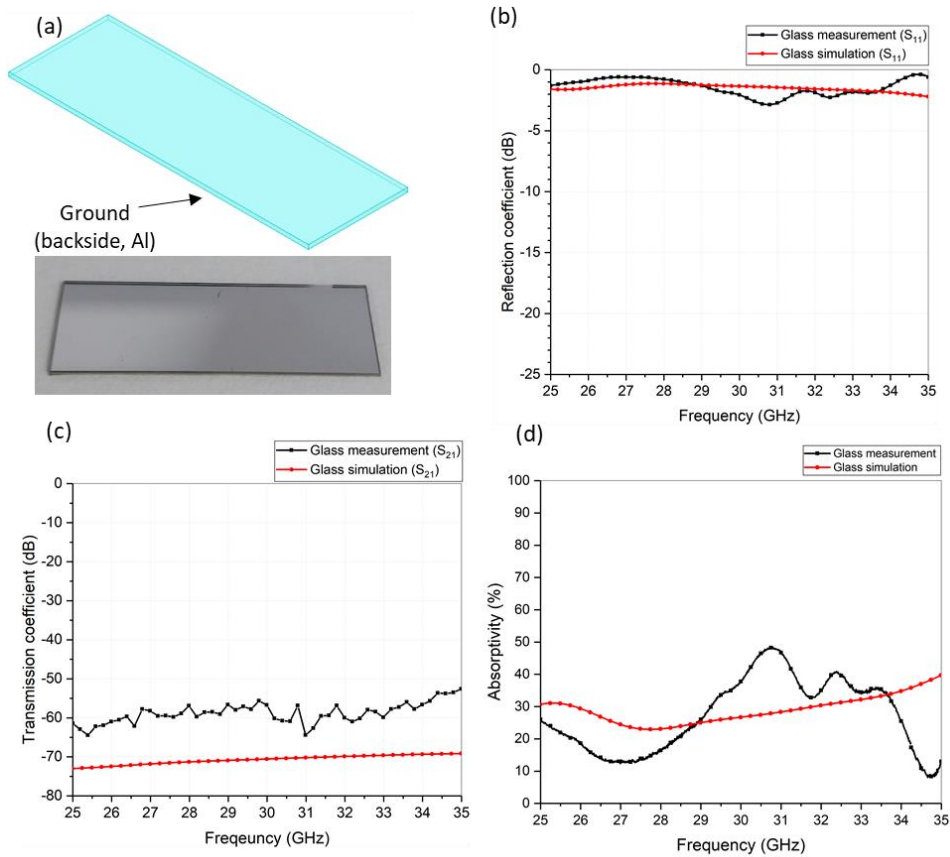
Figure 5.1.6 Measurement of substrate with ground plane (a) Schematic of borofloat glass with backside Al ground plane (b) Reflection coefficient (c) Transmission coefficient and (d) Absorptivity of borofloat glass with backside ground plane

Furthermore, the sample with bottom aluminum SRR structure deposition is measured by a network analyzer. This procedure is also the same verification of MEMS metamaterial absorber. As shown in Figure 5.17, both the simulated and measured reflection coefficient is below -5 dB, and both the simulated and measured transmission coefficient is near -60 to -70 dB.
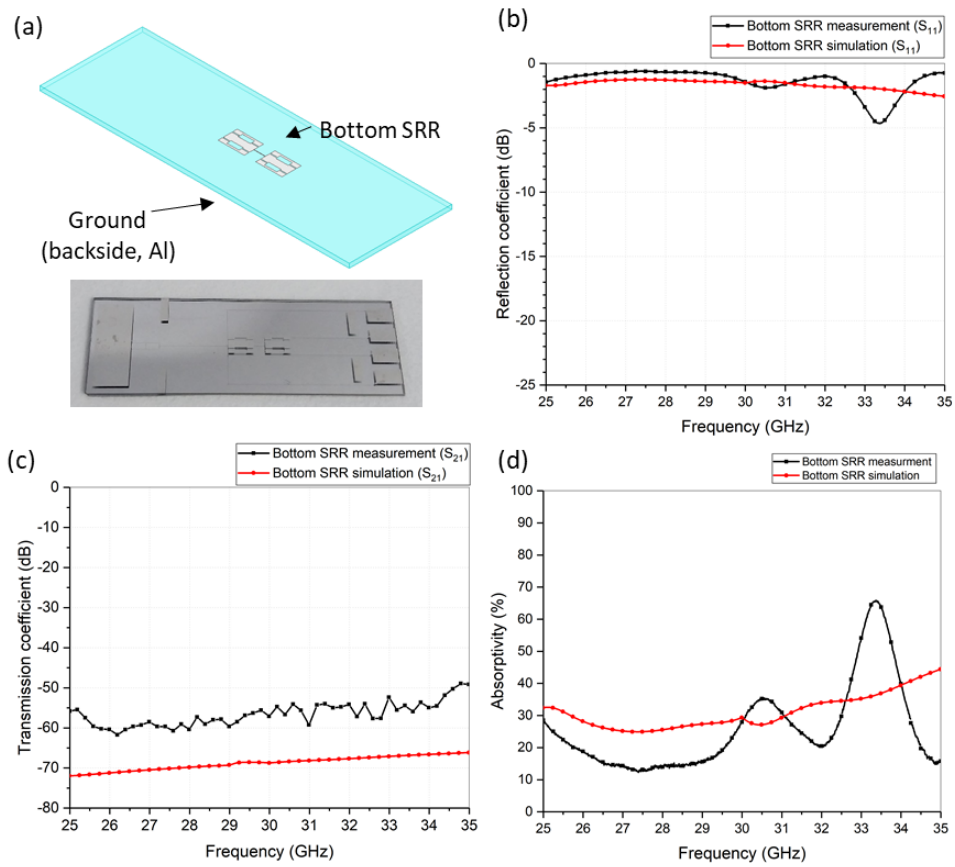
Figure 5.17. Measurement of bottom SRR (a) Schematic of the bottom SRR (b) Reflection coefficient (c) Transmission coefficient and (d) Absorptivity of the bottom SRR

5.5.2 Experiment results

      Figure 5.18 (a) is the microscope image of the initial off-state and (b) is the pull-in state. As shown in the figure, it can be seen the twinkle of light when voltage is not applied. When the semicircle cantilever is pulled down flat by applying over pull-in voltage, the shape of etch hole and the space between etch hole are well seen.
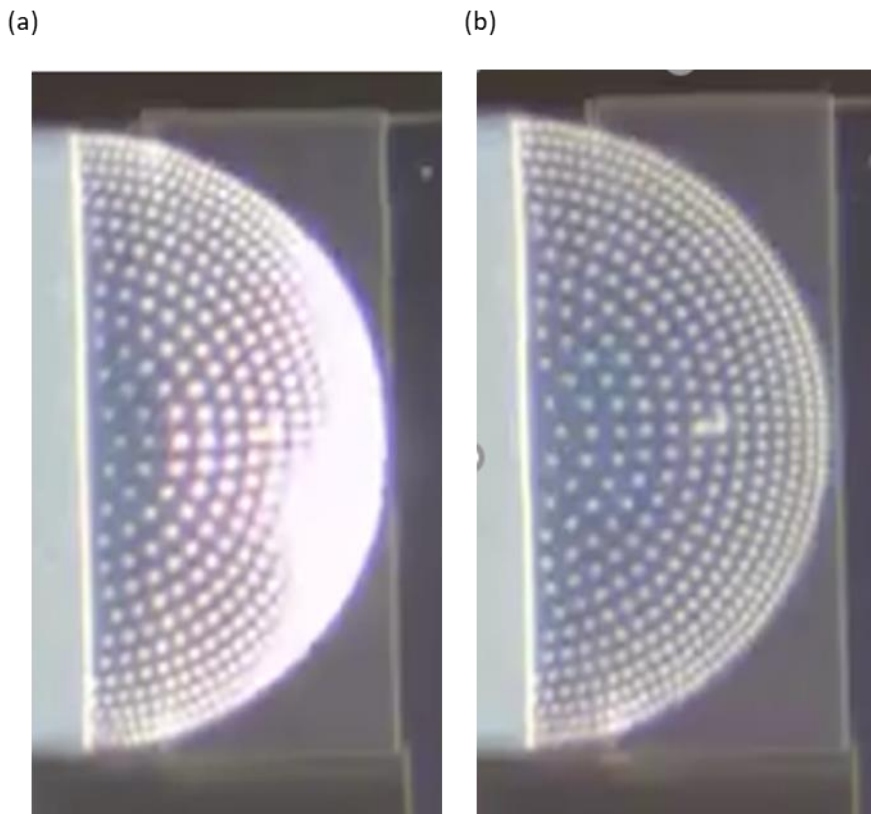
Figure 5.18. Microscope image (a) Initial-off state (b) Pull-in state

Table 5.6 show the results of the reflection coefficient and absorptivity, respectively, measured while applying 80 V of DC bias on electrode 1 to electrode 4 sequentially. At initial off-state, when all the cantilevers are bent upward, the simulated resonance frequency, the reflection coefficient, and the transmission coefficient are 32.95 GHz, -7.20 dB, and -45.59 dB, respectively. When the right two semicircular cantilevers of upper cells are pulled down, which is reconfiguration state 2, the simulated resonance frequency, the reflection coefficient, and the transmission coefficient are 32.07 GHz, -9.27 dB, and -41.60 dB, respectively. For the reconfiguration state 3, in which the two right cantilevers of each cell are pulled down, the simulated resonance frequency, the reflection coefficient, and the transmission coefficient are 30.10 GHz, -8.63 dB, and -42.81 dB, respectively. After, the left two wings are pulled down in the lower cell, the simulated resonance frequency, the reflection coefficient, and the transmission coefficient are 29.37 GHz, -21.02 dB, and -41.22 dB, respectively. Finally, when all the cantilevers are pulled down in both upper and lower cells, the simulated resonance frequency, the reflection coefficient, and the transmission coefficient are 28.87, -8.70 dB, and -39.48 dB, respectively. From state 1 to state 5, the measured peak absorption rates at each state are 80.95 %, 88.17 %, 86.29 %, 99.21 %, and 86.51%, respectively.

Table 5.6. Measurement results of the 3rd design

State	Resonance frequency	Reflection coefficient	Transmission coefficient	Absorptivity
State 1	32.95 GHz	- 7.20 dB	- 45.59 dB	80.95 %
State 2	32.07 GHz	- 9.27 dB	- 41.60 dB	88.17 %
State 3	30.10 GHz	- 8.63 dB	- 42.81 dB	86.29 %
State 4	29.37 GHz	- 21.02 dB	- 41.22 dB	99.21 %
State 5	28.87 GHz	- 8.70 dB	- 39.48 dB	86.51 %

Figure 5.19. shows the measurement result of the reflection coefficient and the absorptivity. The tuning range from the initial off state 1 to all the pulled down state 5 is Δf=4.08 GHz, and the tuning ratio ($\frac{\Delta f}{f}$) is 12.4%. In the case of the resonant frequency, the difference between the experimental and simulation results was within 0.39 GHz error. However, the magnitudes of the reflection coefficients are lower than the simulation results. It is presumed that the loss occurred because the two waveguides did not engage precisely due to a gap created by the substrate of the absorber sample. The comparison between measurement and the simulation results is clearly well depicted in Table 5.7.
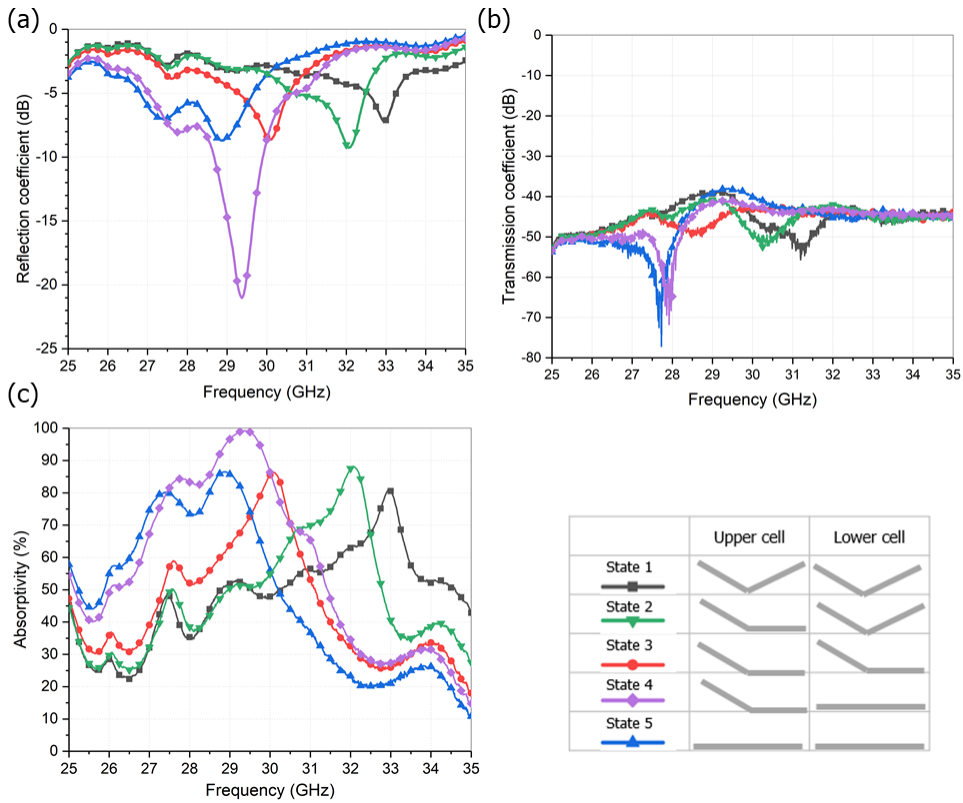
Figure 5.19. Measurement results of the 3rd absorber: (a) Reflection coefficient (b) Transmission coefficient and (d) Absorptivity

Table 5.7. Comparison of measurement and simulation results

State	Measurement		Simulation		Error
	Resonance frequency	Reflection coefficient	Resonance frequency	Reflection coefficient	
State 1	32.95 GHz	- 7.20 dB	32.95 GHz	-9.11 dB	-
State 2	32.07 GHz	- 9.27 dB	32.42 GHz	-35.43 dB	0.35 GHz
State 3	30.10 GHz	- 8.63 dB	30.47 GHz	-11.98 dB	0.37 GHz
State 4	29.37 GHz	- 21.02 dB	29.00 GHz	-24.17 dB	0.37 GHz
State 5	28.87 GHz	- 8.70 dB	28.48 GHz	-15.15 dB	0.39 GHz

5.6 Further Analysis

5.6.1 The waveguide simulation

The reflection measurement of the electromagnetic absorber is thoroughly studied with the rectangular waveguide. The rectangular waveguide method is a way to measure signals by putting them into a closed rectangular waveguide and exciting it with an $\vec{H}$-plane polarized extension waveguide transition. This method eliminates external electromagnetic interference and edge diffraction. In a rectangular waveguide, the path of an incident wave having an incident angle θ and the path of a reflected wave are displayed as shown in Figure 5.20.
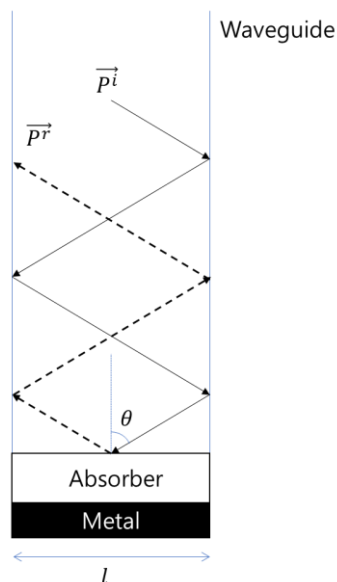
Figure 5.20. The path of incident wave with incident angle θ and the path of reflect wave

The incident angle θ could be calculated with the length of the waveguide l and wavelength λ by following equation.

$$\theta = \sin^{-1}\frac{\lambda}{2l} \qquad \text{Eqn. 5.1}$$

The measuring of the reflection coefficient is not proper for a wave with vertical incidence but is suitable for oblique incidence. Even though the measurement using a waveguide cannot entirely elaborate on the absorber properties, the reflection coefficient value using the rectangular waveguide is very similar to the value measured using the arch-method [153]. Due to the simplicity and effectiveness, many research are published with reflectivity results using the waveguides [57, 154, 155].

This thesis is researched and measured based on the waveguide setup for the above reason. All those the above simulations until this section are performed considering the entire schematic of the waveguide. In this thesis, the apertures of the WR-34 waveguide for an experiment are 8.636 mm × 4.318 mm. Therefore, the incident angle at 30 GHz is about $\theta = 35.4°$. Also, the waveguide WR-34 is only effective in measuring TE_{10} mode.

A FEM simulation is conducted with another mode in port 1, especially, for TE_{10} and TE_{01} to investigate whether the absorber is independent of the electric field direction. Figure 5.21 are the electric field distribution at each TE_{10} and TE_{01} mode. The simulation results at state 5 are shown in Figure 5.22.

TE$_{10}$ mode   TE$_{01}$ mode
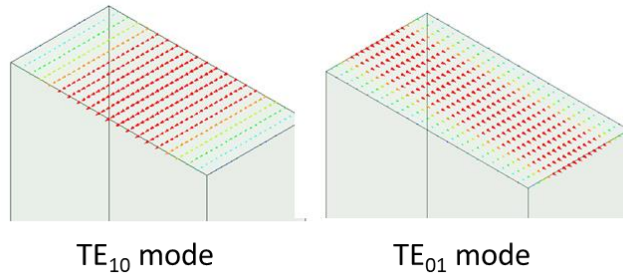
Figure 5.21. Electric field distribution in TE$_{10}$, TE$_{01}$ mode on simulation setup considering waveguide
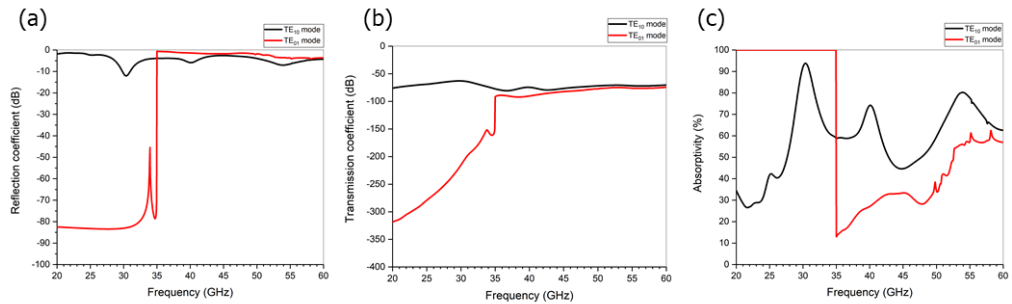
Figure 5.22. Simulation results of TE$_{10}$ and TE$_{01}$ mode at all-pull-down state (state 5) (a) reflection coefficient (b) transmission coefficient (c) absorptivity

However, a wave with a certain mode can only propagate at frequencies above the cutoff frequency. To consider the cutoff frequency, the cutoff wavenumber should be defined. The cutoff wavenumber is a function of the m and n indexes of mode.

$$k_{c_{m,n}}^2 = \left(\frac{m\pi}{a}\right)^2 + \left(\frac{n\pi}{b}\right)^2 \qquad \text{Eqn. 5.2}$$

Then, the cutoff frequency is

$$f_{c_{m,n}} = \frac{k_{c_{m,n}}}{2\pi\sqrt{\mu\varepsilon}} \qquad \text{Eqn. 5.3}$$

There is no significant meaning in TE01 mode because the cutoff frequency exceeds the frequency range of the WR-34 waveguide. Table 5.8 indicates the cut-off frequency of major modes in the Ka-band waveguide.

Table 5.8. Cut-off frequencies of major modes in Ka-band waveguide

Mode	Cut-off frequency (GHz)
TEM	Not supported
TE_{10}	21.07 GHz
TE_{01}	42.15 GHz
TE_{11}	47.13 GHz
TM_{10}	Not supported
TM_{01}	Not supported
TM_{11}	47.13 GHz

5.6.2 The periodic metamaterial unit cell simulation

In this section, the simulation of a periodic metamaterial unit cell is performed to verify the characteristic of the designed absorber. Figure 5.23. shows the periodic boundary condition using primary/secondary coupled boundary (master/slave in an older version of HFSS) to find out the absorber properties according to $\vec{E}$-field polarization and $\vec{E}$-field incident angle.
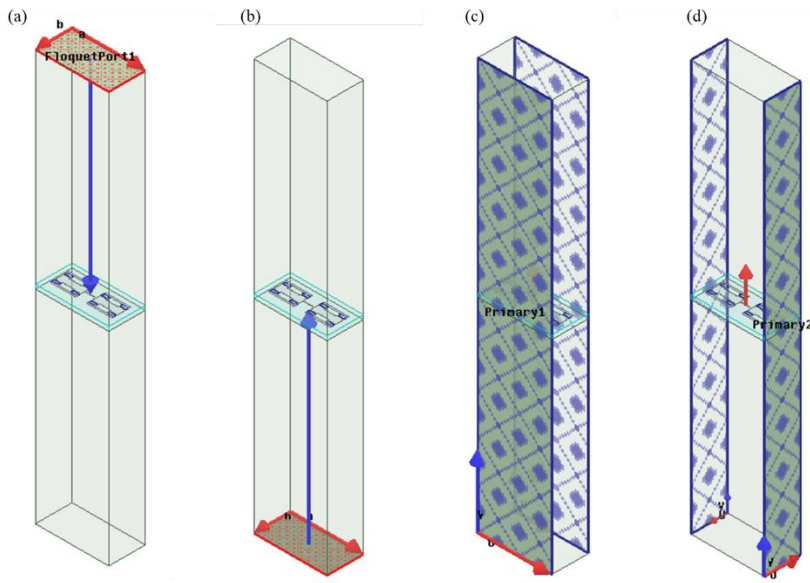
Figure 5.23. Periodic boundary condition in FEM simulation (a) Floquet port 1 (b) Floquet port 2 (c) Coupled boundary condition for x-axis (d) coupled boundary condition of y-axis

Figure 5.24 (a). is the comparison of the reflection coefficients when $\vec{E}$-field is applied in angle with 0° with having only y-axis polarization component and x-axis polarization component at all pull-down state (state 5). In this consideration, the y-axis polarization corresponds to the TE_{01} mode in the rectangular waveguide measurement, and the x-axis polarization corresponds to the TE_{10} mode in the rectangular waveguide measurement. Figure 5.24 (c) and (d) is the comparison of the transmission coefficients and absorptivity when $\vec{E}$-field is applied in an angle at in of 0 ° with having only a y-axis polarization component and x-axis polarization component. However, as mentioned above, the calculated incident angle in a rectangular waveguide is about 35°. Therefore, to verify the measurement results of the rectangular waveguide with the periodic unit cell simulation, the reflection coefficient, the transmission coefficient, and the absorptivity simulation results of $\vec{E}$-field having only x-axis polarization and 35 degrees incident angle should be compared. Figure 5.24 (b), (d), (e) are the reflection coefficient, the transmission coefficient, and the absorptivity simulation results when $\vec{E}$-field propagates with only x-axis polarization and 35° incident angle. As shown in Figure 5.24 (b), the resonant frequency is about 28.7 GHz, which is similar to the 28.87 GHz of the measurement result.
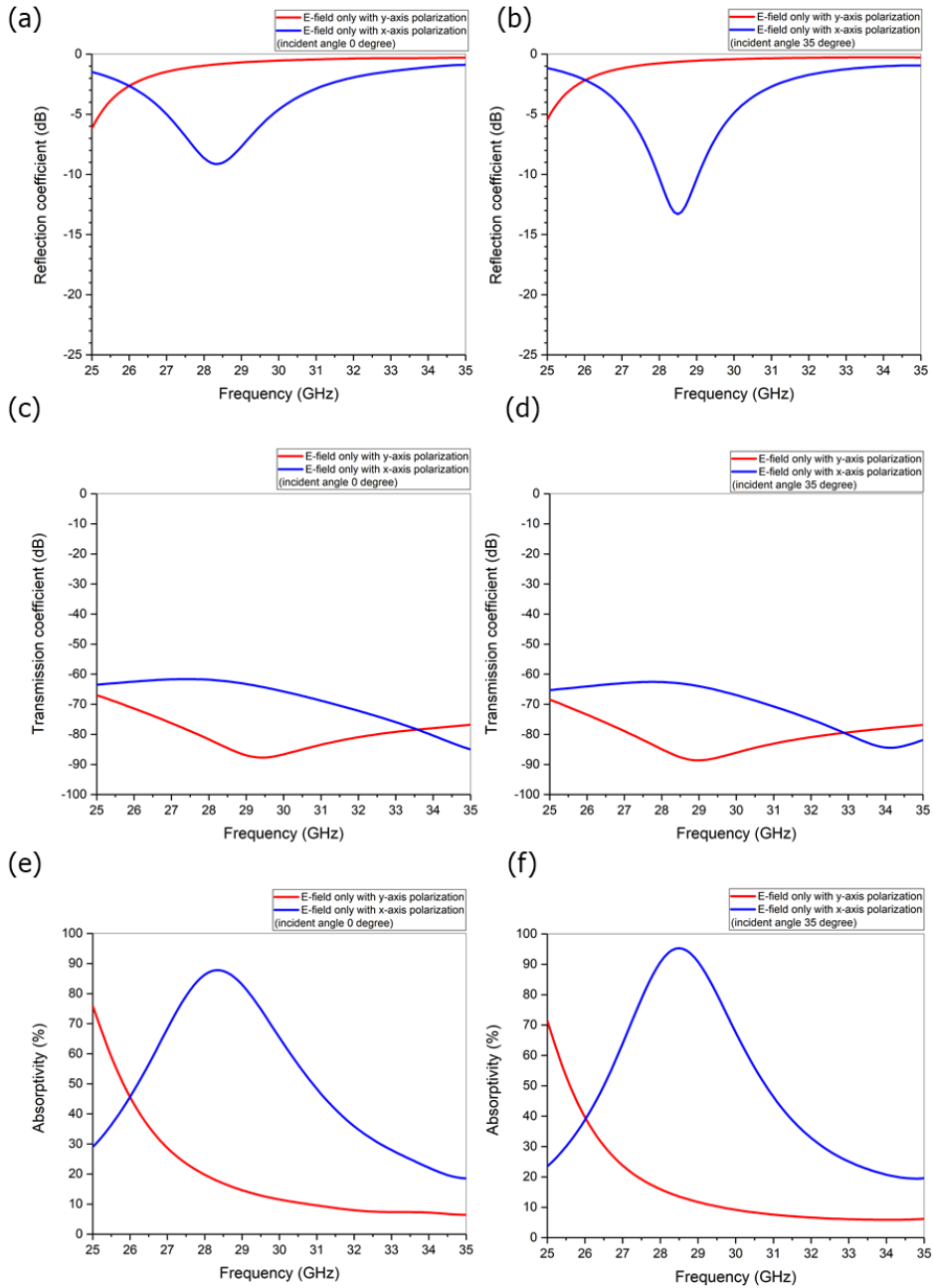
Figure 5.24. Comparison of $\vec{E}$-field properties in all pull-down state (state5) according to *y*-axis polarization (red line in each graph) and *x*-axis polarization (blue line in each graph) at 0° incident angle ((a) Reflection coefficient, (c) Transmission coefficient, (e) Absorptivity) and 35° incident angle ((b) Reflection coefficient, (d)

Transmission coefficient, (f) Absorptivity).

Figure 5.25 (a) is the comparison of the reflection coefficients according to the polarization an angle when $\vec{E}$-field is applied at angle of 0° at all pull-down state (state 5). Figure 5.25 (b) is the comparison of the reflection coefficients according to the polarization angle when $\vec{E}$-field is applied an angle of 35° at all pull-down state (state 5). Figure 5.25 (c) and (d) are the comparison of the transmission coefficients and absorptivity according to polarization angle when $\vec{E}$-field is applied an angle of 0 ° when all the cantilevers are pulled down. Also, Figure 5.25 (c) and (d) are the comparison of the transmission coefficients and absorptivity according to polarization angle when $\vec{E}$-field is applied in angle with 35 ° when all the cantilevers are pulled down. As shown in the graph, the peak absorptivity is sustained above 80 % absorption rate with 45° polarization angle.
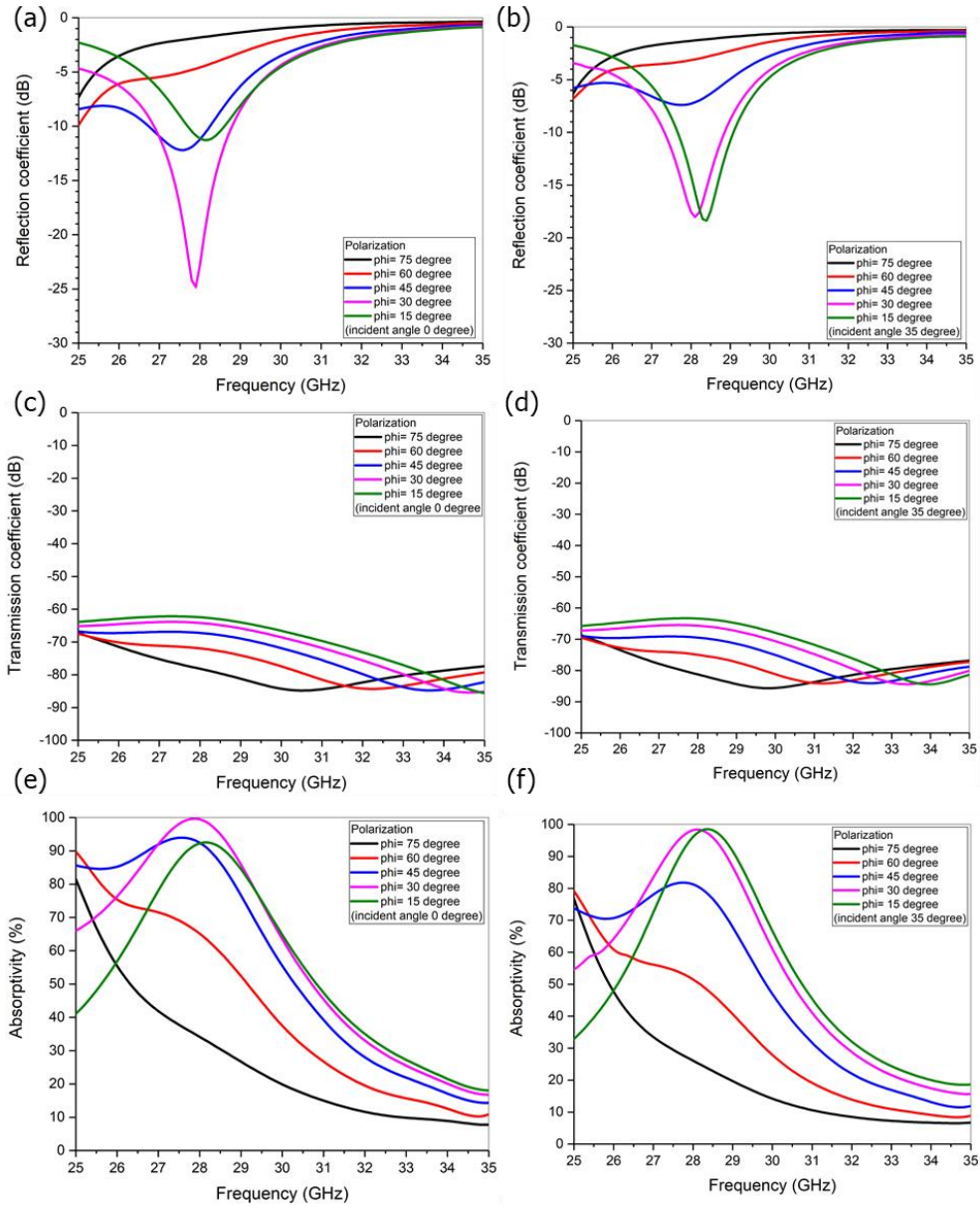
Figure 5.25. $\vec{E}$-field properties according to polarization angle in all pull-down state (state5) at at 0° incident angle ((a) Reflection coefficient, (c) Transmission coefficient, (e) Absorptivity) and 35° incident angle((b) Reflection coefficient, (d) Transmission coefficient, (f) Absorptivity).

Moreover, simulation on the reflection coefficient, the transmission coefficient, and the absorptivity at all pulled-down state according to $\vec{E}$-field incident angle. Figure 5.26 shows the results on the reflection coefficient, the transmission coefficient, and the absorptivity when $\vec{E}$-field is applied with incident angles from 10 ° to 80 °. The peak absorptivity shows the highest values when the incident angle is about 50 °. The peak absorptivity drastically shrinks below 70 % at 80 ° of incident angle.
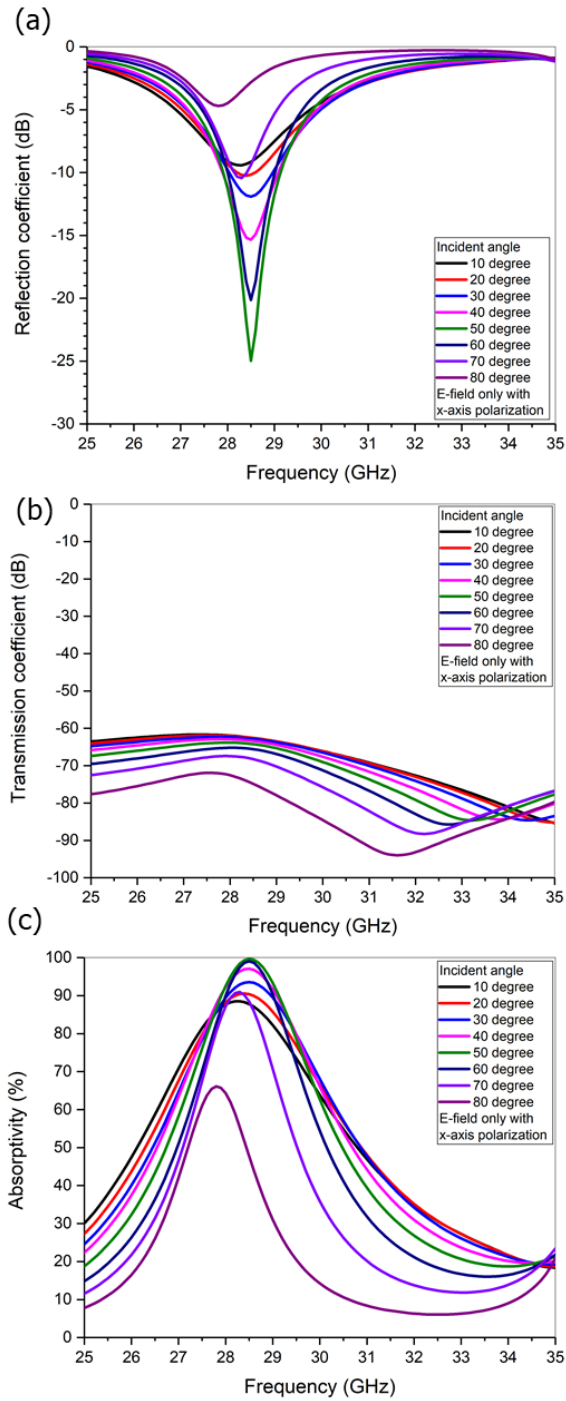
Figure 5.26. Simulation results at all pull-down state according to incident angle (a)

Reflection coefficient (b) Transmission coefficient (c) Absorptivity

5.6.3 Analysis on the surface current

Further information on electric field and surface current can be plotted with the FEM full wave simulation conducted in Section 5.4.2. Since the 3rd design of this thesis research has total of 5 different reconfiguration states, each state is classified as a structural symmetry. For the first initial off-state, the left and the right part of the SRR unit cell is symmetry and also the upper unit cell is identical to the lower SRR unit cell. Figure 5.27. (a), (b) and (c) are the distribution of the electric field, the distribution of the surface current density ($\vec{J}$) intensity, and the vector distribution of the surface current density ($\vec{J}$) at initial off-state 1.

Because the structure is symmetry in state 1, the electric field distribution is symmetry in the left and right parts of the single unit cell, and the electric field is strongly applied at the bottom of the cantilever. The intensity of the surface current density ($\vec{J}$) also shows symmetry within unit cell and is slightly higher near the center of the waveguide as shown in Figure 5.27 (b). Moreover, the current flow of the SRR unit cell can be indicated by taking the vector of the surface current density ($\vec{J}$) account. Strong current flows strongly from the outskirts of the SRR unit cell.
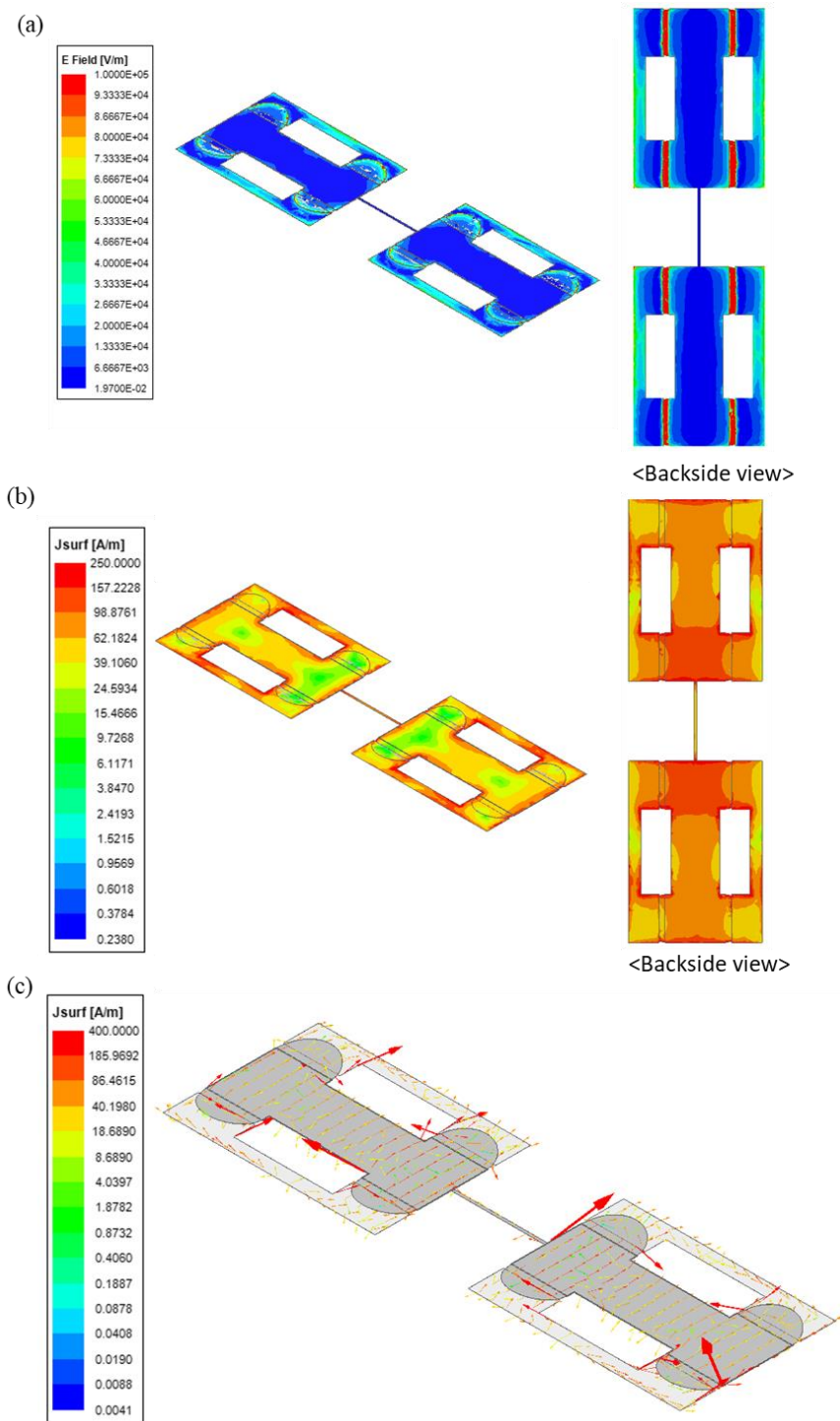
Figure 5.27. (a) $\vec{E}$-field distribution (b) Surface current density $(\vec{J})$ intensity (c) Surface current density $(\vec{J})$ vector at initial off-state 1

Second, the reconfiguration state 2 is an asymmetry structure between unit cells unlike state 1. In state 2, the right set of cantilevers as pulled down while the left part of the upper SRR unit cell and the entire part of the lower unit cell still remains the same. Therefore, the upper cell and the lower cell is not in the identical state. As shown in Figure 5.28 (a), the electric field is much more strongly applied in the upper unit cell than in the lower unit cell due to the asymmetry structure. Moreover, the surface current density ($\vec{J}$) is more intense in the lower unit cells. The surface current vector drives strongly in the lower cell, and the direction of current is different being a reason for double resonance in a frequency range.
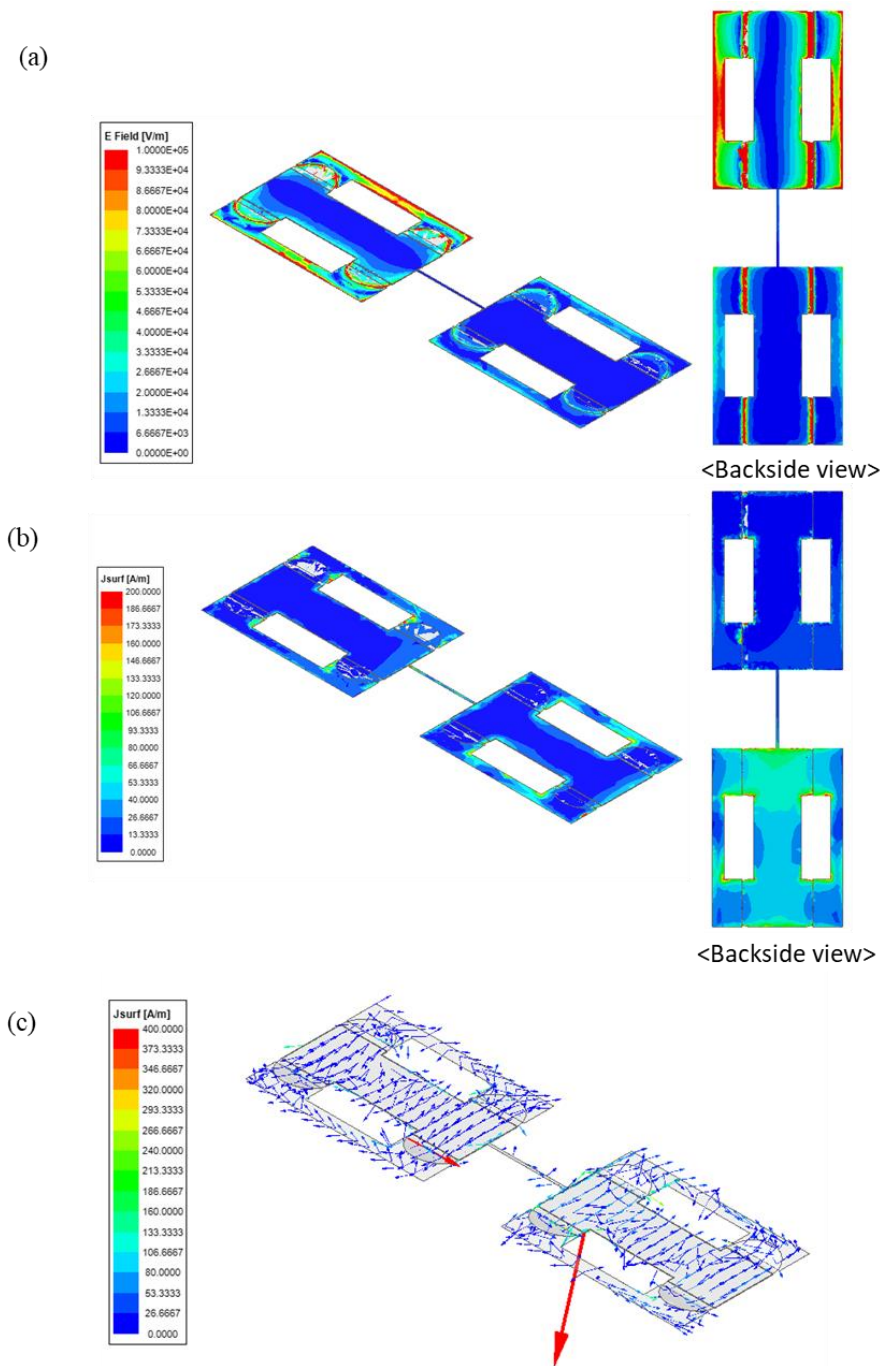
Figure 5.28. (a) $\vec{E}$-field distribution (b) Surface current density $(\vec{J})$ intensity (c) Surface current density $(\vec{J})$ vector at the reconfiguration state 2

151

5.7 Summary

5.7.1 Summary of the 1st, 2nd, and 3rd design

The characteristics of each of the 1st, 2nd, and 3rd designs are described. Table 6.1. is the summary of the 1st, 2nd, and 3rd designs in this work. All of the designs target Ka-band. All of the design share the bottom SRR form factor and function as vertical and out-of-plane actuators. These different design samples are fabricated under the same fabrication process and equipment called oxygen plasma ashing and asher 1. However, a slightly different approach is applied in the ashing recipe. The 1st design is released with 2 cycles of ashing, the 10 min ashing per cycle, and 1 day resting. The other two designs are released with an active look-up ashing process. These samples are fabricated under additional numbers of 2 min ashing per cycle to a certain amount of 5 min ashing per cycle process with the measurement results of profile condition. Moreover, the experiment on S-parameters according to the different actuating mechanisms of cantilevers is another different aspect of the three designs. The first work investigates analog tuning with different voltage states, however, the other two work is regard as digital driving, which only considers initial off and pull-in state. This strategical change is due to the unstable and narrow mechanical behavior of the curved monolayer cantilever. The micro difference in the cantilever profile clearly spawn unpredictable behavior results. Therefore, while the 2nd and the 3rd design involve 4 driving electrodes to differentiate the reconfiguration state under digital driving, the initial design only connotes a single driving electrode.

Based on this background, the first device checked the measured value by increasing the voltage step-by-step to 15 V, and the other two devices applied each pull-in voltage to the electrode step-by-step to confirm the measurement. Therefore, as shown in Table 6.1, the former is continuous tuning and the latter is discontinuous tunings. Applied pull-in voltages in the 1st, 2nd, and 3rd design are 15 V, 110 V, and 80V, respectively. The major distinctive factor defining each design is the shape of the cantilever, which dominantly affects the capacitance that determines resonance frequency. The 1st design utilizes cantilever arrays having a general shape that the width of the beam can be neglected according to the length of the beam. These arrays are the key strategy to solve the scaling-up issue. However, the cantilever shape in the 2nd design is developed by incremental etch hole spacing overcoming the non-uniformity in wide width scale cantilevers. The final evolved structure of the Ka-band MEMS tunable metamaterial absorber is the 3rd design having a semicircular cantilever with incremental etch hole spacing under time splitting ashing conditions to dramatically pull up the uniformity. Therefore, the tuning ration of the 3rd design from the initial 32.95 GHz of the resonance frequency is 4.08 GHz, overwhelming the 2.12 GHz and 2.5 GHz tuning ratio from the initial 32.21 GHz and 28 GHz of the 2nd and the initial design, respectively. Again, the key difference is described in Table 5.9.

Table 5.9. Summary of the 1st, 2nd, and 3rd design
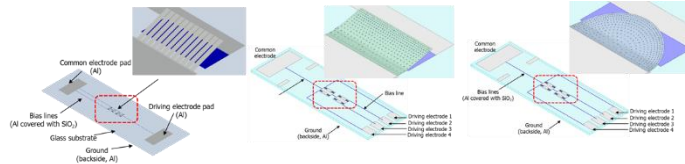
	The 1st design	The 2nd design	The 3rd design
	Ka-band	Ka-band	Ka-band
Resonance frequency (f)	$f = 28$ GHz	$f = 32.21$ GHz	$f = 32.95$ GHz
Tuning method	Mechanical tuning	Mechanical tuning	Mechanical tuning
	MEMS	MEMS	MEMS
Tuning range	$\Delta f = 2.5$ GHz	$\Delta f = 2.12$ GHz	$\Delta f = 4.08$ GHZ
Tuning ratio	$\dfrac{\Delta f}{f} = 9\%$	$\dfrac{\Delta f}{f} = 6.6\%$	$\dfrac{\Delta f}{f} = 12.29\%$
Peak absorptivity	99.95%	90.75 %	99.21%
Type of MEMS actuator	Cantilever	Cantilever	Cantilever
Number of electrodes	1 electrode in 1 cell	4 electrodes in 2 cells	4 electrodes in 2 cells
Deflection direction	Vertical, out-of-plane	Vertical, out-of-plane	Vertical, out-of-plane
Fabrication	Oxygen plasma	Oxygen plasma	Oxygen plasma
Tuning	Continuous tuning	Discontinuous tuning	Discontinuous tuning
Driving voltage	$V_d = 15$ V	$V_d = 110$ V	$V_d = 80$ V

5.7.2 Comparison with MEMS tunable metamaterial absorber

In this article, the detailed contrasting factor among MEMS tunable metamaterial absorbers would be portrayed. These works from F. Hu et al (2016), M. Liu et al(2017), and J. Xu et al(2020) [141-143] are compared to the thesis work. One common aspect of all the MEMS tunable metamaterial absorbers is the vertical deflection direction. However, only the 3rd absorber uses other types of MEMS actuator called suspended membrane while the rest of the three absorbers applied cantilever as a type of MEMS actuator. With this in consideration, the driving of the unit cell is different from each other. While, the 2nd and the 4th absorber show individual unit cell driving, the 3rd absorber works as 9 unit cells set driving and our work is more similar to unit cell element driving due to the scaling issue. Amazingly, the 4th absorber is current driving compared to voltage driving of the rest of the absorbers. The driving 1200 mA current in the 4th absorber creates thermal reconfiguration of the cantilever. Also, the driving voltage in the 3rd absorber is 250 V due to the suspended structure.

The major distinctive key aspect of this research to other absorbers is that our absorber is the only device that works in the GHz regime unlike other absorbers working in sub THz and THz regimes. Before emphasizing the interesting different points, the numerical results such as initial resonance frequency, characteristic length, unit cell dimension, tuning range, tuning ratio, and peak absorptivity are well outlined and depicted in Table 6.2. Mentioning those numbers is just the result of the research-creation.

Another difference is shown in material and fabrication. Only the 2nd

absorber used hydrofluoric wet etching to release the cantilever while other work used an oxygen plasma ashing process. Therefore, the sacrificial layer used in the 2nd absorber is phosposilicate glass instead of a polymer such as photoresist in this work or polyimide in the 3rd and the 4th absorber. All of the properties mentioned above are well described in Table 5.10.

Table 5.10. Summary of MEMS tunable metamaterial absorber
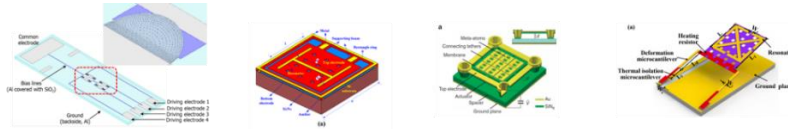
	This work	[141] F Hu *et al*, 2016	[142] M Liu et al., 2017	[143] J. Xu et al., 2020
	GHz	Sub THz regime	THz regime	THz regime
Resonance frequency (f)	$f = 32.95$ GHz	$f = 0.61$ THz	$f = 1.168$ THz	$f = 0.68$ THz
Characteristic length ($\frac{\lambda}{4}$)	$\frac{\lambda}{4} = 2.275$ mm	$\frac{\lambda}{4} = 122.75$ μm	$\frac{\lambda}{4} = 65.25$ μm	$\frac{\lambda}{4} = 110.25$ μm
Meta-atom unit cell	2×3 mm²	160×90 μm²	60×60 μm²	80×105 μm²
Type of MEMS actuator	Stress-induced cantilevers	Cantilever	Suspended membrane	Cantilever
Driving of unit cell	Unit cell element driving	Individual unit cell driving	9 unit cells set driving	Individual unit cell driving
Deflection direction	Vertical, out-of-plane	Vertical, out-of-plane	Vertical	Vertical, out-of-plane
Maximum deflection (δ,ϕ)	$\delta = 60$ μm	$\phi = 0.6°$	$\delta = 3$ μm	$\phi = 5.4°$
Fabrication	Oxygen plasma	HF wet etching	Oxygen plasma	Oxygen plasma
Sacrificial layer	Photoresist AZ4330	Phosphosilicate glass	Polyimide	Polyimide
Tuning range	$\Delta f = 4.08$ GHz	$\Delta f = 0.06$ THz	$\Delta f = 0.\,188$ THz	$\Delta f = 0.01$ THZ
Tuning ratio	$\frac{\Delta f}{f} = 12.29$ %	$\frac{\Delta f}{f} = 9$ %	$\frac{\Delta f}{f} = 16$ %	$\frac{\Delta f}{f} = 15\%$
Peak absorptivity	99.21 %	About 60 %	Up to 80 %	95.6%
Driving voltage / current	$V_d = 80$ V	$V_d = 20$ V	$V_d = 250$ V	$I = 1200$ mA

5.7.3 Comparison with Ka-band tunable metamaterial absorber

The research on Ka-band tunable metamaterial absorbers including this work will be briefly explained. The work from Q. Wang et al (2022) [144] used material tuning using nematic liquid crystal which controlled triple resonance by triple metal stripe deposition above the liquid crystal. However, this research applied MEMS solution instead of other tuning mechanisms. The former Ka-band tunable metamaterial absorber showed a tuning ratio of 9.5, 9.1, 8.58% from an initial 25.4, 28.7, and 32.8 GHz under DC bias 5 V of liquid crystal transition compared to the 12.29 % tuning ratio in this work. Therefore, the tuning ratio is slightly higher in this research work. To resume, each tuning approach has both advantages and disadvantages. Even though, the former has strengths such as low loss of nematic liquid crystal, mature fabrication process, and relatively large tuning ratio, the temperature constraints, and continuous power consumption are drawbacks of the absorber reliability. In contrast to the former research, the absorber in this thesis shows a relatively large tuning ratio and consumes less power, However, the tuning speed and reliability are the major flaw. The Table 5.11 clarifies each characteristic of tunable metamaterial absorbers in Ka-band.

Table 5.11. Summary on Ka-band tunable metamaterial absorber
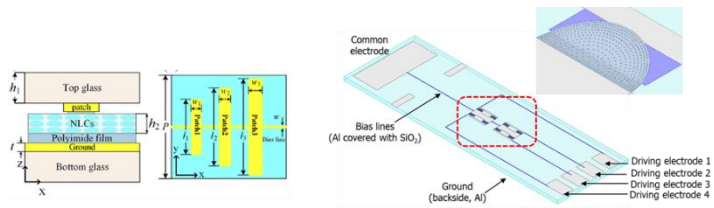
	[144] Q. Wang *et al*, 2022	This work
	Ka-band	Ka-band
Resonance frequency (f)	$f_1 = 25.4$ GHz, $f_2 = 28.7$ GHz, $f_3 = 32.8$ GHz	$f = 32.95$ GHz
Tuning method	Material tuning Liquid crystal	Mechanical tuning MEMS cantilever
Tuning range		$\Delta f = 4.08$ GHz
Tuning ratio	$\dfrac{\Delta f}{f} = 9.5\%, 9.1\%, 8.58\%$	$\dfrac{\Delta f}{f} = 12.29$ %
Peak absorptivity	Up to about 95%	99.21%
Driving voltage	DC bias $V_d = 5$ V	Electrostatic $V_d = 80$ V
Advantages	Low loss of nematic liquid crystal Mature fabrication of liquid crystal Relatively large tuning range	Relatively large tuning range Low energy consumption for pull-in
Disadvantages	Temperature sensitivity of the effective permittivity of nematic liquid crystal Continuous dc bias	Low tuning speed

CHAPTER 6. Conclusion

MEMS solution is first proposed and demonstrated to realize frequency tunable metamaterial absorber for Ka band. To achieve resonance frequency tunability with mechanical reconfiguration, sub-mm scale stress-induced MEMS cantilever having initial out-of-plane deflection is applied as an electrostatically actuating element in the metamaterial unit cell to generate capacitance change. The absorber consists of two split ring resonator structure in which the four cantilever beams with stress gradient is aligned symmetrically with pairs. Determination of the dimensional parameters are realized based on the impedance matching simulation of full electromagnetic wave.

The fabrication of the absorber is entirely performed by surface micromachining with metallic film and photoresist based sacrificial layer on the glass wafer. Oxygen plasma ashing process is selected as a releasing method for realizing cantilever with large deflection. To ramp up the uniformity and reproducibility of sub-mm scale stress-induced cantilevers in absorber, condition of ashing process is thoroughly controlled with cyclic processing and various beam structure is attempted during engineering. Three different beam design from cantilever array type to finally evolved semicircular beam type are proposed and measured as an appropriate shape for applying to absorber.

First of all, the absorber continuously actuated with stress-induced cantilever array structure. The fabricated total 96 cantilevers showed average 41.5 μm deflection. The absorber initially resonated in 28 GHz and gradually shifted to

25.5 GHz showing 2.5 GHz of tuning range when the voltage is applied up to 15 V. The peak absorptivity shift from 72.9 % of initial off-state to 99.9 % of pull-in state.

The 2nd design absorber having sub-mm scale rectangular cantilevers with incremental etch hole pattern reconfigures digitally in 5 different states. From initial state to all pull down state, the absorber performance show 2.14 GHz of tuning. The resonance frequency changes from 32.14 to 30.10 GHz. The peak absorptivity at resonance frequency undergoes 83.58 % to 90.75 %. Even though the releasing of cantilevers has improved, the performance of metamaterial absorber has not been fully achieved due to the abnormal mechanical behavior of electrostatically driven cantilevers.

The semicircular beam with an incremental etch hole showed the most improved uniformity results. The fabrication result of the 3rd design absorber constantly shows reproducibility of releasing sub-mm scale cantilever. Analyzing 144 cantilevers from total 18 samples, the average of the average maximum end tip deflection is 51.8 μm and the standard deviation of the average maximum end tip deflection is 3.1 μm. The performance of the fabricated absorber is experimentally validated with a rectangular waveguide measurement setup. Through undergoing different reconfiguration state from initial off-state to all pulled-down state, the absorption frequency range is measured as 4.08 GHz with 12.9% of tunability when applying DC 80 V bias in each electrode. The resonance frequency shift from 32.95 to 28.87 GHz. The reflection coefficient at each stage exceeds over -9 dB, the transmission coefficient is lower than -39 dB at each state, and the peak absorptivity at each state show over 80%. The measured peak absorption rates at each state are 80.95 %, 88.17 %, 86.29 %, 99.21 %, and 86.51%, at each state respectively.

Bibliography

[1] T. J. Cui, D. R. Smith, and R. Liu, *Metamaterials: Theory, Design, and Applications*. 2010, pp. 1-367.

[2] I. A. Buriak, V. O. Zhurba, G. S. Vorobjov, V. R. Kulizhko, O. K. Kononov, and O. Rybalko, "Metamaterials: Theory, Classification and Application Strategies (Review)," *Journal of Nano- and Electronic Physics,* vol. 8, no. 4(2), pp. 04088-1-04088-11, 2016, doi: 10.21272/jnep.8(4(2)).04088.

[3] R. A. Shelby, D. R. Smith, S. C. Nemat-Nasser, and S. Schultz, "Microwave transmission through a two-dimensional, isotropic, left-handed metamaterial," *Applied Physics Letters,* vol. 78, no. 4, pp. 489-491, 2001, doi: 10.1063/1.1343489.

[4] A. K. Azad, A. V. Efimov, S. Ghosh, J. Singleton, A. J. Taylor, and H. T. Chen, "Ultra-thin metasurface microwave flat lens for broadband applications," *Appl Phys Lett,* vol. 110, no. 22, p. 224101, May 29 2017, doi: 10.1063/1.4984219.

[5] P. Moitra, B. A. Slovick, Z. Gang Yu, S. Krishnamurthy, and J. Valentine, "Experimental demonstration of a broadband all-dielectric metamaterial perfect reflector," *Applied Physics Letters,* vol. 104, no. 17, 2014, doi: 10.1063/1.4873521.

[6] D. Schurig *et al.*, "Metamaterial Electromagnetic Cloak at Microwave Frequencies," *Science,* vol. 314, no. 5801, pp. 977-980, 2006, doi: doi:10.1126/science.1133628.

[7] M. Thiel, M. S. Rill, G. von Freymann, and M. Wegener, "Three-Dimensional Bi-Chiral Photonic Crystals," *Advanced Materials,* pp. NA-NA, 2009, doi: 10.1002/adma.200901601.

[8] D. Chanda *et al.*, "Large-area flexible 3D optical negative index metamaterial formed by nanotransfer printing," *Nat Nanotechnol,* vol. 6, no. 7, pp. 402-7, Jun 5 2011, doi: 10.1038/nnano.2011.82.

[9]   N. Fang *et al.*, "Ultrasonic metamaterials with negative modulus," *Nat Mater,* vol. 5, no. 6, pp. 452-6, Jun 2006, doi: 10.1038/nmat1644.

[10]   W. T. Chen *et al.*, "A broadband achromatic metalens for focusing and imaging in the visible," *Nat Nanotechnol,* vol. 13, no. 3, pp. 220-226, Mar 2018, doi: 10.1038/s41565-017-0034-6.

[11]   S. Wang *et al.*, "A broadband achromatic metalens in the visible," *Nat Nanotechnol,* vol. 13, no. 3, pp. 227-232, Mar 2018, doi: 10.1038/s41565-017-0052-4.

[12]   K. Chen *et al.*, "A Reconfigurable Active Huygens' Metalens," *Adv Mater,* vol. 29, no. 17, May 2017, doi: 10.1002/adma.201606422.

[13]   X. Chen *et al.*, "Dual-polarity plasmonic metalens for visible light," *Nat Commun,* vol. 3, p. 1198, 2012, doi: 10.1038/ncomms2207.

[14]   M. Choi *et al.*, "A terahertz metamaterial with unnaturally high refractive index," *Nature,* vol. 470, no. 7334, pp. 369-73, Feb 17 2011, doi: 10.1038/nature09776.

[15]   J. Gu *et al.*, "Active control of electromagnetically induced transparency analogue in terahertz metamaterials," *Nat Commun,* vol. 3, p. 1151, 2012, doi: 10.1038/ncomms2153.

[16]   S.-Y. Chiam, R. Singh, C. Rockstuhl, F. Lederer, W. Zhang, and A. A. Bettiol, "Analogue of electromagnetically induced transparency in a terahertz metamaterial," *Physical Review B,* vol. 80, no. 15, 2009, doi: 10.1103/PhysRevB.80.153103.

[17]   P. Tassin, L. Zhang, T. Koschny, E. N. Economou, and C. M. Soukoulis, "Low-loss metamaterials based on classical electromagnetically induced transparency," *Phys Rev Lett,* vol. 102, no. 5, p. 053901, Feb 6 2009, doi: 10.1103/PhysRevLett.102.053901.

[18]   B. Wang, J. Zhou, T. Koschny, M. Kafesaki, and C. M. Soukoulis, "Chiral metamaterials: simulations and experiments," *Journal of Optics A: Pure and Applied Optics,* vol. 11, no. 11, 2009, doi: 10.1088/1464-4258/11/11/114003.

[19]   Y. Zhao, A. N. Askarpour, L. Sun, J. Shi, X. Li, and A. Alu, "Chirality detection of enantiomers using twisted optical metamaterials," *Nat Commun,* vol. 8, p. 14180, Jan 25 2017, doi: 10.1038/ncomms14180.

[20]   W. Ma, F. Cheng, and Y. Liu, "Deep-Learning-Enabled On-Demand Design of Chiral Metamaterials," *ACS Nano,* vol. 12, no. 6, pp. 6326-6334, Jun 26 2018, doi: 10.1021/acsnano.8b03569.

[21]   W. Panpradit, A. Sonsilphong, C. Soemphol, and N. Wongkasem, "High negative refractive index in chiral metamaterials," *Journal of Optics,* vol. 14, no. 7, 2012, doi: 10.1088/2040-8978/14/7/075101.

[22]   B. Wang, J. Zhou, T. Koschny, and C. M. Soukoulis, "Nonplanar chiral metamaterials with negative index," *Applied Physics Letters,* vol. 94, no. 15, 2009, doi: 10.1063/1.3120565.

[23]   S. Xiao *et al.*, "Loss-free and active optical negative-index metamaterials," *Nature,* vol. 466, no. 7307, pp. 735-8, Aug 5 2010, doi: 10.1038/nature09278.

[24]   D. R. Smith, W. J. Padilla, D. C. Vier, S. C. Nemat-Nasser, and S. Schultz, "Composite Medium with Simultaneously Negative Permeability and Permittivity," *Physical Review Letters,* vol. 84, no. 18, pp. 4184-4187, 05/01/ 2000, doi: 10.1103/PhysRevLett.84.4184.

[25]   M. Ren *et al.*, "Nanostructured plasmonic medium for terahertz bandwidth all-optical switching," *Adv Mater,* vol. 23, no. 46, pp. 5540-4, Dec 8 2011, doi: 10.1002/adma.201103162.

[26]   K. M. Dani, Z. Ku, P. C. Upadhya, R. P. Prasankumar, S. R. J. Brueck, and A. J. Taylor, "Subpicosecond Optical Switching with a Negative Index Metamaterial," *Nano Letters,* vol. 9, no. 10, pp. 3565-3569, 2009/10/14 2009, doi: 10.1021/nl9017644.

[27]   S. Zhu, D. G. Holtby, K. L. Ford, A. Tennant, and R. J. Langley, "Compact Low Frequency Varactor Loaded Tunable SRR Antenna," *IEEE Transactions on*

Antennas and Propagation, vol. 61, no. 4, pp. 2301-2304, 2013, doi: 10.1109/tap.2013.2239952.

[28]   N. Vasilantonakis, M. E. Nasir, W. Dickson, G. A. Wurtz, and A. V. Zayats, "Bulk plasmon-polaritons in hyperbolic nanorod metamaterial waveguides," *Laser Photon Rev,* vol. 9, no. 3, pp. 345-353, May 2015, doi: 10.1002/lpor.201400457.

[29]   N. Liu, M. Mesch, T. Weiss, M. Hentschel, and H. Giessen, "Infrared perfect absorber and its application as plasmonic sensor," *Nano Lett,* vol. 10, no. 7, pp. 2342-8, Jul 14 2010, doi: 10.1021/nl9041033.

[30]   N. I. Landy, S. Sajuyigbe, J. J. Mock, D. R. Smith, and W. J. Padilla, "Perfect metamaterial absorber," *Phys Rev Lett,* vol. 100, no. 20, p. 207402, May 23 2008, doi: 10.1103/PhysRevLett.100.207402.

[31]   N. Sang-Nourpour, B. Lavoie, R. Kheradmand, M. Rezaei Keramati, and B. Sanders, "Electromagnetic-Magnetoelectric Duality for Waveguides," *arXiv:1510.06458v1,* 10/21 2015.

[32]   A. Forouzmand, C. S. R. Kaipa, and A. B. Yakovlev, "Mushroom-type structures with the wires connected through diodes: Theory and applications," *Journal of Applied Physics,* vol. 120, no. 1, 2016, doi: 10.1063/1.4954676.

[33]   F. Bayatpur and K. Sarabandi, "A Tunable Metamaterial Frequency-Selective Surface With Variable Modes of Operation," *IEEE Transactions on Microwave Theory and Techniques,* vol. 57, no. 6, pp. 1433-1438, 2009, doi: 10.1109/tmtt.2009.2020841.

[34]   J. Y. Ou, E. Plum, J. Zhang, and N. I. Zheludev, "An electromechanically reconfigurable plasmonic metamaterial operating in the near-infrared," *Nat Nanotechnol,* vol. 8, no. 4, pp. 252-5, Apr 2013, doi: 10.1038/nnano.2013.25.

[35]   J. A. Bossard *et al.*, "Tunable Frequency Selective Surfaces and Negative-Zero-Positive Index Metamaterials Based on Liquid Crystals," *IEEE Transactions on Antennas and Propagation,* vol. 56, no. 5, pp. 1308-1320, 2008, doi:

10.1109/tap.2008.922174.

[36]   M. Hudlicka and M. J., "TRIPLE WIRE MEDIUM AS AN ISOTROPIC NEGATIVE PERMITTIVITY METAMATERIAL Triple wire medium as an isotropic negative permittivity metamaterial," *Progress In Electromagnetics Research,* vol. 65, p. 14, 2006.

[37]   J. D. Baena, R. Marqués, F. Medina, and J. Martel, "Artificial magnetic metamaterial design by using spiral resonators," *Physical Review B,* vol. 69, no. 1, 2004, doi: 10.1103/PhysRevB.69.014402.

[38]   S. Komeylian and F. Mohammadi, "Conical Swiss Roll Metamaterial Application for Slow-Light Waveguides," *Canadian Journal of Electrical and Computer Engineering,* vol. 43, no. 3, pp. 163-169, 2020, doi: 10.1109/cjece.2020.2969644.

[39]   S. Maslovski, P. Ikonen, I. Kolmakov, and S. Tretyakov, "Artificial magnetic materials based on the new magnetic particle Metasolenoid," *Progress In Electromagnetics Research,* vol. 54, p. 21, 2005.

[40]   H. Chen *et al.*, "Left-handed materials composed of only S-shaped resonators," *Phys Rev E Stat Nonlin Soft Matter Phys,* vol. 70, no. 5 Pt 2, p. 057605, Nov 2004, doi: 10.1103/PhysRevE.70.057605.

[41]   K. Matra and N. Wongkasem, "Left-handed chiral isotropic metamaterials: analysis and detailed numerical study," *Journal of Optics A: Pure and Applied Optics,* vol. 11, no. 7, 2009, doi: 10.1088/1464-4258/11/7/074011.

[42]   C. Sabah and H. G. Roskos, "Terahertz sensing application by using planar split-ring-resonator structures," *Microsystem Technologies,* vol. 18, no. 12, pp. 2071-2076, 2012, doi: 10.1007/s00542-012-1559-0.

[43]   W. Zhang *et al.*, "Micromachined switchable metamaterial with dual resonance," *Applied Physics Letters,* vol. 101, no. 15, 2012, doi: 10.1063/1.4759029.

[44]   S. K. Patel and C. Argyropoulos, "Enhanced bandwidth and gain of compact microstrip antennas loaded with multiple corrugated split ring resonators," *Journal*

of Electromagnetic Waves and Applications, vol. 30, no. 7, pp. 945-961, 2016, doi: 10.1080/09205071.2016.1167633.

[45]   E. Ekmekci, K. Topalli, T. Akin, and G. Turhan-Sayan, "A tunable multi-band metamaterial design using micro-split SRR structures," *Opt. Express,* vol. 17, no. 18, pp. 16046-16058, 2009/08/31 2009, doi: 10.1364/OE.17.016046.

[46]   A. X. Lalas, N. V. Kantartzis, and T. D. Tsiboukis, "Reconfigurable metamaterial components exploiting two-hot-arm electrothermal actuators," *Microsystem Technologies,* vol. 21, no. 10, pp. 2097-2107, 2015, doi: 10.1007/s00542-015-2407-9.

[47]   X. He, Z. Lv, B. Liu, and Z. Li, "Tunable magnetic metamaterial based multi-split-ring resonator (MSRR) using MEMS switch components," *Microsystem Technologies,* vol. 17, no. 8, pp. 1263-1269, 2011, doi: 10.1007/s00542-011-1313-z.

[48]   Y. S. Lin, F. Ma, and C. Lee, "Three-dimensional movable metamaterial using electric split-ring resonators," *Opt Lett,* vol. 38, no. 16, pp. 3126-8, Aug 15 2013, doi: 10.1364/OL.38.003126.

[49]   J. Naqui, J. Coromina, F. Martín, A. K. Horestani, and C. Fumeaux, "Comparative analysis of split ring resonators (SRR), electric-LC (ELC) resonators, and S-shaped split ring resonators (S-SRR): Potential application to rotation sensors," in *Proceedings of 2014 Mediterranean Microwave Symposium (MMS2014)*, 12-14 Dec. 2014 2014, pp. 1-5, doi: 10.1109/MMS.2014.7088931.

[50]   R. Basiry, H. Abiri, and A. Yahaghi, "Electromagnetic performance analysis of omega-type metamaterial radomes," *International Journal of RF and Microwave Computer-Aided Engineering,* vol. 21, no. 6, pp. 665-673, 2011, doi: 10.1002/mmce.20562.

[51]   F. Zhang, G. Houzet, E. Lheurette, D. Lippens, M. Chaubet, and X. Zhao, "Negative-zero-positive metamaterial with omega-type metal inclusions," *Journal*

of Applied Physics, vol. 103, no. 8, 2008, doi: 10.1063/1.2910831.

[52]   F. Dincer, M. Karaaslan, E. Unal, and C. Sabah, "Dual-band polarization independent metamaterial absorber based on omega resoanator and octa-star strip configuration," *Progress In Electromagnetics Research,* vol. 141, p. 13, 2013.

[53]   C. M. Watts, X. Liu, and W. J. Padilla, "Metamaterial electromagnetic wave absorbers," *Adv Mater,* vol. 24, no. 23, pp. OP98-120, OP181, Jun 19 2012, doi: 10.1002/adma.201200674.

[54]   S. A. Tretyakov and S. I. Maslovski, "Thin absorbing structure for all incidence angles based on the use of a high-impedance surface," *Microwave and Optical Technology Letters,* vol. 38, no. 3, pp. 175-178, 2003, doi: 10.1002/mop.11006.

[55]   F. Bilotti, L. Nucci, and L. Vegni, "An SRR based microwave absorber," *Microwave and Optical Technology Letters,* vol. 48, no. 11, pp. 2171-2175, 2006, doi: 10.1002/mop.21891.

[56]   H. Li, L. H. Yuan, B. Zhou, X. P. Shen, Q. Cheng, and T. J. Cui, "Ultrathin multiband gigahertz metamaterial absorbers," *Journal of Applied Physics,* vol. 110, no. 1, 2011, doi: 10.1063/1.3608246.

[57]   L. Li, Y. Yang, and C. Liang, "A wide-angle polarization-insensitive ultra-thin metamaterial absorber with three resonant modes," *Journal of Applied Physics,* vol. 110, no. 6, 2011, doi: 10.1063/1.3638118.

[58]   Y. Cheng, H. Yang, Z. Cheng, and N. Wu, "Perfect metamaterial absorber based on a split-ring-cross resonator," *Applied Physics A,* vol. 102, no. 1, pp. 99-103, 2010, doi: 10.1007/s00339-010-6022-4.

[59]   I. Puscasu and W. L. Schaich, "Narrow-band, tunable infrared emission from arrays of microstrip patches," *Applied Physics Letters,* vol. 92, no. 23, 2008, doi: 10.1063/1.2938716.

[60]   X. Liu, T. Tyler, T. Starr, A. F. Starr, N. M. Jokerst, and W. J. Padilla, "Taming the blackbody with infrared metamaterials as selective thermal emitters," *Phys Rev Lett,*

167

vol. 107, no. 4, p. 045901, Jul 22 2011, doi: 10.1103/PhysRevLett.107.045901.

[61]   T. Maier and H. Brückl, "Wavelength-tunable microbolometers with metamaterial absorbers," *Opt. Lett.,* vol. 34, no. 19, pp. 3012-3014, 2009/10/01 2009, doi: 10.1364/OL.34.003012.

[62]   T. Maier and H. Brueckl, "Multispectral microbolometers for the midinfrared," *Opt. Lett.,* vol. 35, no. 22, pp. 3766-3768, 2010/11/15 2010, doi: 10.1364/OL.35.003766.

[63]   P. K. Singh, K. A. Korolev, M. N. Afsar, and S. Sonkusale, "Single and dual band 77/95/110 GHz metamaterial absorbers on flexible polyimide substrate," *Applied Physics Letters,* vol. 99, no. 26, 2011, doi: 10.1063/1.3672100.

[64]   Z. Yin *et al.*, "Electrically tunable terahertz dual-band metamaterial absorber based on a liquid crystal," *RSC Advances,* vol. 8, no. 8, pp. 4197-4203, 2018, doi: 10.1039/c7ra13047c.

[65]   F. Zhang, Q. Zhao, W. Zhang, J. Sun, J. Zhou, and D. Lippens, "Voltage tunable short wire-pair type of metamaterial infiltrated by nematic liquid crystal," *Applied Physics Letters,* vol. 97, no. 13, 2010, doi: 10.1063/1.3496034.

[66]   X. Wang, D.-H. Kwon, D. H. Werner, I.-C. Khoo, A. V. Kildishev, and V. M. Shalaev, "Tunable optical negative-index metamaterials employing anisotropic liquid crystals," *Applied Physics Letters,* vol. 91, no. 14, 2007, doi: 10.1063/1.2795345.

[67]   H. Yan *et al.*, "Tunable infrared plasmonic devices using graphene/insulator stacks," *Nat Nanotechnol,* vol. 7, no. 5, pp. 330-4, Apr 22 2012, doi: 10.1038/nnano.2012.59.

[68]   A. E. Nikolaenko *et al.*, "Nonlinear graphene metamaterial," *Applied Physics Letters,* vol. 100, no. 18, 2012, doi: 10.1063/1.4711044.

[69]   L. Ju *et al.*, "Graphene plasmonics for tunable terahertz metamaterials," *Nat Nanotechnol,* vol. 6, no. 10, pp. 630-4, Sep 4 2011, doi: 10.1038/nnano.2011.146.

[70]   M. Gil *et al.*, "Electrically tunable split-ring resonators at microwave frequencies based on barium-strontium-titanate thick films," *Electronics Letters,* vol. 45, no. 8, 2009, doi: 10.1049/el.2009.3055.

[71] L. Kang, Q. Zhao, H. Zhao, and J. Zhou, "Magnetically tunable negative permeability metamaterial composed by split ring resonators and ferrite rods," *Opt. Express,* vol. 16, no. 12, pp. 8825-8834, 2008/06/09 2008, doi: 10.1364/OE.16.008825.

[72] M. K. Hedayati *et al.*, "Photo-driven Super Absorber as an Active Metamaterial with a Tunable Molecular-Plasmonic Coupling," *Advanced Optical Materials,* vol. 2, no. 8, pp. 705-710, 2014, doi: 10.1002/adom.201400105.

[73] M. Masyukov, A. Vozianova, A. Grebenchukov, K. Gubaidullina, A. Zaitsev, and M. Khodzitsky, "Optically tunable terahertz chiral metasurface based on multi-layered graphene," *Sci Rep,* vol. 10, no. 1, p. 3157, Feb 21 2020, doi: 10.1038/s41598-020-60097-0.

[74] H.-T. Chen *et al.*, "Experimental demonstration of frequency-agile terahertz metamaterials," *Nature Photonics,* vol. 2, no. 5, pp. 295-298, 2008, doi: 10.1038/nphoton.2008.52.

[75] M. Seo *et al.*, "Active terahertz nanoantennas based on VO2 phase transition," *Nano Lett,* vol. 10, no. 6, pp. 2064-8, Jun 9 2010, doi: 10.1021/nl1002153.

[76] M. D. Goldflam *et al.*, "Reconfigurable gradient index using VO2 memory metamaterials," *Applied Physics Letters,* vol. 99, no. 4, 2011, doi: 10.1063/1.3615804.

[77] K. Appavoo and R. F. Haglund, "Detecting nanoscale size dependence in VO2 phase transition using a split-ring resonator metamaterial," *Nano Lett,* vol. 11, no. 3, pp. 1025-31, Mar 9 2011, doi: 10.1021/nl103842v.

[78] T. Driscoll *et al.*, "Dynamic tuning of an infrared hybrid-metamaterial resonance using vanadium dioxide," *Applied Physics Letters,* vol. 93, no. 2, 2008, doi: 10.1063/1.2956675.

[79] A. V. Krasavin, K. F. MacDonald, A. S. Schwanecke, and N. I. Zheludev, "Gallium/aluminum nanocomposite material for nonlinear optics and nonlinear

plasmonics," *Applied Physics Letters,* vol. 89, no. 3, 2006, doi: 10.1063/1.2234276.

[80]   H. Jeong, J. H. Park, Y. H. Moon, C. W. Baek, and S. Lim, "Thermal Frequency Reconfigurable Electromagnetic Absorber Using Phase Change Material," *Sensors (Basel),* vol. 18, no. 10, Oct 17 2018, doi: 10.3390/s18103506.

[81]   W. Xu and S. Sonkusale, "Microwave diode switchable metamaterial reflector/absorber," *Applied Physics Letters,* vol. 103, no. 3, 2013, doi: 10.1063/1.4813750.

[82]   J. Fang, J. Huang, Y. Gou, and Y. Shang, "Research on broadband tunable metamaterial absorber based on PIN diode," *Optik,* vol. 200, 2020, doi: 10.1016/j.ijleo.2019.163171.

[83]   X. Wu *et al.*, "Active microwave absorber with the dual-ability of dividable modulation in absorbing intensity and frequency," *AIP Advances,* vol. 3, no. 2, 2013, doi: 10.1063/1.4792069.

[84]   T. Wu, W. Li, S. Chen, and J. Guan, "Wideband frequency tunable metamaterial absorber by splicing multiple tuning ranges," *Results in Physics,* vol. 20, 2021, doi: 10.1016/j.rinp.2020.103753.

[85]   H. Jeong, T. T. Nguyen, and S. Lim, "Subwavelength Metamaterial Unit Cell for Low-Frequency Electromagnetic Absorber Applications," *Sci Rep,* vol. 8, no. 1, p. 16774, Nov 13 2018, doi: 10.1038/s41598-018-35267-w.

[86]   S. Ghosh and K. V. Srivastava, "Polarization-Insensitive Single-/Dual-Band Tunable Absorber With Independent Tuning in Wide Frequency Range," *IEEE Transactions on Antennas and Propagation,* vol. 65, no. 9, pp. 4903-4908, 2017, doi: 10.1109/tap.2017.2731381.

[87]   S. Hrabar, I. Krois, I. Bonic, and A. Kiricenko, "Negative capacitor paves the way to ultra-broadband metamaterials," *Applied Physics Letters,* vol. 99, no. 25, 2011, doi: 10.1063/1.3671366.

[88]   K. Z. Rajab, Y. Hao, D. Bao, C. G. Parini, J. Vazquez, and M. Philippakis, "Stability

of active magnetoinductive metamaterials," *Journal of Applied Physics,* vol. 108, no. 5, 2010, doi: 10.1063/1.3476464.

[89]   D. Shrekenhamer *et al.*, "High speed terahertz modulation from metamaterials with embedded high electron mobility transistors," *Opt. Express,* vol. 19, no. 10, pp. 9968-9975, 2011/05/09 2011, doi: 10.1364/OE.19.009968.

[90]   E. Feigenbaum, K. Diest, and H. A. Atwater, "Unity-order index change in transparent conducting oxides at visible frequencies," *Nano Lett,* vol. 10, no. 6, pp. 2111-6, Jun 9 2010, doi: 10.1021/nl1006307.

[91]   K. A. Boulais *et al.*, "Tunable split-ring resonator for metamaterials using photocapacitance of semi-insulating GaAs," *Applied Physics Letters,* vol. 93, no. 4, 2008, doi: 10.1063/1.2967192.

[92]   J. Han and A. Lakhtakia, "Semiconductor split-ring resonators for thermally tunable terahertz metamaterials," *Journal of Modern Optics,* vol. 56, no. 4, pp. 554-557, 2009, doi: 10.1080/09500340802621785.

[93]   D. Roy Chowdhury, R. Singh, J. F. O'Hara, H.-T. Chen, A. J. Taylor, and A. K. Azad, "Dynamically reconfigurable terahertz metamaterial through photo-doped semiconductor," *Applied Physics Letters,* vol. 99, no. 23, 2011, doi: 10.1063/1.3667197.

[94]   A. Pimenov, A. Loidl, P. Przyslupski, and B. Dabrowski, "Negative refraction in ferromagnet-superconductor superlattices," *Phys Rev Lett,* vol. 95, no. 24, p. 247009, Dec 9 2005, doi: 10.1103/PhysRevLett.95.247009.

[95]   M. Ricci, N. Orloff, and S. M. Anlage, "Superconducting metamaterials," *Applied Physics Letters,* vol. 87, no. 3, 2005, doi: 10.1063/1.1996844.

[96]   C. Kurter, A. P. Zhuravel, J. Abrahams, C. L. Bennett, A. V. Ustinov, and S. M. Anlage, "Superconducting RF Metamaterials Made With Magnetically Active Planar Spirals," *IEEE Transactions on Applied Superconductivity,* vol. 21, no. 3, pp. 709-712, 2011, doi: 10.1109/tasc.2010.2088093.

[97]   A. B. Golovin and O. D. Lavrentovich, "Electrically reconfigurable optical metamaterial based on colloidal dispersion of metal nanorods in dielectric fluid," *Applied Physics Letters,* vol. 95, no. 25, 2009, doi: 10.1063/1.3278442.

[98]   Q. Liu, Y. Cui, D. Gardner, X. Li, S. He, and Smalyukh, II, "Self-alignment of plasmonic gold nanorods in reconfigurable anisotropic fluids for tunable bulk metamaterial applications," *Nano Lett,* vol. 10, no. 4, pp. 1347-53, Apr 14 2010, doi: 10.1021/nl9042104.

[99]   K. Fuchi, A. R. Diaz, E. J. Rothwell, R. O. Ouedraogo, and J. Tang, "An origami tunable metamaterial," *Journal of Applied Physics,* vol. 111, no. 8, 2012, doi: 10.1063/1.4704375.

[100]   Z. Wang *et al.*, "Origami-Based Reconfigurable Metamaterials for Tunable Chirality," *Adv Mater,* vol. 29, no. 27, Jul 2017, doi: 10.1002/adma.201700412.

[101]   I. M. Pryce, K. Aydin, Y. A. Kelaita, R. M. Briggs, and H. A. Atwater, "Highly strained compliant optical metamaterials with large frequency tunability," *Nano Lett,* vol. 10, no. 10, pp. 4222-7, Oct 13 2010, doi: 10.1021/nl102684x.

[102]   H. Tao *et al.*, "Metamaterial silk composites at terahertz frequencies," *Adv Mater,* vol. 22, no. 32, pp. 3527-31, Aug 24 2010, doi: 10.1002/adma.201000412.

[103]   J. Y. Ou, E. Plum, L. Jiang, and N. I. Zheludev, "Reconfigurable photonic metamaterials," *Nano Lett,* vol. 11, no. 5, pp. 2142-4, May 11 2011, doi: 10.1021/nl200791r.

[104]   H. Jeong, D. H. Le, D. Lim, R. Phon, and S. Lim, "Reconfigurable Metasurfaces for Frequency Selective Absorption," *Advanced Optical Materials,* vol. 8, no. 13, 2020, doi: 10.1002/adom.201902182.

[105]   P. Pitchappa, C. P. Ho, L. Dhakar, and C. Lee, "Microelectromechanically reconfigurable interpixelated metamaterial for independent tuning of multiple resonances at terahertz spectral region," *Optica,* vol. 2, no. 6, 2015, doi: 10.1364/optica.2.000571.

[106] P. Pitchappa *et al.*, "Micro-electro-mechanically tunable metamaterial with enhanced electro-optic performance," *Applied Physics Letters,* vol. 104, no. 15, 2014, doi: 10.1063/1.4871517.

[107] P. Pitchappa, C. P. Ho, Y. Qian, L. Dhakar, N. Singh, and C. Lee, "Microelectromechanically tunable multiband metamaterial with preserved isotropy," *Sci Rep,* vol. 5, p. 11678, Jun 26 2015, doi: 10.1038/srep11678.

[108] P. Pitchappa, C. P. Ho, L. Cong, R. Singh, N. Singh, and C. Lee, "Reconfigurable Digital Metamaterial for Dynamic Switching of Terahertz Anisotropy," *Advanced Optical Materials,* vol. 4, no. 3, pp. 391-398, 2016, doi: 10.1002/adom.201500588.

[109] Y.-S. Lin, Y. Qian, F. Ma, Z. Liu, P. Kropelnicki, and C. Lee, "Development of stress-induced curved actuators for a tunable THz filter based on double split-ring resonators," *Applied Physics Letters,* vol. 102, no. 11, 2013, doi: 10.1063/1.4798244.

[110] L. Yu-Sheng, H. Chia-Yi, and L. Chengkuo, "Reconfiguration of Resonance Characteristics for Terahertz U-Shape Metamaterial Using MEMS Mechanism," *IEEE Journal of Selected Topics in Quantum Electronics,* vol. 21, no. 4, pp. 93-99, 2015, doi: 10.1109/jstqe.2014.2361840.

[111] Y.-S. Lin and C. Lee, "Tuning characteristics of mirrorlike T-shape terahertz metamaterial using out-of-plane actuated cantilevers," *Applied Physics Letters,* vol. 104, no. 25, 2014, doi: 10.1063/1.4885839.

[112] F. Ma, Y.-S. Lin, X. Zhang, and C. Lee, "Tunable multiband terahertz metamaterials using a reconfigurable electric split-ring resonator array," *Light: Science & Applications,* vol. 3, no. 5, pp. e171-e171, 2014, doi: 10.1038/lsa.2014.52.

[113] M. Manjappa *et al.*, "Reconfigurable MEMS Fano metasurfaces with multiple-input-output states for logic operations at terahertz frequencies," *Nat Commun,* vol. 9, no. 1, p. 4056, Oct 3 2018, doi: 10.1038/s41467-018-06360-5.

[114] F. Ma *et al.*, "Polarization-sensitive microelectromechanical systems based tunable terahertz metamaterials using three dimensional electric split-ring resonator arrays,"

Applied Physics Letters, vol. 102, no. 16, 2013, doi: 10.1063/1.4803048.

[115]   C. P. Ho, P. Pitchappa, and C. Lee, "Digitally reconfigurable binary coded terahertz metamaterial with output analogous to NOR and AND," *Journal of Applied Physics,* vol. 119, no. 15, 2016, doi: 10.1063/1.4946891.

[116]   P. Pitchappa, C. P. Ho, L. Dhakar, Y. Qian, N. Singh, and C. Lee, "Periodic Array of Subwavelength MEMS Cantilevers for Dynamic Manipulation of Terahertz Waves," *Journal of Microelectromechanical Systems,* vol. 24, no. 3, pp. 525-527, 2015, doi: 10.1109/jmems.2015.2421307.

[117]   K. Shih *et al.*, "Active MEMS metamaterials for THz bandwidth control," *Applied Physics Letters,* vol. 110, no. 16, 2017, doi: 10.1063/1.4980115.

[118]   X. Zhao *et al.*, "Electromechanically tunable metasurface transmission waveplate at terahertz frequencies," *Optica,* vol. 5, no. 3, 2018, doi: 10.1364/optica.5.000303.

[119]   P. Pitchappa *et al.*, "Active control of near-field coupling in conductively coupled microelectromechanical system metamaterial devices," *Applied Physics Letters,* vol. 108, no. 11, 2016, doi: 10.1063/1.4943974.

[120]   H. Zhengli, K. Kohno, H. Fujita, K. Hirakawa, and H. Toshiyoshi, "Tunable Terahertz Filter and Modulator Based on Electrostatic MEMS Reconfigurable SRR Array," *IEEE Journal of Selected Topics in Quantum Electronics,* vol. 21, no. 4, pp. 114-122, 2015, doi: 10.1109/jstqe.2014.2378591.

[121]   P. Pitchappa, M. Manjappa, H. N. S. Krishnamoorthy, Y. Chang, C. Lee, and R. Singh, "Bidirectional reconfiguration and thermal tuning of microcantilever metamaterial device operating from 77 K to 400 K," *Applied Physics Letters,* vol. 111, no. 26, 2017, doi: 10.1063/1.5006836.

[122]   H. Tao, A. C. Strikwerda, K. Fan, W. J. Padilla, X. Zhang, and R. D. Averitt, "MEMS Based Structurally Tunable Metamaterials at Terahertz Frequencies," *Journal of Infrared, Millimeter, and Terahertz Waves,* vol. 32, no. 5, pp. 580-595, 2010, doi: 10.1007/s10762-010-9646-8.

[123] H. Tao, A. C. Strikwerda, K. Fan, W. J. Padilla, X. Zhang, and R. D. Averitt, "Reconfigurable terahertz metamaterials," *Phys Rev Lett,* vol. 103, no. 14, p. 147401, Oct 2 2009, doi: 10.1103/PhysRevLett.103.147401.

[124] T. Kan *et al.*, "Enantiomeric switching of chiral metamaterial for terahertz polarization modulation employing vertically deformable MEMS spirals," *Nat Commun,* vol. 6, p. 8422, Oct 1 2015, doi: 10.1038/ncomms9422.

[125] Y. H. Fu *et al.*, "A Micromachined Reconfigurable Metamaterial via Reconfiguration of Asymmetric Split-Ring Resonators," *Advanced Functional Materials,* vol. 21, no. 18, pp. 3589-3594, 2011, doi: 10.1002/adfm.201101087.

[126] X. Zhao *et al.*, "Voltage-tunable dual-layer terahertz metamaterials," *Microsyst Nanoeng,* vol. 2, p. 16025, 2016, doi: 10.1038/micronano.2016.25.

[127] W. M. Zhu *et al.*, "Microelectromechanical Maltese-cross metamaterial with tunable terahertz anisotropy," *Nat Commun,* vol. 3, p. 1274, 2012, doi: 10.1038/ncomms2285.

[128] M. Zhang, W. Zhang, A. Q. Liu, F. C. Li, and C. F. Lan, "Tunable Polarization Conversion and Rotation based on a Reconfigurable Metasurface," *Sci Rep,* vol. 7, no. 1, p. 12068, Sep 21 2017, doi: 10.1038/s41598-017-11953-z.

[129] Z. Wu *et al.*, "Resonance Switchable Metamaterials Using MEMS Fabrications," *IEEE Journal of Selected Topics in Quantum Electronics,* vol. 19, no. 3, pp. 4700306-4700306, 2013, doi: 10.1109/jstqe.2013.2238217.

[130] W. M. Zhu *et al.*, "Switchable magnetic metamaterials using micromachining processes," *Adv Mater,* vol. 23, no. 15, pp. 1792-6, Apr 19 2011, doi: 10.1002/adma.201004341.

[131] H. K. Kim, D. Lee, and S. Lim, "Frequency-tunable metamaterial absorber using a varactor-loaded fishnet-like resonator," *Applied Optics,* vol. 55, no. 15, 2016, doi: 10.1364/ao.55.004113.

[132] S. R. Thummaluru and R. K. Chaudhary, "Polarization controllable and wide-angle

frequency tunable metamaterial absorber," *Journal of Applied Physics,* vol. 124, no. 20, 2018, doi: 10.1063/1.5054093.

[133] D. Shrekenhamer, W. C. Chen, and W. J. Padilla, "Liquid crystal tunable metamaterial absorber," *Phys Rev Lett,* vol. 110, no. 17, p. 177403, Apr 26 2013, doi: 10.1103/PhysRevLett.110.177403.

[134] S. Savo, D. Shrekenhamer, and W. J. Padilla, "Liquid Crystal Metamaterial Absorber Spatial Light Modulator for THz Applications," *Advanced Optical Materials,* https://doi.org/10.1002/adom.201300384 vol. 2, no. 3, pp. 275-279, 2014/03/01 2014, doi: https://doi.org/10.1002/adom.201300384.

[135] B.-X. Wang and G.-Z. Wang, "Temperature tunable metamaterial absorber at THz frequencies," *Journal of Materials Science: Materials in Electronics,* vol. 28, no. 12, pp. 8487-8493, 2017, doi: 10.1007/s10854-017-6570-x.

[136] Y. Chen, X. Li, X. Luo, S. A. Maier, and M. Hong, "Tunable near-infrared plasmonic perfect absorber based on phase-change materials," *Photonics Research,* vol. 3, no. 3, 2015, doi: 10.1364/prj.3.000054.

[137] L. Lei, F. Lou, K. Tao, H. Huang, X. Cheng, and P. Xu, "Tunable and scalable broadband metamaterial absorber involving VO2-based phase transition," *Photonics Research,* vol. 7, no. 7, 2019, doi: 10.1364/prj.7.000734.

[138] L. Wang, S. Ge, W. Hu, M. Nakajima, and Y. Lu, "Graphene-assisted high-efficiency liquid crystal tunable terahertz metamaterial absorber," *Opt Express,* vol. 25, no. 20, pp. 23873-23879, Oct 2 2017, doi: 10.1364/OE.25.023873.

[139] S. Cao *et al.*, "Graphene–Silver Hybrid Metamaterial for Tunable and High Absorption at Mid-Infrared Waveband," *IEEE Photonics Technology Letters,* vol. 30, no. 5, pp. 475-478, 2018, doi: 10.1109/lpt.2018.2800729.

[140] S. Ghosh and S. Lim, "Fluidically Switchable Metasurface for Wide Spectrum Absorption," *Sci Rep,* vol. 8, no. 1, p. 10169, Jul 5 2018, doi: 10.1038/s41598-018-28574-9.

[141]   F. Hu *et al.*, "A dynamically tunable terahertz metamaterial absorber based on an electrostatic MEMS actuator and electrical dipole resonator array," *Journal of Micromechanics and Microengineering,* vol. 26, no. 2, 2016, doi: 10.1088/0960-1317/26/2/025006.

[142]   M. Liu *et al.*, "Ultrathin tunable terahertz absorber based on MEMS-driven metamaterial," *Microsyst Nanoeng,* vol. 3, p. 17033, 2017, doi: 10.1038/micronano.2017.33.

[143]   J. Xu, D. Jia, Y. Liu, Y. Tian, and X. Yu, "Tunable terahertz metamaterial absorber actuated by thermomechanical bimaterial microcantilevers," *Opt Express,* vol. 28, no. 7, pp. 10329-10336, Mar 30 2020, doi: 10.1364/OE.385948.

[144]   Q. Wang, Y. K. Liu, G. C. Wang, W. X. Jiang, and T. J. Cui, "Tunable triple-band millimeter-wave absorbing metasurface based on nematic liquid crystal," *AIP Advances,* vol. 12, no. 1, 2022, doi: 10.1063/5.0075606.

[145]   T. J. Kang *et al.*, "Deformation characteristics of electroplated MEMS cantilever beams released by plasma ashing," *Sensors and Actuators A: Physical,* vol. 148, no. 2, pp. 407-415, 2008, doi: 10.1016/j.sna.2008.08.022.

[146]   C.-W. Baek, Y.-K. Kim, Y. Ahn, and Y.-H. Kim, "Measurement of the mechanical properties of electroplated gold thin films using micromachined beam structures," *Sensors and Actuators A: Physical,* vol. 117, no. 1, pp. 17-27, 2005, doi: 10.1016/j.sna.2003.11.041.

[147]   W. Leow Cheah, A. B. Mohammad, and N. M. Kassim, "Analytical modeling for determination of pull-in voltage for an electrostatic actuated MEMS cantilever beam," in *ICONIP '02. Proceedings of the 9th International Conference on Neural Information Processing. Computational Intelligence for the E-Age (IEEE Cat. No.02EX575)*, 19-21 Dec. 2002 2002, pp. 233-238, doi: 10.1109/SMELEC.2002.1217814.

[148]   Y.-T. Huang, H.-L. Chen, and W. Hsu, "An analytical model for calculating the pull-

in voltage of micro cantilever beams subjected to tilted and curled effects," *Microelectronic Engineering,* vol. 125, pp. 73-77, 2014, doi: 10.1016/j.mee.2013.12.030.

[149] A. Persano, J. Iannacci, P. Siciliano, and F. Quaranta, "Out-of-plane deformation and pull-in voltage of cantilevers with residual stress gradient: experiment and modelling," *Microsystem Technologies,* vol. 25, no. 9, pp. 3581-3588, 2018, doi: 10.1007/s00542-018-4264-9.

[150] A. O. Watanabe, B. K. Tehrani, T. Ogawa, P. M. Raj, M. M. Tentzeris, and R. R. Tummala, "Ultralow-Loss Substrate-Integrated Waveguides in Glass-Based Substrates for Millimeter-Wave Applications," *IEEE Transactions on Components, Packaging and Manufacturing Technology,* vol. 10, no. 3, pp. 531-533, 2020, doi: 10.1109/tcpmt.2020.2968305.

[151]   S. A, C. A, R. T, and D. B, "Dielectric characterization of Borofloat 33 and some classic glasses by the coaxial cable method," in *2020 IEEE International IOT, Electronics and Mechatronics Conference (IEMTRONICS)*, 9-12 Sept. 2020 2020, pp. 1-6, doi: 10.1109/IEMTRONICS51293.2020.9216429.

[152]   X. Zhao, Y. Pi, W. Wang, S. Ma, and Y. Jin, "High Aspect Ratio TGV Fabrication Using Photosensitive Glass Substrate," in *2018 14th IEEE International Conference on Solid-State and Integrated Circuit Technology (ICSICT)*, 31 Oct.-3 Nov. 2018 2018, pp. 1-3, doi: 10.1109/ICSICT.2018.8564909.

[153] D. W. Wu, "A new method to measure the electromagnetic absorbers — the rectangular waveguide method measurement," *Chinese Physics,* vol. 9, no. 6, p. 4, 1980.

[154] S. Gu, J. P. Barrett, T. H. Hand, B. I. Popa, and S. A. Cummer, "A broadband low-reflection metamaterial absorber," *Journal of Applied Physics,* vol. 108, no. 6, 2010, doi: 10.1063/1.3485808.

[155] J. Zhong, Y. Huang, G. Wen, H. Sun, O. Gordon, and W. Zhu, "Dual-Band Negative

Permittivity Metamaterial Based on Cross Circular Loop Resonator With Shorting Stubs," *IEEE Antennas and Wireless Propagation Letters,* vol. 11, pp. 803-806, 2012, doi: 10.1109/LAWP.2012.2208172.

초록 (국문)

이 논문은 산소 플라즈마 애싱 공정을 사용하여 응력구배 MEMS 외팔보를 사용한 최초의 Ka 대역 주파수 가변 메타물질 흡수체를 제안하고 검증하였다. GHz 영역에서 LC 공진 주파수 가변 방식에 MEMS 액추에이터를 구동하기 위해 메타물질 단위 셀인 분할링공진기 구조는 mm 스케의 외팔보를 정전용량의 요소를 갖도록 설계하였다. 정전용량 변화를 최대화하기 위해 MEMS 외팔보는 플라즈마 애싱 공정에 의해 수직 방향으로 큰 편향차를 갖도록 설계하였다. 응력구배 MEMS 외팔보는 대칭의 분할링 공진기 구조의 단위 셀 4곳에 배열되고 두 셀은 배열구조로 설계되었다. 이 때, 풀인 전압 이상의 높은 전압을 인가시 외팔보는 바닥전극에 붙게 되어 정전용량을 키우고 LC 공진 주파수를 낮춘다.

흡수체의 기계적 거동에 대한 균일성을 개선하기 위해 총 3가지 다른 모양의 외팔보를 설계하였다. 먼저 길이 $400\,\mu\text{m}$, 너비 $50\,\mu\text{m}$인 외팔보를 12개의 배열상태로 설계하여 컴퓨터 시뮬레이션과 측정값을 확인하였다. 첫 번째 흡수체의 플라즈마 애싱 공정을 통한 외팔보 구현 공정의 결과, 96개의 외팔보의 평균 값은 41.5 μm이고 표준 편차는 15.4 μm였다. 첫 번째 흡수체의 경우 제작 외팔보의 산포가 상당히 큼에도 불구하고, 15 V까지 아날로그 튜닝을 하여, 초기 상태의 28 GHz의 공진주파수에서 25.5 GHz의 공진주파수 변화하여 총 2.5 GHz의 주파수

가변범위를 도달하였다. 반사계수는 초기 −5.68 dB에서 −33.60 dB까지 변화하였고, 투과 계수의 경우 −40에서 −60 dB를 유지하였다. 흡수율 계산 결과, 각 공진 주파수에서의 흡수율은 0 V일 때 72.9%에서 계속 증가하며 15 V일때 99.9%의 흡수율을 도달하였다. 그럼에도 불구하고, 외팔보 어레이 갖는 넓은 편향값 산포가 컴퓨터 시뮬레이션과의 괴리가 있어 개선된 설계를 다시 시도하였다.

앞선 설계의 단점을 극복하기 위해 점진적으로 증가하는 패턴의 식각 구멍을 외팔보에 적용하였다. 이 두 번째 구조 또한 제작, 컴퓨터 계산 및 실험 검증하였다. 이러한 식각 구멍 패턴은 외팔보를 산소 플라즈마 애싱 공정으로 구현 시, 제작 균일성을 크게 증가시킨다. 나아가 플라즈마 애싱 공정 또한 시간을 분할하여 제작함으로써 균일도를 크게 증가시킨다. 또한 두번째 설계부터는 응력 구배로 인한 큰 편향을 갖는 외팔보가 갖는 비평형 구동 방식의 해석 어려움에 따라 전압을 개별적으로 인가하며 on/off 형태의 디지털 구동방식으로만 구동하게끔 시스템 구동방식을 변경하였다. 2개의 메타물질 단위 구조에 4개의 전극을 분리하여 총 5개의 구조적으로 다른 상태를 구현하였다. 모든 외팔보가 위로 휘어진 상태에서 전극에 전압을 순차적으로 인가하여 2개씩 바닥에 붙게 하여 최종적으로 모든 외팔보가 바닥에 붙게 하였다. 두 번째 흡수체의 경우, 외팔보 구현이 크게 개선됨에도 불구하고 초기 32.24 GHz의 공진 주파수 값에서 2.14 GHz만 변화하여 최종 30.10 GHz의 공진주파수 측정 결과를 보였다. 흡수율의 경우에도 초기 83.59%에서 최종

90.75%의 결과를 보였지만 컴퓨터 계산과 많은 차이를 보였다.

최종적으로 앞선 2개의 설계를 보완한, 최종 진화한 형태인, 반원형 응력 구배 외팔보를 갖는 흡수체를 설계, 제작, 및 실험 검증하였다. 특히, 외팔보가 갖는 불안정한 기계적 거동을 단순화하여 디지털 구동을 하게끔 흡수체를 설계하였다. 식각 패턴의 거리를 2 μm씩 늘리며 반원 형태의 외곽으로부터 설계한 결과 재현성과 균일성이 매우 크게 개선되었다. 특히 반원 형태의 외팔보의 경우 최고점 편향 높이가 항상 반원 중간에서 구현되기 때문에 반원형 외팔보 간의 모양이 균일하게 유지된다. 제작된 18개 흡수체 샘플에서 144개의 외팔보를 측정한 결과 평균 편향 높이의 평균 값이 51.8 μm였으며 표준 편차는 3.1 μm였다. 4개의 전극에서 기반한 5개 상태의 서로 다른 구조에 따른 반사 계수와 투과 계수를 도파관 측정으로 실험 값을 얻었다. 상용 유한요소법 컴퓨터 계산과 비교 검증하였다. 초기 상태에서 공진 주파수는 32.95 GHz였고, 모든 외팔보가 풀린 전압 인가로 인해 바닥 전극에 붙으면 하면 주파수 28.87 GHz가 되어 총 4.08GHz 이동하여 12.29%의 주파수 가변율을 갖는다. 측정값과 유한요소 시뮬레이션 값의 오차는 5개 상태 모두에서 0.39GHz 이내였다. 흡수율의 경우 각 상태에서 80.95 %, 88.17 %, 86.29 %, 99.21 %, and 86.51% 값을 보였다. 이 논문은 Ka-대역 흡수체의 튜닝 방법으로서 MEMS의 가능성을 보여주었다.